Controlling the optical properties of colloidal lead halide perovskite nanocrystals by shape, size and dimensionality

Dissertation

submitted to the Physics Department

of the Ludwig-Maximilians-Universität München

by

Yu Tong

of

Heilongjiang, China

München, July 6th, 2018

First reviewer:	Prof. Dr. Jochen Feldmann
Second reviewer:	Prof. Dr. Peter Müller-Buschbaum
Additional members of the examination:	Prof. Dr. Thomas Weitz
	Prof. Dr. Matthias Punk
Date of the oral examination:	September 14th, 2018

Publications and awards

Publications presented in this work

- *Boosting Tunable Blue Luminescence of Halide Perovskite Nanoplatelets Through Post-synthetic Surface Trap Repair*

  B. Bohn[#], Y. Tong[#] (equal contribution), M. Gramlich, M. Lai, M. Döblinger, R. L. Z. Hoye, K. Wang, P. Müller-Buschbaum, S. D. Stranks, A. S. Urban, L. Polavarapu, J. Feldmann. Submitted for publication

- *Spontaneous Self-Assembly of Perovskite Nanocrystals into Electronically Coupled Supercrystals: Toward Filling the Green Gap*

  Y. Tong, A. Manzi, E-P. Yao, E. Bladt, K. Wang, P. Müller-Buschbaum, S. Bals, A. S. Urban, L. Polavarapu, J. Feldmann

  Advanced Materials DOI:10.1002/adma.201801117

- *From Precursor Powders-to-$CsPbX_3$ Perovskite Nanowires: One-Pot Synthesis, Growth Mechanism and Oriented Self-assemblies*

  Y. Tong, B. J. Bohn, E. Bladt, K. Wang, P. Müller-Buschbaum, S. Bals, A. S. Urban, L. Polavarapu, J. Feldmann

  Angewante Chemie International Edition 56 (44), 13887-13892 (2017)

- *Highly Luminescent Cesium Lead Halide Perovskite Nanocrystals with Tunable Composition and Thickness via Ultrasonication*

  Y. Tong, E. Bladt, M. F. Ayguler, A. Manzi, K. Z. Milowska, V. A. Hintermayr, P. Docampo, S. Bals, A. S. Urban, L. Polavarapu, J. Feldmann

  Angewante Chemie International Edition 55 (44), 13887–13892 (2016)

- *Quantum Size Effect in Organometal Halide Perovskite Nanoplatelets*

  J.A. Sichert[#], Y. Tong[#](equal contribution), N. Mutz, M. Vollmer, S.F. Fischer, K.Z. Milowska, R.G. Cortadella, B. Nickel, C. Cardenas-Daw, J.K. Stolarczyk, A.S. Urban, J. Feldmann

  Nano Letters 15 (10), 6521-6527 (2015)

Further publications

- *Resonantly Enhanced Multiple Exciton Generation through Below-Band Gap Multiple Photon Excitation in Perovskite Nanocrystals*
  A. Manzi, Y. Tong, J. Feucht, E.-P. Yao, L. Polavarapu, A. S. Urban, J. Feldmann
  Nature Communication 9 (1), 1518 (2018)

- *Preferential Orientation of Crystals Induced by Incorporation of Organic Ligands in Mixed-Dimensional Hybrid Perovskite Films*
  R. Wang, Y. Tong, A. Manzi, K. Wang, Z. Fu, E. Kentzinger, J. Feldmann, A. S. Urban, P. Müller-Buschbaum, H. Frielinghaus
  Advanced Optical Materials 6 (6), 1701311 (2018)

- *Dilution-Induced Formation of Hybrid Perovskite Nanoplatelets*
  Y. Tong, F. Ehrat, W. Vanderlinden, C. Cardenas-Daw, J.K. Stolarczyk, L. Polavarapu , A. S. Urban
  ACS Nano 10 (12), 10936-10944 (2016)

- *Tuning the Optical Properties of Organic/inorganic Hybrid Perovskite Nanoplatelets through Composition and Thickness by Ligand-assisted Exfoliation*
  V. A. Hintermayr, A. Richter, F. Ehrat, M. Doblinger, W. Vanderlinden, J. Sichert, Y. Tong, L. Polavarapu, J. Feldmann, A. S. Urban
  Advanced Materials 28 (43), 9478-9485 (2016)

Awards

- Best poster Award at Soltech International Workshop 2015

- CeNS Publication Award 2017, Category: Best interdisciplinary publication

Contributions to conferences and workshops

- *Quantum Size Effect and Exciton Binding Energy in Lead Halide Perovskite Nanoplatelets*
  Y. Tong, J.A. Sichert, B. J. Bohn, A.S. Urban, J. Feldmann
  International Conference on Optics of Excitons in Confined Systems 2017, **Bath, UK**

- *Optical Properties of Lead Halide Perovskite Nanocrystals with Different Morphologies*
  Y. Tong, L. Polavarapu, A.S. Urban, J. Feldmann
  "Young Ideas in Nanoscience" Workshop by Nanosystems-Initiative-Munich, 2017, Munich, Germany

- *$CsPbX_3$ Perovskite Nanocrystals: A Novel Efficient Optoelectronic Material*
  Y. Tong, L. Polavarapu, A.S. Urban, J. Feldmann
  Workshop on Optical Spectroscopy of New Materials, 2017, Syracuse, Italy

- *Dilution-Induced Formation of Perovskite Nanocrystals Displaying Quantum Confinement*
  Y. Tong, F. Ehrat, J. Stolarczyk, A. Urban, L. Polavarapu
  5th International Solar Technologies Go Hybrid-Workshop, 2016, Munich, Germany

- *Fabrication of $CsPbX_3$ Perovskite Nanocrystals and Their Optical Properties*
  Y. Tong, F. Ehrat, J. Stolarczyk, A. Urban, L. Polavarapu
  Workshop on Photonics and Optoelectronics with New Materials, 2016, Fall Lenggries, Germany

- *Blue Shifted Emission in Organic-Inorganic Hybrid Perovskite Nanocrystals*
  Y. Tong, F. Ehrat, L. Polavarapu, A. Urban,
  CeNS "Channels and Bridges to the Nanoworld" Workshop, 2015, Venice, Italy

- *Tuning the Optical Properties of Perovskite Nanoplatelets by Quantum Confinement*
  Y. Tong, J.A. Sichert, A.S. Urban, J. Feldmann
  4th International Solar Technologies Go Hybrid-Workshop, 2015, Kloster Banz, Germany

Contents

Kurzfassung

In letzter Zeit gewinnen Metallhalogenid-Perowskit-Halbleitermaterialien zunehmend an Aufmerksamkeit, was auf ihre faszinierenden Eigenschaften und vielversprechenden optoelektronischen Anwendungen zurückzuführen ist. Die meisten der ersten Studien konzentrierten sich auf Volumenmaterial dieser Perowskite, während die aufkommenden kolloidalen Perowskit-Nanokristalle aufgrund ihrer einzigartigen Eigenschaften weiteres Interesse auf sich zogen. In dieser Arbeit werden die optischen Eigenschaften von verschiedenen kolloidalen Metallhalogenid-Perowskit-Nanokristallen untersucht und mit ihrer Form, Größe und Dimensionalität korreliert.

Zum einen kann die Photolumineszenz von kolloidalen Metallhalogenid-Perowskit-Nanokristallen durch eine Verringerung ihrer Dimensionalität abgestimmt werden. Zweidimensionale Methylammonium-Bleihalogenid-Perowskit-Nanoplättchen wurden mit unterschiedlichen Dicken synthetisiert und deren Quanten-Größeneffekte werden hier quantitativ untersucht. Durch das Ersetzen des Methylammonium-Ions mit einem Cäsium-Ion, können komplett anorganische kolloidale Cäsium-Bleihalogenid-Perowskit-Nanokristalle erhalten werden und ihre optischen Eigenschaften werden durch die Änderung der chemischen Zusammensetzung sowie der Dimensionalität effektiv abgestimmt. Die Exzitonenbindungsenergie nimmt mit abnehmender Dicke von Nanokristallen zu. Darüber hinaus können die Photolumineszenz-Quantenausbeuten von kolloidalem Cäsium-Bleibromid-Perowskit-Nanoplättchen signifikant durch Zugabe einer $PbBr_2$-Liganden-Lösung erhöht werden, welche die Oberflächendefekte repariert.

Außerdem wurden andere Perowskit-Nanokristalle mit verschiedenen Formen, einschließlich von Cäsium-Bleibromid-Nanodrähten und Superkristallen, hergestellt und ihre optischen Eigenschaften untersucht. Es wurde festgestellt, dass Cäsium-Bleibromid-Nanodrähte durch eine orientierte Anlagerung von Nanowürfeln in kolloidalen Lösungen gebildet werden. Die Nanodrähte zeigen eine rotverschobene Photolumineszenz mit einer Polarisations-Anisotropie aufgrund ihrer länglichen Geometrie. Im Vergleich zu Nanowürfeln weisen die Nanodrähte auch eine viel geringere Photolumineszenz-Quantenausbeute auf, da der strahlungslose Zerfall durch die Ladungsträgermobilität entlang des Drahtes an Bedeutung gewinnt. Des Weiteren können sich Cäsium-Bleibromid-Nanowürfel in kolloidaler Lösung selbst anordnen und sogenannte Superkristalle bilden. Diese Superkristalle zeigen eine offensichtliche Rotverschiebung in der Photolumineszenz infolge einer interpartikulären elektronischen Kopplung durch den hinreichend kleinen Abstand zwischen den benachbarten Nanowürfeln. Inzwischen bleibt die hohe Photolumineszenz-Quantenausbeute der Nanowürfel-Untereinheiten in den Superkristallen erhalten.

Zusammenfassend stellt diese Arbeit einen Einblick in die Dimensionalität abhängigen optische Eigenschaften von kolloidalem Bleihalogenid-Perowskit-Nanokristallen.

Abstract

Recently, metal halide perovskite semiconductor materials are gaining increasing attention owing to their fascinating properties and promising optoelectronic applications. Most of the initial studies focued on the bulk-like perovskite materials, while the emerging colloidal perovskite nanocrystals attract further interest due to their unique properties. In this thesis, the optical properties of various colloidal metal halide perovskite nanocrystals are explored and correlated with their shape, size and dimensionality.

Firstly, the photoluminescence of colloidal metal halide perovskite nanocrystals can be tuned by decreasing their dimensionality. Two-dimensional methylammonium lead halide perovskite nanoplatelets with different thicknesses are synthesized and their quantum size effects are quantitatively investigated. By replacing the methylammonium ion with a cesium ion, all-inorganic colloidal cesium lead halide perovskite nanocrystals are obtained and their optical properties are effectively tuned by changing chemical composition as well as dimensionality. The exciton binding energy is found to increase with decreasing thickness of nanocrystals. In addition, the photoluminescence quantum yields of colloidal cesium lead bromide perovskite nanoplatelets can be significantly increased by adding $PbBr_2$-ligand solution to repair the surface defects.

Furthermore, other perovskite nanocrystals with different shapes including cesium lead bromide nanowires and supercrystals are prepared and their optical properties are investigated. Cesium lead bromide nanowires are found to be formed through an oriented attachment of nanocubes in colloidal solution. The nanowires show a redshifted photoluminescence with a polarization anisotropy due to their elongated anisotropic geometry. The nanowires also exhibit a much lower photoluminescence quantum yield compared to nanocubes due to nonradiative decay causued by charge carrier mobility along the wire. In addition, cesium lead bromide nanocubes can self-assembly into supercrystals in colloidal solution. The supercrystals show an obvious redshift in photoluminescence due to an interparticle electronic coupling enabled by the sufficiently small spacing between neighboring nanocubes. Meanwhile, high photoluminescence quantum yield of the nanocube subunits is retained in the supercrystals.

In summary, this thesis provides an insight into dimensionality-dependent optical properties of colloidal lead halide perovskite nanocrystals.

1. Introduction

As a class of semiconductors, metal halide perovskites have attracted drastically increasing attention in recent years due to their success in photovoltaic applications. This material has a perovskite crystal structure with a general chemical formula of ABX_3. Normally the B site is lead (Pb) or tin (Sn) and the X site is a halide, being Cl, Br, I or a mixture of those. The A site can be an organic molecule such as methylammonium ion ($CH_3NH_3^+$ or MA in short) or an inorganic ion such as cesium (Cs^+). The first type is called organic-inorganic hybrid perovskite and the latter is an all-inorganic perovskite. Although these metal halide perovskite materials attracted tremendous attention only after 2009, actually their history can be dated to more than a century ago [1]. $CsPbX_3$ was found to crystallize in a perovskite-type lattice and exhibit photoconductivity in the 1950s [2, 3], while the synthesis and crystal structures of $MAPbX_3$ were introduced in 1978 [4].

The electronic properties of conventional perovskites attracted broad interest after the demonstration of ferroelectricity in $BaTiO_3$ in the mid-1940s [5]. Thereafter, the first study of metal halide perovskite electronic properties was reported in $CsPbX_3$ compounds in 1950s, which revealed a frequency-dependent photoconductive response [2, 3]. Similar to the conventional oxide perovskites, metal halide perovskites also tend to form layered structures where the layered inorganic metal halide sheets are separated by monovalent organic or inorganic A-site cations. These two-dimensional (2D) famillies of A_2MX_4, $A_3M_2X_7$, and $A_4M_3X_{10}$ compounds were also under investigation due to their interesting ferro- and antiferromagnetic characteristics. Significant efforts were devoted on elucidating their underlying structural properties [6].

Metal halide perovskite optoelectronics began with the pioneering work on the layered organic-inorganic hybrid perovskite systems. The natural self-assembly of layered perovskite structures with molecularly precise structural tunability offers the possibility for tunable optical properties. The organic interlayers provide dielectric confinement effects that can substantially increase the exciton binding energy and the oscillator strength [7, 8]. A transition from semiconducting to

metallic behavior as a function of the number of adjacent inorganic layers in layered tin-based hybrid perovskites highlighted the electronic tunability of these materials [9, 10]. Due to the unique optical and electronic properties, these perovskite materials were introduced as active layers in organic-inorganic light-emitting diodes and as semiconducting channels in thin film field-effect transistors [11, 12].

However, despite the above mentioned work on investigating the electronic and optical properties of metal halide perovskites, an actually new era for these materials started only recently due to their successful application in photovoltaics. In 2009, for the first time, $MAPbX_3$ (X = Br, I) perovskite was employed as a sensitizer to replace the common dye in a dye-sensitized solar cell (DSSC) by Miyasaka et al [13]. The working principle of these perovskite solar cells is similar as the DSSCs, and the power conversion efficiencies (PCE) were 3.1% for X = Br and 3.8% for the X = I case. Afterwards, efforts were made to improve the efficiency and long-term stability of these solar cells based on the perovskite sensitizer. In 2012, a fist nonsensitization type perovskite solar cell was demonstrated by Snaith et al. [14] and a high PCE of 10.9% was achieved by using $MAPbI_{3-x}Cl_x$ perovskite embedded in the mesoporous insulator Al_2O_3 instead of the common n-type TiO_2 semiconductor. The insulating Al_2O_3 served as only a scaffold layer because electron injection from perovskite to Al_2O_3 was not allowed. This result implied that the sensitization concept is not necessarily required for perovskite solar cell design and suggested that electron transfer can occur in the perovskite layer. Within only two years, rapid progress occurred in perovskite solar cells and a high efficiency exceeding 15% was achieved [15, 16]. Perovskite solar cell technology was selected as one of the biggest scientific breakthroughs of 2013 by Science and Nature [17, 18].

Accompanied with the advances of perovskite solar cell technology are the efforts to understand the origin for the exceptional performance of perovskite solar cells. It has been shown that for the most commonly used $CH_3NH_3PbI_3$ perovskite, the bandgap is relatively small and the absorption coefficient is large, enabling an efficient absorption of incident solar light. On the other hand, a balanced electron and hole transport with large diffusion lengths was reported in $MAPbI_3$ and $MAPbI_{3-x}Cl_x$ perovskite [19, 20]. Moreover, the defect density of the perovskite film can be remarkably reduced by improving the quality of perovskite film [21], favoring an effective

transport of charge carriers through the perovskite layer, providing the importance for high performance photovoltaics.

The success in photovoltaics and a better understanding of the underlying physics also boosted the development of other perovskite optoelectronics including light emitting devices and lasers, etc. [22, 23]. Initially, the main focus was on the bulk-like perovskites until the first report of colloidal $MAPbBr_3$ nanocrystals (NCs) with bright fluorescence in 2014 [24]. The emergence of colloidal perovskite NCs further broadened the interests in the metal halide perovskite since colloidal semiconductor NCs generally show unique properties compared with their bulk counterparts. For example, efficient photoluminescence (PL) and tunable emission color by controlling the size of the colloidal NCs. Therefore, colloidal semiconductor NCs are an interesting system for both fundamental studies and optoelectronic applications. It has been shown in several semiconductor systems that the electronic and optical properties can be controlled by changing the size, shape and dimensionality of the NCs [25, 26]. However, for this new class of perovskite colloidal NC, there is still a lack of studies correlating their optical properties with their morphologies. This has motivated my PhD study on the relationship between the optical properties of perovskite NCs and their shape, size and dimensionality.

This thesis is structured in seven parts. After this general introduction of the metal halide perovskite material, the background related to the thesis is briefly introduced. Since the metal halide perovskites are a class of semiconductors, some basic semiconductor fundamentals are given, including low-dimensional semiconductor materials and colloidal semiconductor NCs. Afterwards, the characteristics of metal halide perovskites are discussed and the emerging colloidal perovskite NCs are also introduced. Chapter 3 shows the synthesis of the colloidal metal halide perovskite NCs studied in this work and chapter 4 describes the related experimental setups. Chapter 5 and 6 present the main results of this work. Chapter 5 discusses the optical properties of perovskite NCs with different dimensionalities, starting with the organic-inorganic lead bromide perovskite, $MAPbBr_3$, and then focusing on the all-inorganic $CsPbX_3$ perovskite. The quantum size effects in perovskite NCs with reduced dimensionality are studied in details. In Chapter 6, the optical properties of $CsPbBr_3$ perovskite nanowires (NWs) and supercrystals are studied and compared with the corresponding nanocubes. This thesis ends with a brief conclusion and an

outlook is given showing the potential contribution of my work to the current and future scientific landscape.

2. Background

This chapter gives an overview on the background related to the work presented in this thesis. As the colloidal lead halide perovskites NCs studied in this thesis are a class of semiconductors, semiconductor fundamentals are first discussed, including the electronic band sructure, excitons, low-dimensional semiconductors and colloidal NCs. Afterwards, metal halide perovskites are introduced, their crystal structure and electronic band structure are discussed. Then the characteristic optoelectronic properties of metal halide perovskites and their applications are discussed. Finally, the emerging colloidal metal halide perovskite NCs are introduced.

2.1 Fundamentals of semiconductors

Semiconductors play a crucial role in our everyday life. The development of modern electronic and optoelectronic devices strongly relies on semiconductor materials. The modern understanding of the properties of a semiconductor relies on quantum physical theories. In the following, the fundamentals of both bulk and low-dimensional semiconductors are presented.

2.1.1 Energy bands in semiconductors

Semiconductors are generally solid materials consisting of a large number of periodically arranged atoms or molecules. As schematically shown in figure 2.1 (a), the electrons of a single free atom occupy discrete energy levels. In contrast, when a large number of atoms come close to form a solid crystal lattice, the wavefunctions of electrons in different atoms overlap and the atomic energy levels split thus forming quasi-continuous energy bands.

The band structure can be determined considering the periodic nature of a crystal lattice. In a crystal lattice, a periodic potential $U(\vec{r})$ appears because the atoms are arranged with a periodicity of their Bravais lattice, given by lattice vector $\vec{R}$, described as

$$U(\vec{r}+\vec{R})=U(\vec{r})\,. \tag{2.1}$$

This potential is included in the the Schrödinger equation thus the wavefunction $\psi(\vec{r})$ of electrons in lattice can be determined by solving the time independent Schrödinger equation for a single electron, i.e.

$$E\psi(\vec{r})=\left(-\frac{\hbar^2}{2m}\nabla^2+U\left(\vec{r}\right)\right)\psi(\vec{r})\,, \tag{2.2}$$

where E represents the system energy, $\hbar$ is the reduced Plank constant, m is the electron mass and ∇^2 is the Laplacian.

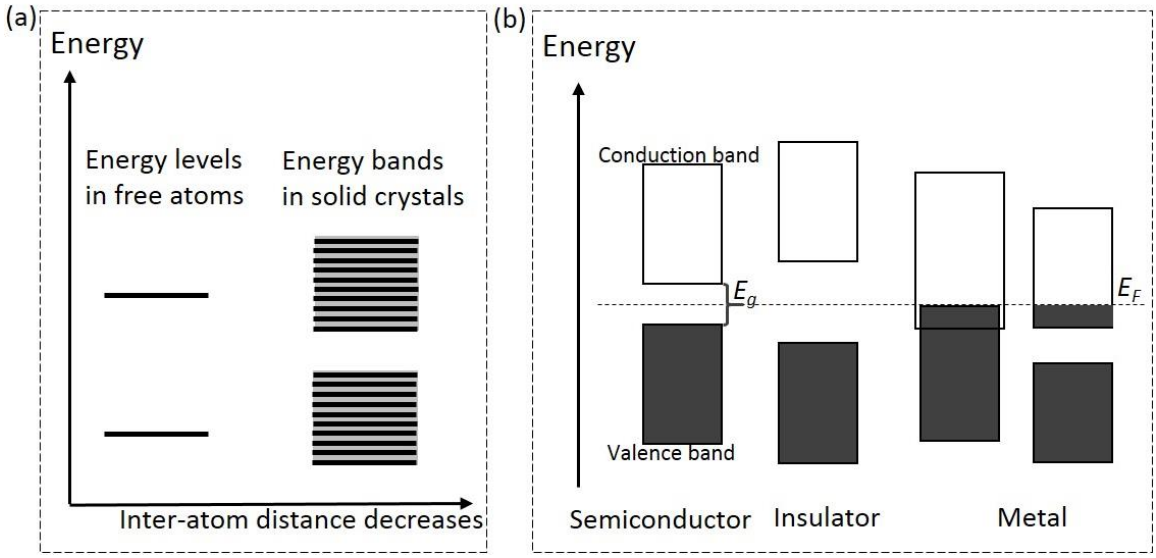

Figure 2.1: (a) Schematic illustration of the electronic energy levels of free atoms and the formation of energy bands in the solid crystals consisting of many atoms. (b) Scheme showing the position of Fermi level with respect to the electronic energy bands in a semiconductor, insulator and metal. The figure is based on a book written by C. Kittel [27].

Considering the Born-von Karman boundary condition, the wavefunction of the electron in the crystal lattice is a Bloch wave which has the form of the free electron wavefunction multiplied by a periodic function with the lattice periodicity, i.e.

$$\psi_{n\vec{k}}(\vec{r})=e^{i\vec{k}\cdot\vec{r}}u_{n\vec{k}}(\vec{r})\,,u_{n\vec{k}}(\vec{r})=u_{n\vec{k}}(\vec{r}+\vec{R})\,. \tag{2.3}$$

This fact is called Bloch's theorem and the electrons are hence called Bloch electrons.

The wavevector $\vec{k}$ takes on any value inside the first Brillouin zone, which is a polyhedron in reciprocal space that is related to the crystal lattice. For each value of $\vec{k}$, there are multiple solutions to the Schrödinger equation labelled by *n*, the band index, which simply numbers the energy bands. For each band an energy function $E_n(\vec{k})$ can be defined, which is the dispersion relation for electrons in that band.

The distribution of electrons in a semiconductor obeys the Fermi–Dirac distribution function, which describes that at thermodynamic equilibrium, the probability of an electron having energy *E* is given by

$$f(E) = \frac{1}{1+e^{(E-E_F)/k_BT}}. \tag{2.4}$$

Here, k_B is the Boltzmann constant, *T* is the system temperature and E_F is the Fermi energy.

As depicited in figure 2.1 (b), for semiconductors and insulators, the conduction band (CB) and valence band (VB) are separated by a bandgap E_g, and the Fermi level lies inside the bandgap. At 0 K, the probability of electrons having energy larger than E_F is zero. With increasing tempeature, the probability to find electrons located above the Fermi level is increased according to equation 2.4. Since the bandgap of a semiconductor is relatively small, electrons can be thermally excited to the CB thus making the semiconductor electrically conductive. The electrical conductivity of a semiconductor will increase with the tempereature increasing due to an enhanced thermal excitation. Addtionally, the electrons in the VB can also be optically excited by absorbing photons with energy larger than E_g. This photoexcitation is a common phenomenon for semiconductors and occurs in metal halide perovskite.

2.1.2 Excitons in semiconductors

As mentioned above, electrons in the CB and holes in the VB can be created by photoexcitation. Since the electron and hole have opposite electronic charge, there can be an attractive force between them resulting from the Coulomb potential

$$U(r) = -\frac{e^2}{2\pi\varepsilon\varepsilon_0 r}, \tag{2.5}$$

with r being the distance of electron and hole and ε being the dielectric constant of the material.

A strong Coulomb interaction will make the electron and hole form a bound state instead of existing as free carriers, this bound electron-hole pair is called an exciton as schematically shown in figure 2.2 (a).

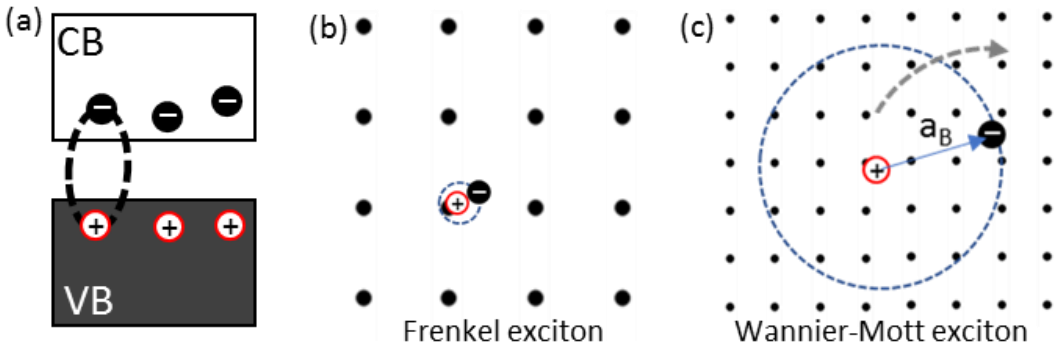

Figure 2.2: (a) Coulomb interaction between a negatively charged electron in the CB and a positively charged hole in the VB in a semiconductor. (b) A Frenkel exciton and (c) a Wannier-Mott exciton based on ref [27].

There are two basic types of excitons in solids: Frenkel excitons [28] and Wannier-Mott excitons [29] as depicted in figure 2.2 (b) and (c), respectively. Frenkel excitons are typically found in alkali halide crystals and organic molecular materials. In these materials with small dielectric constants, the Coulomb interaction between the electron and hole is strong and the exciton Bohr radius (a_B) is small. Frenkel excitons are also known as "tightly bound excitons" which are generally localized at a specific atom or molecule.

In contrast, Wannier-Mott excitons are found in many semiconductor materials. The dielectric constant is generally large in these materials and a strong dielectric screening will reduce the Coulomb interaction between electrons and holes. Additionally, the small effective mass of electrons in semiconductors also favors a large a_B and a Wannier-Mott exciton is generally much larger than the lattice spacing in a semiconductor. A Wannier-Mott exciton is usually delocalized and it can move inside the material, so it is also called "free exciton".

In metal halide perovskites, both free carriers and Wannier-Mott excitons are reported [30, 31]. Figure 2.3 (a) shows the excitation of an electron in the one-particle picture and the two-particle picture highlighting the exciton concept is depicited in figure 2.3 (b). The linear dispersion relation of the excitation light is also included to show the possible interactions between photons and excitons at the intersection of the two dispersion relations.

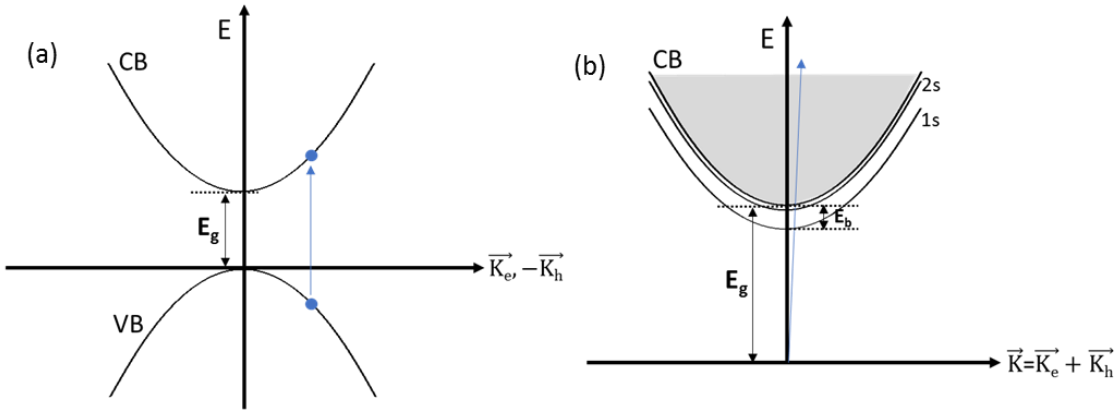

Figure 2.3: Excitation of an electron-hole pair in (a) one particle picture with VB and CB and (b) in the exciton two particle picture. The pictures are based on ref [32].

The quantum mechanical description of Wannier-Mott excitons in metal halide perovskites is similar to that of a hydrogen atom and the wavefunction of the exciton can be determined by solving the Schrödinger equation considering the attractive interaction between the electron and the hole. Similarly as in the hydrogen atom, the energy of the exciton is quantized (figure 2.3 (b)), The ground state of exciton is the state with the quantum number n=1, (1s exciton), while n=2 is the 2s exciton state, n=3 represents the 2p exciton state and so on.

For the 1s exciton, the Bohr radius of the hydrogen-like exciton is given by

$$a_B = \frac{4\pi\varepsilon\hbar^2}{\mu e^2}. \tag{2.6}$$

Here, ε is the dielectric constant of the medium and μ is the reduced mass given by

$$\mu = \frac{m_e^* m_h^*}{m_e^* + m_h^*}, \tag{2.7}$$

where m_e^* and m_h^* are the effective mass of the electron in the CB and hole in the VB, respectively.

The exciton binding energy, E_b, is the difference between the energy of the 1s exciton and the continuum band edge as shown in figure 2.3 (b). It can be written as

$$E_b = \frac{\mu}{2\hbar^2}\left(\frac{e^2}{4\pi\varepsilon}\right) = \frac{\hbar^2}{2\mu a_B^2}. \tag{2.8}$$

The quantization effect of this energy is given by

$$E_n = \frac{1}{n^2} E_b, \tag{2.9}$$

and the transition energy for the exciton in the corresponding exciton state is

$$E_{xn} = E_g - E_n. \tag{2.10}$$

Quantized exciton states in semiconductors have been observed from optical absorption spectroscopy [33, 34]. Exciton binding energy of bulk-like $MAPbI_3$ perovskites are found to be several tens of meV [35-38] .

2.1.3 Low-dimensional semiconductors

In bulk semiconductors, the material size is considered to be infinite thus not restricting the carrier wavefunction. However, if the material size is reduced to the nanometer scale, quantum confinement effects need to be considered [39]. The system can be confined in one, two or three dimensions, resulting in a 2D quantum well, 1D quantum wire or 0D quantum dot structure, respectively [40]. Quantum size effects have significant impacts on the behavior of charge carriers in semiconductors, and will dramatically modify the electronic and optical properties of low-dimensional semiconductor system with respect to their bulk counterparts [41-44]. The density of states (DOS) for electrons in low-dimensional semiconductors show significant difference from 3D bulk semiconductors as illustrated in figure 2.4.

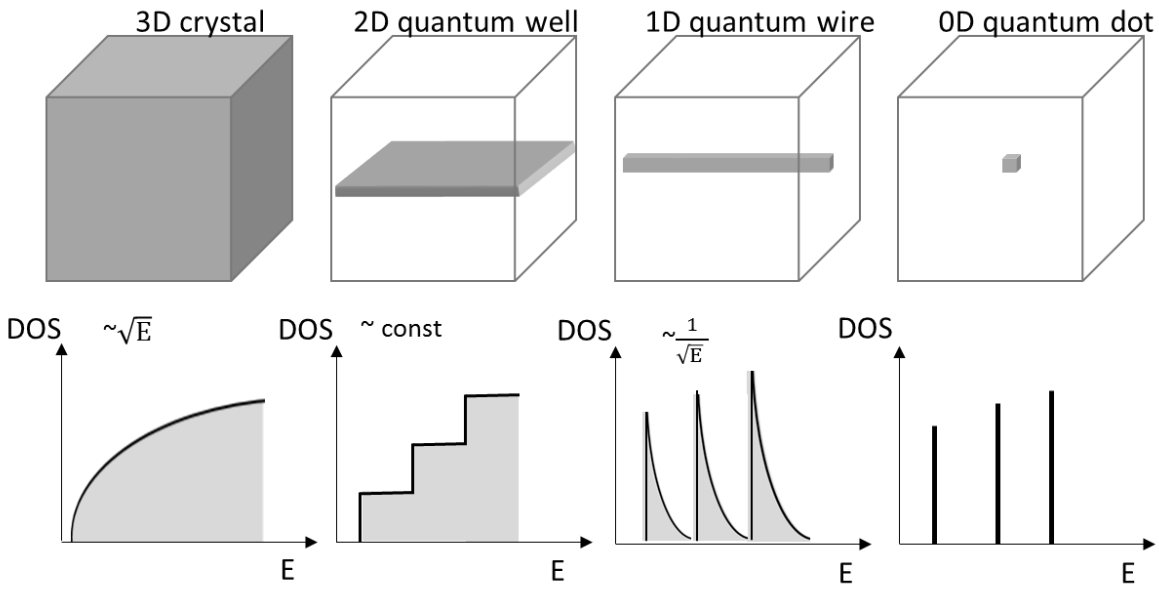

Figure 2.4: Density of states (DOS) for electrons in a 3D crystal, a 2D quantum well, a 1D quantum wire and a 0D quantum dot according to ref [40].

The dimensionality of a semiconductor not only affects the properties of free carriers but also influence the Coulomb interaction between the electrons and holes. Accordingly, the properties of excitons can be changed in low-dimensional semiconductors compared with the corresponding bulk semiconductors [45].

Excitons in metal halide perovskites are generally hydrogen-like Wannier-Mott excitons, and the excitonic impact on the absorption spectrum can be modeled by using the Elliott equation [33]. In Elliott's theory, single particles states form the basis of the pair states with an envelope function expressing the pair correlation. The motion of the exciton can be split into the motion of the center of mass and the relative motion of the electron-hole pair. This approximation is only valid for Wannier-Mott excitons and can be used to extract the exciton binding energy and band gap energy of a material. The reduced dimensionality from 3D to 2D impacts the absorption spectra of a semiconductor and the theoretical absorption according to the Elliott formula is different for the 3D and 2D case.

In the 3D case, the Elliott formula is given by

$$\alpha_{3D}(\hbar\omega) = \left[A \cdot \Theta(\hbar\omega - E_g) \cdot D_{CV}^{3D}(\hbar\omega) \right] \cdot \left[\frac{\pi x e^{\pi x}}{\sinh(\pi x)} \right] + A \cdot E_b \sum_{n=1}^{\infty} \frac{4\pi}{n^3} \delta\left(\hbar\omega - E_g + \frac{E_b}{n^2} \right), \tag{2.11}$$

where α is the absorption coefficient, A is a constant related to the transition matrix, Θ is the Heaviside step function and D_{CV}^{3D} represents the joint density of states in the 3D case. x is given by $x = \left(E_b (\hbar\omega - E_g)^{-1} \right)^{1/2}$ [33].

In the 2D case, the Elliot formula needs to be modified using the 2D hydrogen-like model [46], given by

$$\alpha_{2D}(\hbar\omega) = \left[A \cdot \Theta(\hbar\omega - E_g) \cdot D_{CV}^{2D}(\hbar\omega) \right] \cdot \left[\frac{e^{\pi x}}{\cosh(\pi x)} \right] + A \cdot E_b \sum_{n=1}^{\infty} \frac{4\pi}{\left(n + \frac{1}{2}\right)^3} \delta\left(\hbar\omega - E_g + \frac{E_b}{4 \cdot \left(n + \frac{1}{2}\right)^2} \right). \tag{2.12}$$

The first part of equation 2.11 and 2.12 corresponds to the continuum absorption including the Sommerfeld enhancement [47], and the second part is attributed to the excitonic absorption with n representing the discrete exciton levels.

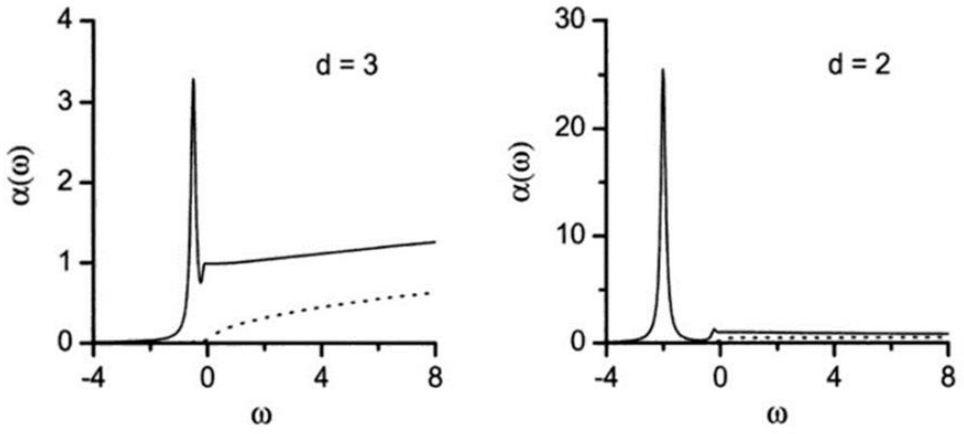

Figure 2.5: The calculated absorption spectrum for 3D (d=3) and 2D (d=2) semiconductors according to the Elliott formula. The dotted lines represent the absorption without considering Coulomb interaction and

Sommerfeld enhancement. The figure is taken from a book written by S. Glutsch [45].

Figure 2.5 shows the theoretical absorption spectra of a 2D and 3D semiconductor according to the Elliott formula. The dotted lines show the absorption without including the electron-hole interactions. It can be seen that in the 3D case, without these interactions, the absorption spectrum is essentially shaped by the energy-dependent DOS of electrons which is depicted in figure 2.4. Once including the interactions, a peak arises at ω smaller than zero, followed by an absorption band. This peak corresponds to the 1s exciton (n=1) according to equation 2.11 However, further excitonic peaks (n>1) can hardly be identified as the oscillator strength decreases due to its proportionally to n^{-3}. The Coulomb interactions are accounted for and result in a strong Sommerfeld enhancement of the absorption of the continuum states. In the 2D case, the relative intensity of the excitonic peak is enhanced and the shape of the continuum absorption is also changed. According to equation 2.11 and 2.12, the absorption area of the exciton is increased by a factor of four for 2D compared to 3D case [48]. Additionally, since the DOS of electron in 2D system shows a step-like function depending on the energy (figure 2.4), the continuum absorption becomes flatter.

The above discussion is mainly focused on the comparison beween 2D and 3D semiconductors as the 2D and 3D perovskite NCs are the major systems investigated in this thesis. In fact, owing to the progress in the fabrication technology of low-dimensional semiconductors since the 1980s, the physical properties of free electrons and excitons in various low-dimensional semiconductor systems with different dimensionalities have been extensively investigated [43, 49-53]. Moreover, the anisotropic geometry of low-dimensional semiconductors also makes them important systems for studying anisotropic electronic and optical properties [54-57].

2.1.4 Multiple quantum wells and superlattices

As discussed, quantum confinement effects have significant impacts on the electronic and optical properties of low-dimensional semiconductors. One of the most elementary problems in quantum mechanics is that of a particle confined to a 1D rectangular potential well. This can be experimentally achieved by making a 2D quantum well structure where carriers are confined only in one direction. A typical example of these quantum well structures is a thin GaAs layer sandwiched between two GaAlAs layers. In this structure, GaAs with a small bandgap acts as the

well and GaAlAs with a larger bandgap acts as barriers [53]. Multiple quantum well (MQW) structures consist of a series of quantum wells, i.e. a series of alternating layers of wells and barriers [58]. If the barrier layer is thick enough to prevent significant electronic tunneling, then each well can be considered to be electronically isolated. Alternatively, if the barrier thickness is sufficiently thin to allow electronic tunneling and coupling, a superlattice can be formed [58, 59]. In the superlattice, there is a significant overlap of the electronic wavefunctions thus that the electronic charge distribution can become delocalized along the well layer direction normal. This electronic coupling leads to a broadening of the quantized electronic states of the wells, which are termed minibands.

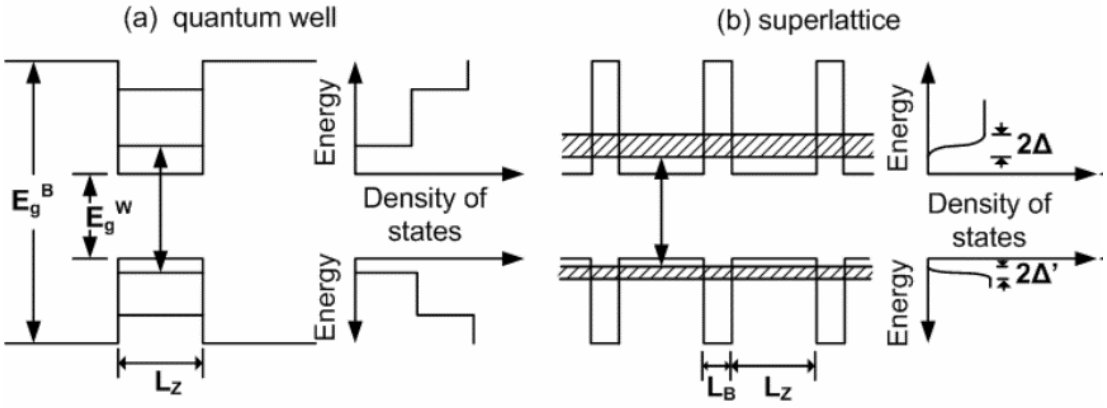

Figure 2.6: Potential and subband energy diagrams of (a) a single quantum well and (b) a superlattice. Quantized states in isolated quantum well expand to form minibands in a superlattice. The figure is taken from a book wirten by H.T. Grahn [60].

Figure 2.6 shows the potential and subband energy diagrams of a single quantum well and a superlattice. In the case of an isolated single quantum well, quantized states are formed due to the quantum size effect and localized in the particular region in the well. In the superlattice, tunnelling of electrons through the thin barriers results in an electronic coupling and the original quantized states expand to form minibands.

The width of the miniband, 2Δ, depends on how much the wavefunction can penetrate into the barrier and it can be calculated based on the Kronig-Penney model using the effective mass approximation [61]. The eigenvalue of energy can be determined from

$$\cos\left[K(L_Z + L_B)\right]) = \frac{1}{2}\left(\frac{m_W^*\theta}{m_B^*k} - \frac{m_B^*k}{m_W^*\theta}\right)\sin(kL_Z)\sinh(\theta L_B) + \cos(kL_Z)\cosh(\theta L_B), \quad (2.13)$$

with $k^2 = \frac{2m_W^*E}{\hbar^2}$ and $\theta^2 = \frac{2m_B^*(V-E)}{\hbar^2}$.

Here, V is the band offset between the quantum well and the barrier, L_Z and L_B are the thickness of the quantum well and barrier, respectively, k is the wave vector, m_W^* and m_B^* are the effective masses of electrons in the quantum well and barrier materials, respectively.

In this thesis, stacked perovskite nanoplatelets (NPls) and and closely packed perovskite NC assemblies are considered as superlattices and the role of electronic coupling on affecting their optical peropeties of perovskite NCs is investigated.

2.1.5 Colloidal semiconductor nanomaterials

Low-dimensional semiconductors are of significant importance for both fundamental physics and advanced applications [62-64]. In the studies of low-dimensional semiconductors including 0D quantum dots, 1D quantum wires and 2D quantum wells, the nanostructures are usually fabricated by epitaxial growth or lithography [42, 53, 65-68]. Since the 1980s, the solution synthesis of colloidal semiconductor quantum dots has become an important supplementary to solid-state fabrication methods [69-72].

Colloidal semiconductor NCs are typically synthesized in solution using capping ligands to control the reaction. The obtained NCs generally have a good dispersity in solvent and can form colloidal dispersions [72]. The difference between semiconductor quantum dots obtained by epitaxial growth and colloidal synthesis is sketched in figure 2.7 (a). The solution synthesis of colloidal semiconductor NCs is relatively easy and cost-efficient in comparison with the traditional solid state methods. Moreover, as shown in figure 2.7 (b), narrow and efficient PL with tunable color can be achieved by controlling the size of the colloidal quantum dots and make core-shell heterostructures [25, 73-76]. These advantages of the colloidal semiconductor quantum dots make them excellent candidates for light emitting applications [77-79].

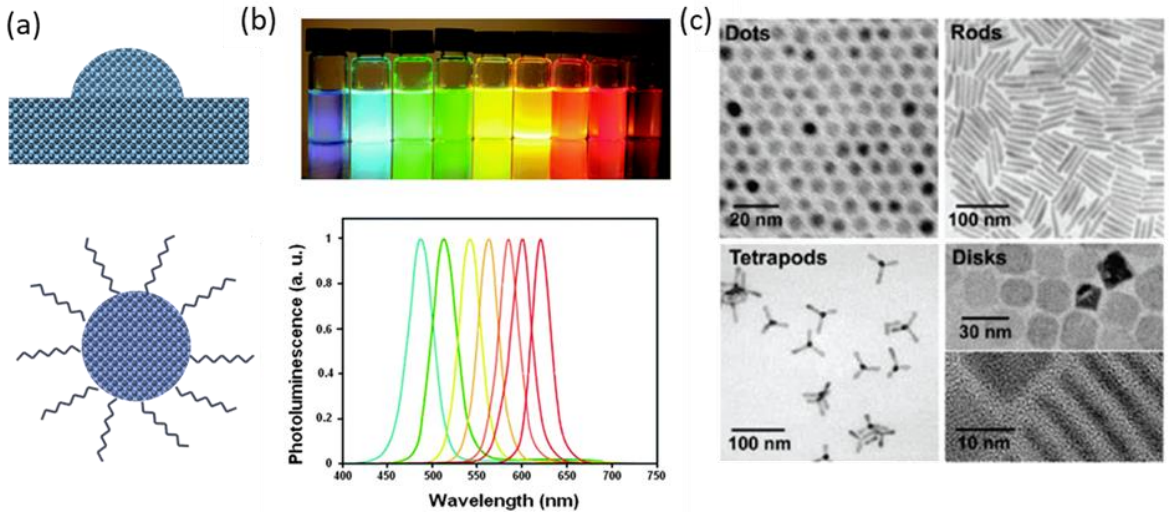

Figure 2.7: (a) Sketch showing a semiconductor quantum dot fabricated by epitaxial growth (top) and colloidal synthesis (bottom). (b) Tunable PL of colloidal semiconductor NCs by changing the size. Reprinted with permission from [73]. Copyright 2016 Royal Society of Chemistry. (c) TEM images of colloidal semiconductor NCs with various shapes. Reproduced with permission from [25]. Copyright 2009 American Chemical Society.

Another important feature of colloidal semiconductor NCs is the controllability of shape and dimensionality. Even though earlier studies of semiconductor NCs mainly focused on 0D sphere-like quantum dots, with the increasing interest in these colloidal nanomaterial system, synthesis approaches of colloidal NCs with different shapes and dimensionalities were broadly explored and a variety of colloidal semiconductor NCs with different shapes have been obtained (figure 2.7 (c)) [25, 80-82].

Particularly, 2D colloidal semiconductor nanomaterials have attracted tremendous interests and various colloidal 2D semiconductor NCs have been synthesized and studied [82-85]. These colloidal 2D NCs are generally surrounded by organic capping ligands. Due to the large E_g of the organic ligand and a consequent larger barrier energy according to figure 2.6 (a), there is a stronger quantum confinement in the colloidal 2D semiconductor NCs in comparison with the traditional quantum wells. Additionally, as schematically illustrated in figure 2.8, the organic ligands normally have relatively small dielectric constants compared to that of the AlGaAs barriers in a traditional quantum well, i.e. $\varepsilon_2 < \varepsilon_1$. The smaller dielectric constant leads to a weaker screening effect on the Coulomb interaction according to:

$$U_{screen}(\vec{k}) = \frac{U_{non-screen}(\vec{k})}{\varepsilon(\vec{k},\omega)}, \tag{2.14}$$

where $U_{screen}(\vec{k})$ and $U_{non-screen}(\vec{k})$ represent the Coulomb potential with and without screening effect, respectively and ε is the dielectric constant of the material.

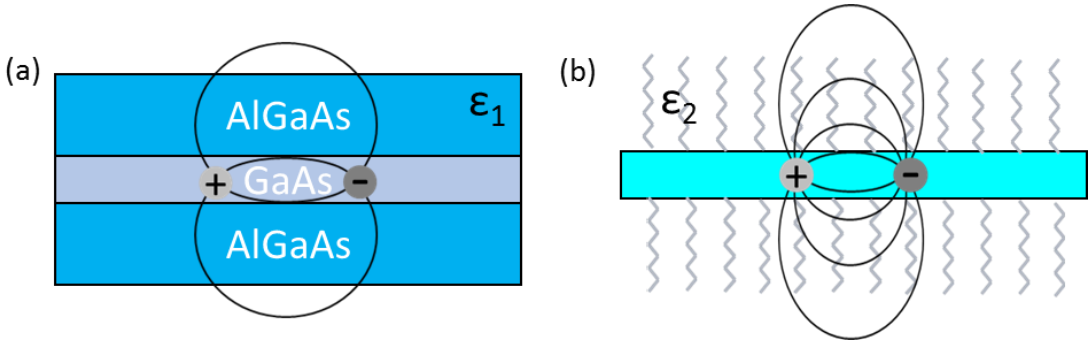

Figure 2.8: Schematic illustration of the Coulomb interaction between an electron and a hole in (a) a traditional GaAs quantum well and (b) a 2D colloidal semiconductor NC. In colloidal 2D semiconductor NCs, the Coulomb interaction is strong due to a weak dielectric screening effect resulting from the small dielectic constant of the surrounding ligands.

The strong quantum confinement and strong Coulomb interaction between electrons and holes in colloidal 2D semiconductor NCs make these colloidal NCs ideal systems to study 2D electronic and excitonic properties [83, 85-87]. In this work, a new class of 2D colloidal semiconductor material, namely the colloidal lead halide perovskite NPls are synthesized and their optical properties are studied.

2.2 Metal halide perovskite

As a class of semiconductor, metal halide perovskites have been studied for a long time, but only in recent years they attract significant attention due to their extraordinary performance in photovoltaic applications. Great effort has been devoted to uncover the origin for the high efficiency of perovskite solar cells as well as to continuously optimize the solar cells. In this section, major characteristics of metal halide perovskites are presented and the emerging colloidal perovskite NCs are also introduced.

2.2.1 Perovskite crystal structure

Metal halide perovskites belong to the perovskite family which possesses the general ABX_3 stoichiometry. The perovskite mineral was first discovered by Gustav Rose in 1839 (oxide perovskite $CaTiO_3$) and named after Russian mineralogist Lev Perovski [88]. More than half a century after the initial identification of oxide perovskites, a series of inorganic metal trihalide perovskites with the chemical formula of $CsPbX_3$ (X = Cl, Br, and I) were reported [1]. The highest symmetry phase of perovskite is the cubic phase with a $Pm\bar{3}m$ space group. The cubic crystal structure of ABX_3 perovskites is schematically shown in figure 2.9 (a). The B-site element is octahedrally coordinated in a BX_6 configuration and the A component is situated in the cuboctahedral cavity formed by the 8 nearest-neighbor units of BX_6 octahedra. However, a phase transition lowering this symmetry generally occurs through octahedral rotations that can be described using Glazer's notation [89-91]. The phase transition can be induced by temperature, pressure, and/or chemistry, and it will strongly influence the electronic structure and consequent optical and optoelectronic properties [92-96].

3D bulk perovskite crystals are formed through a periodical arrangement of the cubic units and exibit cubic shape, as shown in figure 2.9 (b). SEM image of cubic shaped $CsPbBr_3$ perovskite crystals is also given in figure 2.9 (c). The formability of general bulk perovskite structure can be predicted as the A-site component is under size constraints caused by the corner-sharing BX_6 octahedra [91, 97]. A semiempirical geometric parameter, known as the Goldschmidt tolerance factor [98], is used to predict the formability of metal halide perovskite and it is given as

$$t = \frac{r_A + r_X}{\sqrt{2}(r_B + r_X)}, \tag{2.15}$$

where r_A, r_B and r_X are the ionic radii of the corresponding components. Empirically, the majority of bulk metal halide perovskite forms in the approximate range of $0.81 \leq t \leq 1$. A second constraint is the octahedral factor, $\mu = r_B/r_X$, a parameter determining the octahedral stability and typically lies in the range of $0.44 \leq t \leq 0.9$ [97]. The combination of these two factors provides a parameter space for perovskite formability.

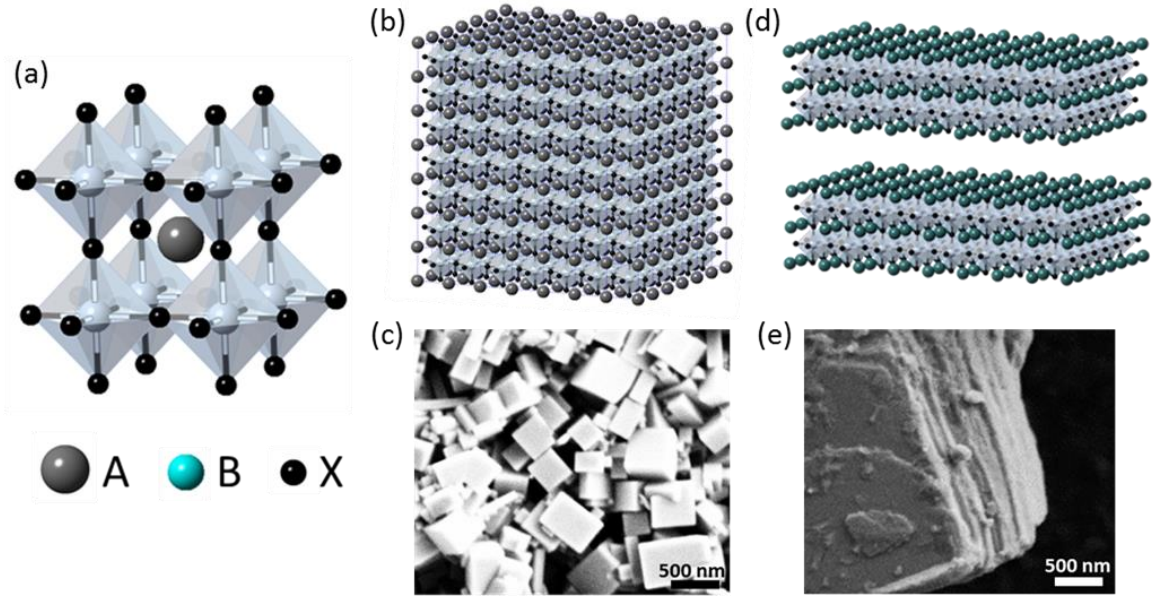

Figure 2.9: (a) Scheme showing that in perovskite crystal, A-site component is in the center of cuboctahedral voids formed by eight BX_6 octahedra. (b) Schematic illustration of a 3D cubic perovskite crystal and (c) SEM image of cubic shaped $CsPbBr_3$ perovskite crystals. (d) Schematic illustration of layerd perovskite structures and (e) SEM image of layered $MAPbI_3$ perovskite structures.

Generally, a larger size of A-site component will favor a 2D layered perovskite crystal structure as shown in figure 2.9 (d). SEM image of $MAPbI_3$ perovskite consisting 2D layered structures is given in figure 2.9 (e) as an example. In addition to the 2D layered perovskite structures, other lower-dimensional structures such as 1D chained structure and 0D isolated octahedra are also important extensions to 3D bulk-like perovskites [99]. Furthermore, subtle chemical modifications in perovskite materials can dramatically change their electronic and optical properties [100, 101].

In this thesis, the optical properties of both 3D and 2D lead halide perovskite NCs are studied.

2.2.2 Metal halide perovskite band structure

Typical metal halide perovskites which are of optoelectronic interest, for example, the most common ones with A-site as Cs or MA and B site as Pb, are direct bandgap semiconductors with strong band edge optical absorption and luminescence. The electronic structures play an important role in governing their properties. It has been reported that the electronic structure near the band edge is primarily dictated by the basic BX_6 clusters [99, 102, 103]. Therefore, orbital diagrams of PbX_6 clusters provide a foundation for understanding band structures of lead halide perovskites [104].

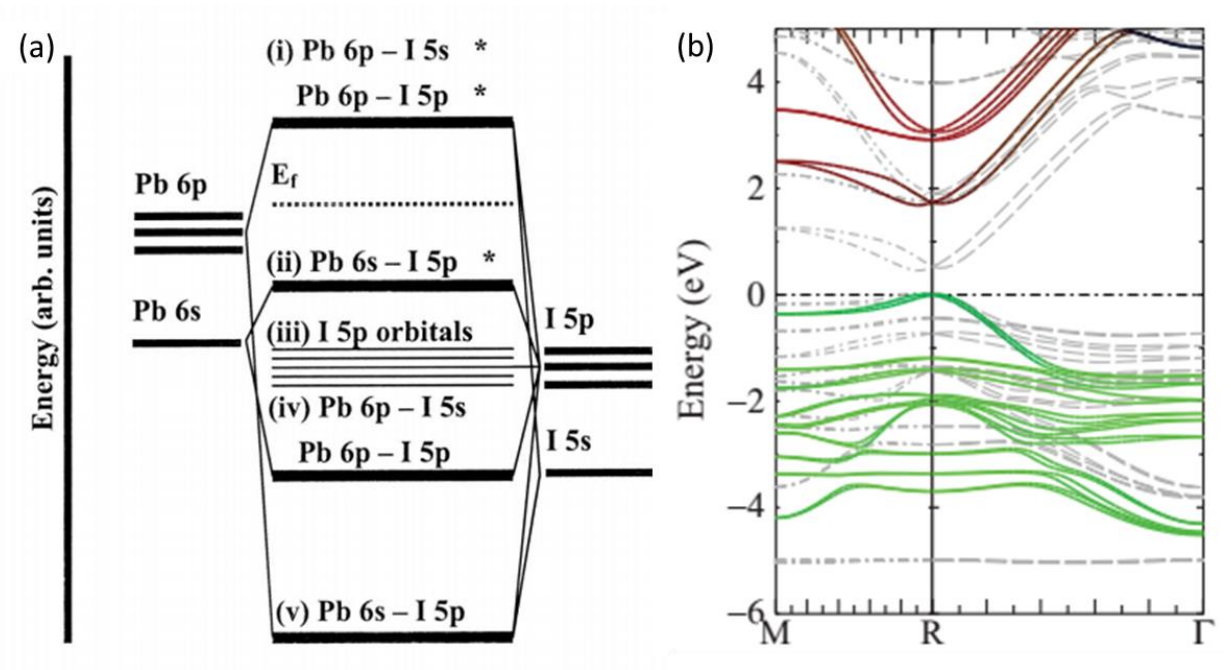

Figure 2.10: (a) Bonding diagram of a $[PbI_6]^{4-}$ octahedra without considering spin orbital coupling. (b) Calculated electronic band structure of $MAPbI_3$. Orbital contributions are indicated by I 5p (green), Pb 6p (red), and Pb 6s (blue). Reproduced with permission from [95], copyright 2016 American Chemical Society.

Figure 2.10 (a) shows the bonding diagram of $[PbI_6]^{4-}$ units, a Pb 6s−I 5p σ-antibonding orbital comprises the highest occupied molecular orbital (HOMO), while Pb 6p−I 5p π-antibonding and Pb 6p−I 5s σ-antibonding orbitals constitute the lowest unoccupied molecular orbital (LUMO) [102]. Comparable electronic character is retained in the bulk $MAPbI_3$ perovskite as shown in figure 2.10 (b). The large halide contribution at the VBM makes it easier to be modulated by the halide composition whereas the large Pb character in the CB makes it relatively insensitive to

halide chemistry states [95]. In many metal halide perovskite materials, the band gap of metal halide perovskite follows the tendency of E_g(Cl)> E_g(Br)> E_g(I) [105, 106].

Metal halide perovskite is considered as a special class of sp semiconductors since they exhibit an inverted electronic structure compared with conventional III−V compounds like GaAs, which has substantial As 4p character in the VB and Ga and As 4s character in the CB [107-110]. The unique electronic structure at the band edge of metal halide perovskite gives rise to a positive deformation potential described by

$$\alpha_v = \frac{\partial E_g}{\partial \ln V} > 0, \tag{2.16}$$

with V representing the unit volume. Such a relationship has been probed by monitoring changes in PL as a function of temperature or pressure [95, 111]. Upon lattice contraction, covalent interactions between Pb 6s and I 5p at the VBM are enhanced, causing an increase in the energy of these states. In contrast, the CBM is less significantly affected by lattice deformations. Therefore, a raised VBM and relatively constant CBM will result in a redshifted absorption upon lattice contraction, contrary to what is typically observed in conventional semiconductors [112].

Another feature of the perovskite band structure shown in figure 2.10 (b) is the comparable parabolicity of the VB and CB near the R point, indicating comparable effective masses of electrons and holes according to the dispersion relation

$$E = \frac{\hbar^2 k^2}{2m^*}. \tag{2.17}$$

It has been calculated that for bulk-like $MAPbI_3$ perovskite, $m_e^* = 0.19m_0$ and $m_h^* = 0.25m_0$ (m_0 is the mass of free electrons) [113], in close agreement with the values determined by high-field magneto absorption spectroscopy [35]. While in contrast, in other typical semiconductors, there is a large difference between the effective masses of the electron and hole. For instance, in GaAs, the effective masses of electrons and holes are $m_e^* = 0.07m_0$ and $m_h^* = 0.50m_0$, respectively [95]. The similar effective mass of electrons and holes in $MAPbI_3$ perovskite is a main reason for the

balanced electron and hole drift/diffusion lengths in $MAPbI_3$ perovskite have been observed in a number of experimental studies [19, 20].

The similar effective masses of electrons and holes of metal halide perovskite materials will lead to a comparable quantum confinement effect on electrons and holes in low-dimensional perovskite NCs, which will be discussed in chapter 5.

2.2.3 Metal halide perovskites optoelectronics

As already mentioned, efforts have been made on studying the physical properties of metal halide perovskite and seeking for their optoelectronic applications since over fifty years ago [2-4]. However, the attention on metal perovskite only drastically increases in recent years due to its promising application in photovoltaics, particularly the organic-inorganic hybrid perovskite $MAPbI_3$. Here, more details about the physical properties of metal halide perovskite such as carrier diffusion, are discussed based on the perovskite solar cells.

The first perovskite solar cell was reported in 2009 and the power conversion efficiency (PCE) was lower than 4% at that time. However, in the following years, the PCE of perovskite solar cells has experienced a rapid increase and quickly reached more than 16%, as shown in figure 2.11 (a) [114]. The high PCE of perovskite solar cells is already comparable to commercial silicon solar cells and surpasses most organic solar cells.

There are two main different architectures for perovskite solar cells. Figure 2.11 (b) shows the architecture of a perovskite-sensitized solar cell, which was used at the early stages of the development of perovskite solar cells. The structure is similar to the solid-state dye-sensitized solar cells, and the working principle is also shown in figure 2.11 (b). Perovskite, like other dye sensitizers, attaches to the surface of the mesoporous electron transport material (ETM) such as TiO_2, forming an ultrathin layer between the hole transporting material (HTM) and the ETM. The photogenerated carriers in the sensitizer enter the HTM and ETM where they transport to the corresponding electrodes. However, it was discovered later that the mesoporous structures are not necessary. Planar perovskite solar cells showed high efficiency and their PCE can be effectively increased by improving the quality of the perovskite film [115-117]. As depicted in figure 2.11 (c), for planar perovskite solar cells, a flat perovskite film is sandwiched between the HTM and ETM

layers. The carriers generated by photoexcitation diffuse through the perovskite layer to reach the HTM or ETM layer and subsequently the corresponding electrode.

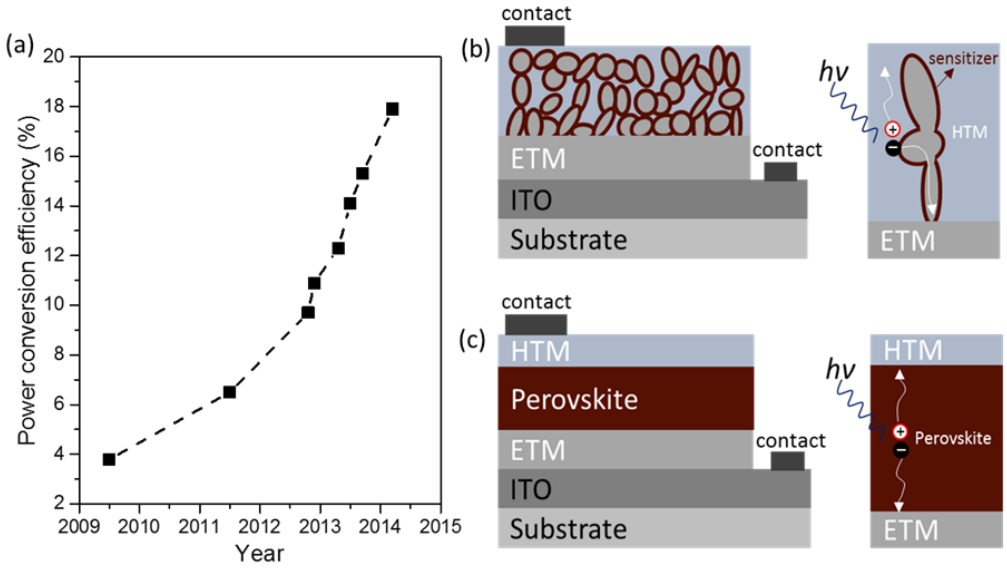

Figure 2.11: (a) Evolution of power conversion efficiency of metal halide perovskite based solar cells as a function of year. (b) Architecture and working principle of a perovskite solar cell with the same structure as a dye-sensitized solar cell. (c) Architecture and working principle of a planar perovskite solar cell. The figure is based on ref [95].

Several reasons are believed to be responsible for the high performance of perovskite solar cells. First, the optical absorption coefficient of the metal halide perovskite is high, enabling an efficient absorption of photons thus generating a large number of charge carriers [118]. Additionally, the large diffusion length of the carriers and low trap-state density in perovskite film facilitate an effective transport of photogenerated charge carriers through the perovskite film to reach the electrodes, thus yielding a high photovoltaic performance [19, 119, 120].

The diffusion length of charge carriers (L_D) is a crucial parameter for solar cell since it directly influences the efficiency of charge collection in a solar cell film. L_D is the average distance that a charge carrier is able to travel due to diffusion before recombination occurs. L_D can be calculated according to

$$L_D = \sqrt{D\tau}\,, \tag{2.18}$$

where D is the diffusion coefficient, and τ is the lifetime of charge carriers before they recombine. The D of electron or hole in a perovskite layer can be determined according to the diffusion equation [19, 121]

$$\frac{\partial n(x,t)}{\partial t} = D\frac{\partial^2 n(x,t)}{\partial x^2} - k(t)n(x,t)\,, \tag{2.19}$$

where n (x, t) is the number and distribution of excitations in the perovskite film and k (t) is the PL decay rate. It has been reported that the electron and hole in the perovskite have comparable large diffusion lengths, which is around 200 nm for $MAPbI_3$ and even larger in $MAPbI_{3-x}Cl_x$ film (~1 μm). The large diffusion length suggests that the photogenerated charge carriers in the perovskite film can efficiently transport through the perovskite layer to reach the charge transport layers so that mesostructures are not necessary for highly efficient charge generation and collection, supporting the high PCE achieved in planar perovskite solar cells [16, 23, 115].

In fact, in perovskite NCs, excitons can also transport by diffusion. The diffusion of excitons and its effect on the optical properties of perovskite NCs will be discussed in chapter 6.

2.2.4 Colloidal metal halide perovskite nanocrystals

The huge success in photovoltaics makes metal halide perovskites also candidates for other optical and optoelectronic applications. Lasers and light emitting diodes (LEDs) based on metal halide perovskites have been reported [22, 23, 122, 123]. However, the early studies of perovskites mainly focused on bulk-like films or crystals. It is known that colloidal semiconductor NCs exhibit unique properties and advantages compared with bulk materials such as narrow PL spectra with broad tunability and high PLQYs [78]. Therefore, attemps were made to synthesize colloidal metal halide perovskite NCs and the first non-template synthesis of colloidal $MAPbBr_3$ perovskite nanoparticles was reported in 2014 [24].

It is demonstrated that the the obtained colloidal $MAPbBr_3$ nanoparticles exhibit a size of ~6 nm, as shown in figure 2.12 (a). The Bohr radius of exciton in $MAPbBr_3$ perovskite is estimated to be ~1.4 nm according to

$$a_B = \frac{\varepsilon}{\varepsilon_0}\frac{m_0}{\mu}a_H\,, \tag{2.20}$$

where ε_0 and ε are the dielectric constants of vacuum and the material, respectively, m_0 is the mass of free electron, μ is the reduced mass of the exciton given by equation 2.7, and a_H is the Bohr radius [99, 124].

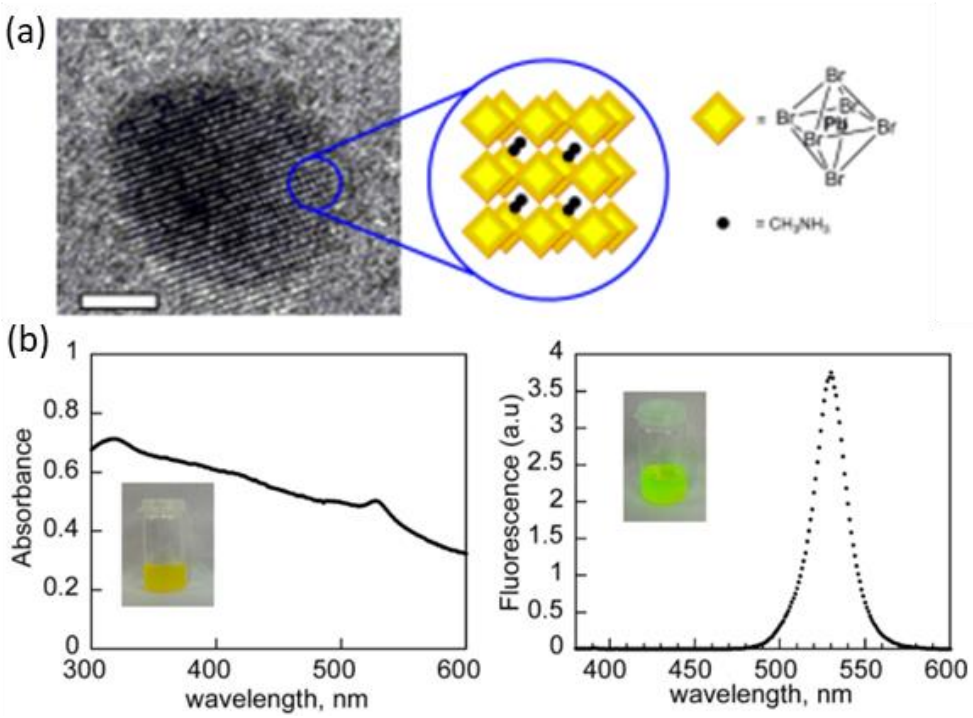

Figure 2.12: (a) Colloidal $MAPbBr_3$ perovskite nanoparticles obtained by a non-template synthesis approach, the scale bar is 2 nm. (b) Absorption (left) and PL (right) spectra of colloidal $MAPbBr_3$ nanoparticles. The insets are the corresponding photographs. Reproduced with permission from ref [24], copyright 2014 American Chemical Society.

As the size of the colloidal $MAPbBr_3$ nanoparticles is comparable to a_B, a weak quantum confinement was observed. The absorption and PL spectra of colloidal $MAPbBr_3$ perovskite nanoparticles presented in figure 2.12 (b) show a blueshift in comparison with the bulk-like $MAPbBr_3$ perovskite. The PLQY of the colloidal nanoparticles is relatively high, around 20%.

The emergence of colloidal perovskite NCs not only broadens the optoelectronic application of perovskite but also attracts a deeper exploration into the optical and other fundamental properties

of these NCs. In this thesis, the shape, size and dimensionality of the colloidal metal halide perovskite NCs are controlled and their optical properties are studied.

3. Materials and sample preparation

This chapter presents the preparation of metal halide perovskite NCs with various shapes. Essentially, two different methods are used in this work, first is the two-step reprecipitation method and second is the single-step ultra-sonication method. Details of the sample preparation using these two methods are given in the following.

3.1 Reprecipitation method

Reprecipitation is a common method for NC preparation which involves two steps as schematically shown in figure 3.1. In brief, in the first step, the precursors are dissolved in good solvent mixed with capping ligand. The adding of bad solvent will induce the precipitation of crystals from the solvent due to a change in solubility. The growth of the crystal is restricted by the long-chain ligand thus forming NCs with smaller size or lower dimensionality.

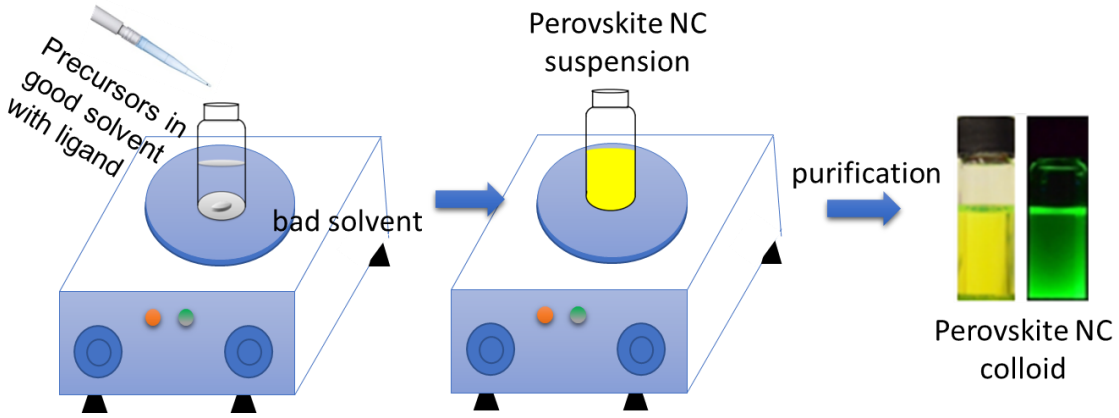

Figure 3.1: Schematic illustration of reprecipitation method for the synthesis of colloidal metal halide perovskite NCs.

3.1.1 Organic-inorganic perovskite nanocrystals

Organic-inorganic perovskite ($MAPbBr_3$) NCs were synthesized through reprecipitation method and the thickness of the NCs can be controlled to obtain thin sheets. Methylammonium and octylammonium bromide (MABr and OABr) precursor powders were prepared by reacting methylamine or octylamine solution with HBr in methanol, followed by a removal of solvent using rotating evaporation. To synthesize $MAPbBr_3$ perovskite NCs, first, $PbBr_2$ and a same molar amount of MABr powders or MABr/OABr mixture were dissolved in dimethylformamide at 80 °C. Then bad solvent toluene was injected and the clear solution turned cloudy which indicates the precipitation of perovskite NCs. After 3 minutes, the solution containing perovskite crystals were centrifuged at 3000 rpm for 10 min and the precipitates were redispersed in toluene. The thickness of the perovskite NCs can be controlled by varing the ratio between OABr and MABr. Scanning electron microscope (SEM) images show that the shape of the NCs transform from 3D cube to 2D thin sheet when increasing the OABr ratio, while the crystal structure almost maintains from X-ray diffraction (XRD) measurement as shown in figure 3.2.

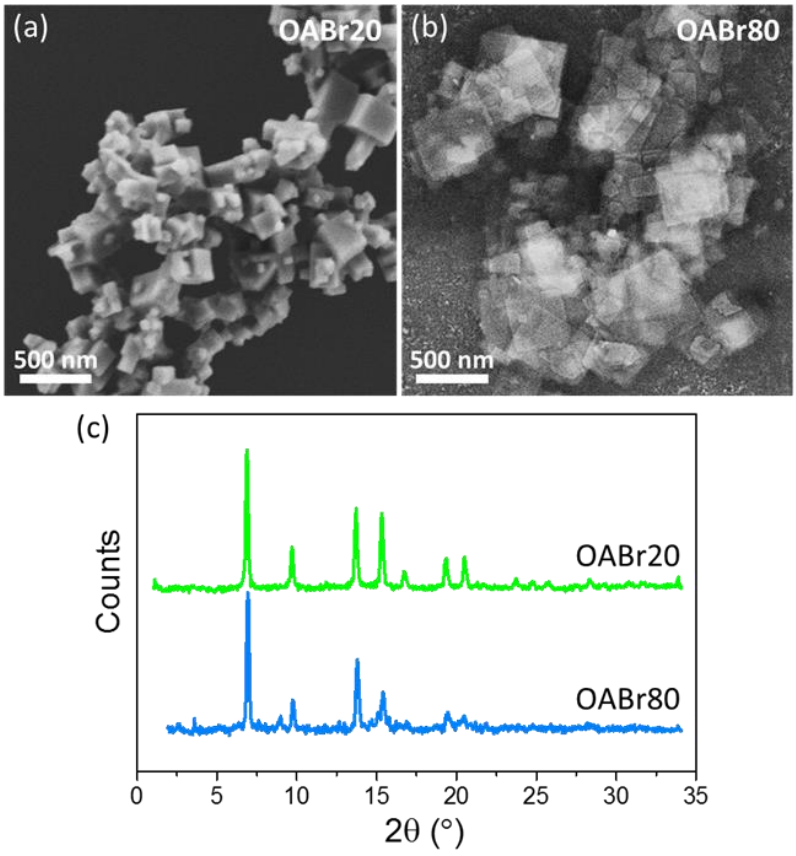

Figure 3.2: SEM images of $MAPbBr_3$ perovskite NCs. (a) 3D cubes obtained by using small OABr amount and (b) 2D sheets using large OABr amount. (c) XRD patterns of the corresponding perovskite NCs.

3.1.2 All-inorganic perovskite nanocrystals

All-inorganic perovskite ($CsPbBr_3$) NCs with controllable thickness were also prepared through reprecipitation method. First of all, Cs-oleate and $PbBr_2$-ligand solution were prepared as precursors. 0.1 mmol Cs_2CO_3 powders were dissolved in 10 ml oleic acid by heating to obtain Cs-oleate solution. $PbBr_2$-ligand solution was prepared by dissolving 0.1 mmol $PbBr_2$ powders in 10 ml toluene mixed with 0.1ml oleic acid and oleylamine. In a typical synthesis of $CsPbBr_3$ nanoplatelets (NPls), Cs-oleate solution was added into $PbBr_2$ precursor solution at room temperature followed by injection of bad solvent acetone to precipitate the $CsPbBr_3$ NPls. The thickness of the $CsPbBr_3$ NPls is tuned by changing the ratio between Cs-oleate and $PbBr_2$ precursor solutions as well as the amount of acetone. Higher Cs to $PbBr_2$ ratio and larger amount of acetone led to the formation of thicker NPls. The precipitated NPls are extracted from the suspension by centrifugation and redispersed in hexane to form colloidal solutions. The photos of the colloidal $CsPbBr_3$ perovskite NPls with different thicknesses as well as the transmission electron microscope (TEM) image are presented in figure 3.3.

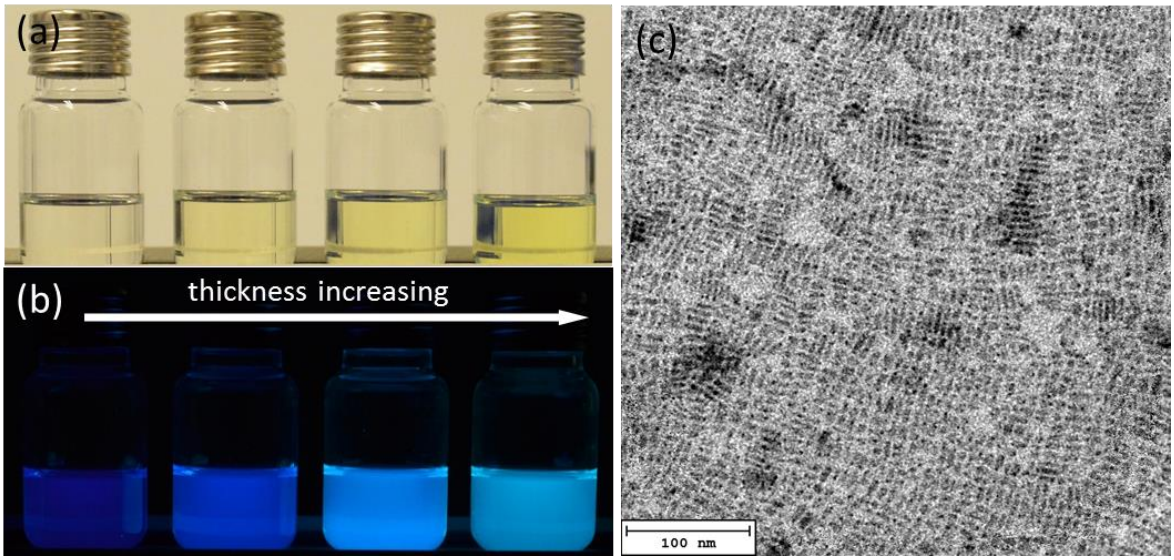

Figure 3.3: Photographs of $CsPbBr_3$ perovskite NPl dispersions under (a) room light and (b) UV light. (c) TEM image of $CsPbBr_3$ perovskite NPls.

3.2 Ultrasonication method

Aside from the reprecipitation method, ultrasonication method was also used to synthesize colloidal $CsPbX_3$ (X=Cl, Br, I or their mixtures) perovskite NCs. The sonication method is a single-step method, where all precursor powders and ligands are loaded in organic solvent such as octadecene and the reaction is initiated by a tip-sonicator. During the course of sonication, perovskite NCs are formed, indicated by the color change of the colloidal solution. After the completion of reaction, perovskite NCs are purified by centrifugation. Perovskite NCs with various compositions and shapes can be obtained by changing the precursors or reacting conditions. This ultrasonication method is illustrated in figure 3.4.

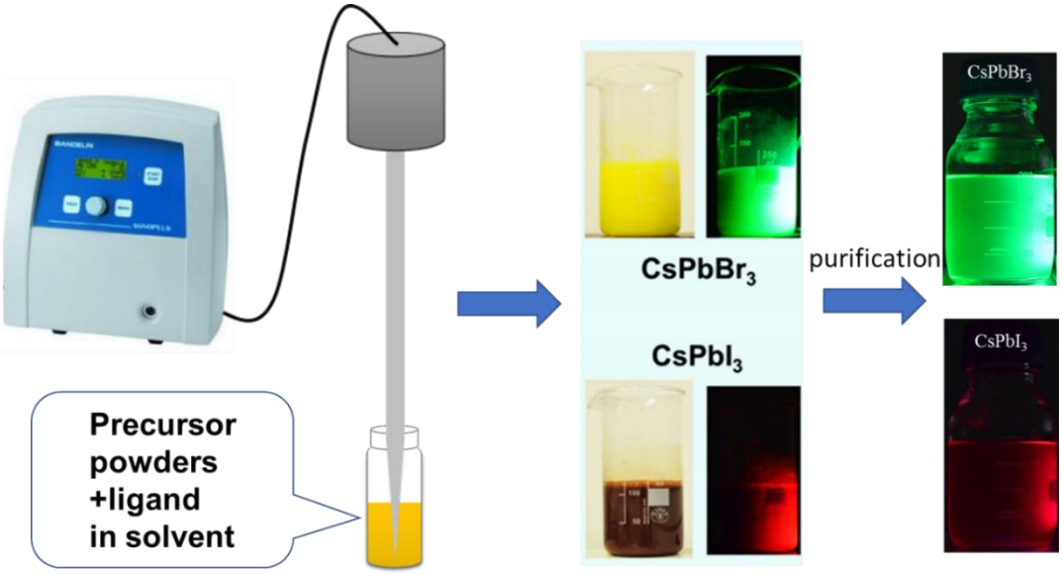

Figure 3.4: Ultrasonication method for the synthesis of $CsPbBr_3$ and $CsPbI_3$ perovskite NCs.

3.2.1 $CsPbX_3$ perovskite nanocubes

0.1 mmol Cs_2CO_3 and 0.3 mmol PbX_2 powders were added into 10 ml 1-octadecene solvent with 0.5 ml oleic acid and 0.5 ml oleylamine ligand. Then the mixture was tip-sonicated at a power of 30W for 10 min to ensure a sufficient reaction. Afterwards, the NC suspension was centrifuged at 9000 rpm for 10 min to get rid of unreacted precursors. Then the sediment was redispersed in 5 ml hexane under mild sonication, followed by a 2000 rpm centrifugation to discard large crystals. TEM images obtained at different reaction time indicating the seeded growth of $CsPbBr_3$ perovskite NCs are shown in figure 3.5 (a)-(c). High resolution TEM (HRTEM) image and

crystallography diffraction patterns confirming the crystallinity of $CsPbBr_3$ NCs is given in figure 3.5 (d). 2D $CsPbBr_3$ NPls can also be obtained by decreasing the molar ratio between Cs_2CO_3 and $PbBr_2$ as shown in figure 3.5 (e).

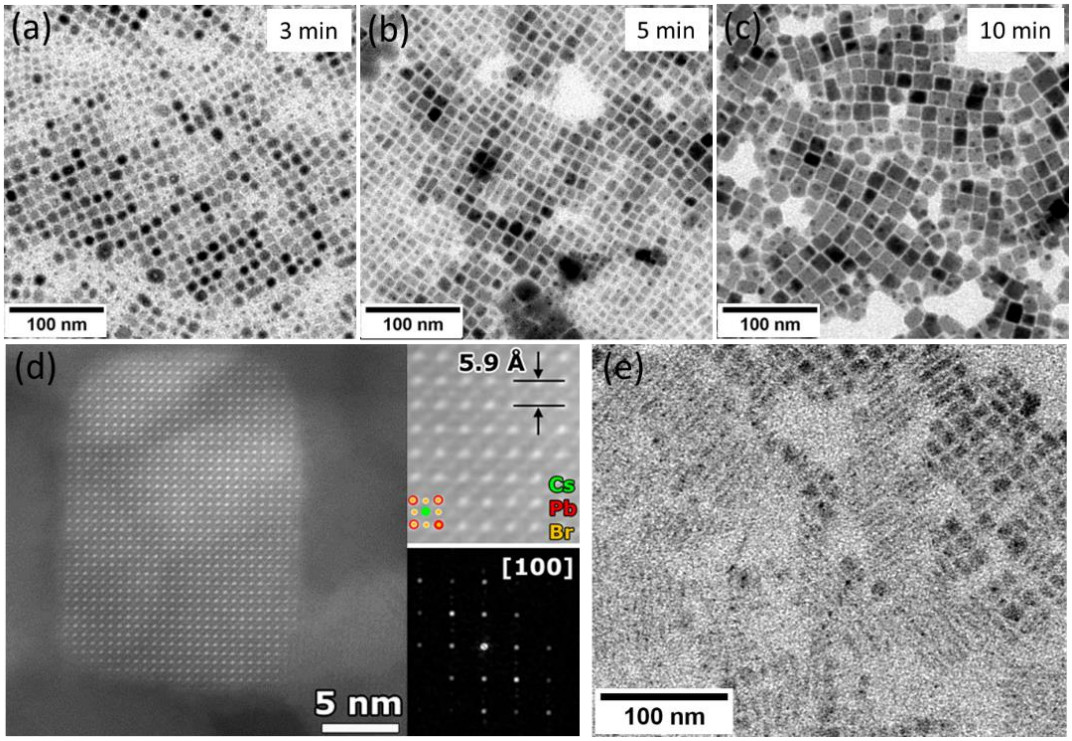

Figure 3.5: (a)-(c) TEM images of $CsPbBr_3$ perovskite NCs obtained at different reaction times. (d) HRTEM image of a single $CsPbBr_3$ NC and the crystallography diffraction pattern. (e) TEM image of colloidal $CsPbBr_3$ NPls obtained by decreasing the molar ratio between Cs_2CO_3 and $PbBr_2$.

3.2.2 $CsPbX_3$ perovskite nanowires

$CsPbBr_3$ nanowires (NWs) were prepared using a similar sonication approach with nanocubes but a prolonged reaction time. Specifically, 0.1 mmol Cs_2CO_3 and 0.3 mmol $PbBr_2$ together with 0.5 ml oleylamine and 0.5 ml oleic acid were loaded in 10 ml octadecene. The mixture was tip-sonicated at a power of 25 W for 60 min and then centrifuged at 5000 rpm to obtain NWs in the sediment. The obtained $CsPbBr_3$ perovskite NWs were washed with hexane for three times and redispersed in hexane. NWs containing Cl or I composition were obtained by doing halide ion exchange on the $CsPbBr_3$ perovskite NWs. Photos and SEM images of NWs are presented in figure 3.6.

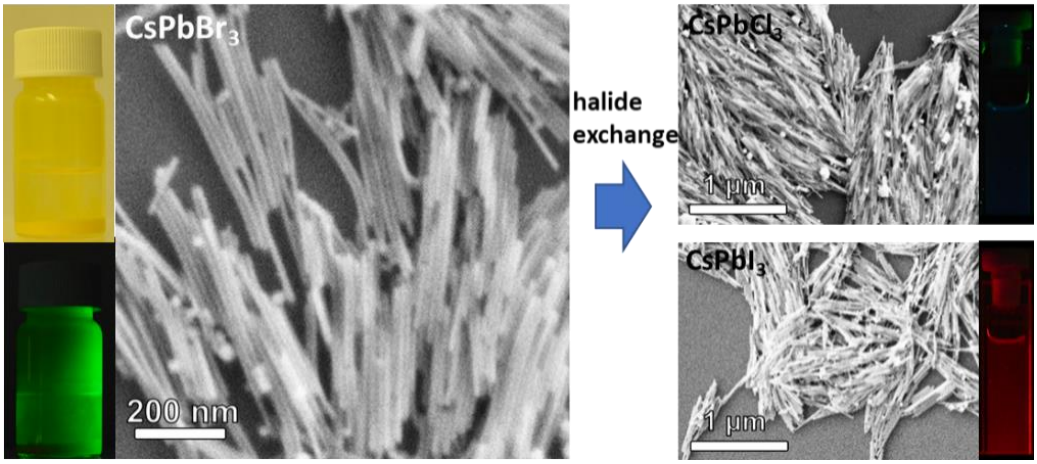

Figure 3.6: $CsPbBr_3$ perovskite nanowires prepared by ultrasonication method and $CsPbCl_3$/$CsPbI_3$ NWs obtained by doing halide ion exchange on the $CsPbBr_3$ NWs.

3.2.3 $CsPbBr_3$ perovskite supercrystals

Tip-sonication method was also used to fabricate $CsPbBr_3$ perovskite supercrystals. 1 mmol Cs_2CO_3 and 3 mmol $PbBr_2$ powders were loaded in 10 ml 1-octadecene. After adding 1.5ml oleic acid and 1.5ml oleylamine, the mixture was tip-sonicated at 30W for 30 minutes. Afterwards, the colloidal solution was cooled down and centrifuged at 6000rpm for 15min to obtain residual $CsPbBr_3$ supercrystals, which consist of NC subunits and exhibit bright PL as shown in figure 3.7.

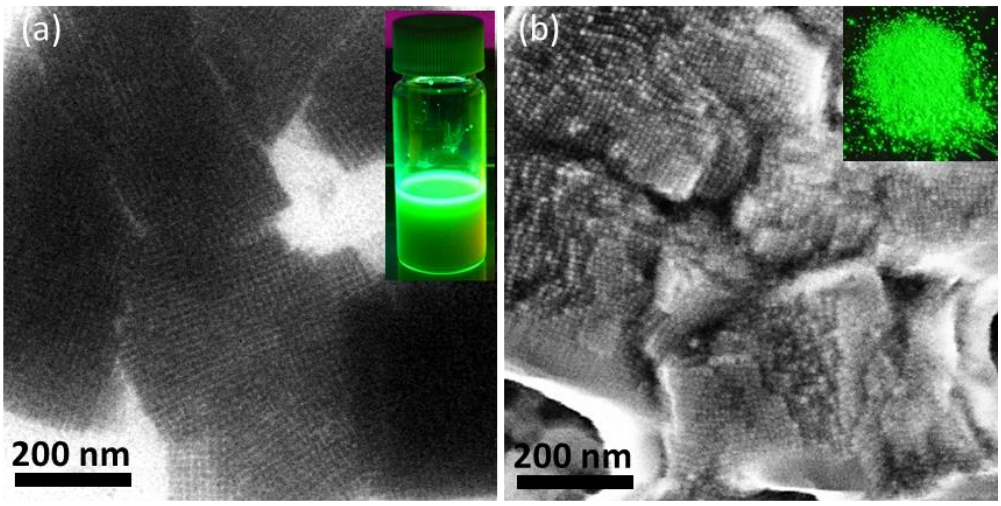

Figure 3.7: (a) TEM image of colloidal $CsPbBr_3$ supercrystals. (b) SEM image of dried $CsPbBr_3$ supercrystals. Insets are the corresponding samples under UV light.

4. Experimental setups

This chapter gives information on the experimental setups used in this work, including both optical spectroscopy and other morphological measurements.

4.1 Optical spectroscopy

Steady-state absorption and photoluminescence spectroscopy as well as time-resolved photoluminescence spectroscopy are used to study the optical properties of perovskite NCs.

4.1.1 Absorption spectroscopy

With a sample inserted into the light path, the incident light will be absorbed and scattered by the sample. A *Cary 5000* spectrophotometer (Agilent Technologies) was used to give information of this process. In principle, a flash Xenon lamp is used as a source to generate white light with broad wavelength distribution. Then different wavelength is isolated by a monochromator to obtain monochromatic light. The intensity of the light before and after passing through the sample is measured with a photodetector.

The wavelength dependent absorbance $A(\lambda)$ is given by

$$A(\lambda) = -\log_{10}\left(\frac{I(\lambda)}{I_0(\lambda)}\right), \tag{4.1}$$

where $I_0(\lambda)$ and $I(\lambda)$ are the intensity of light before and after passing through the sample, respectively.

According to the Beer-Lambert Law, the intensity of the light transmitted through the sample at wavelength λ is determined by

$$I(\lambda) = I_0(\lambda) \cdot e^{-\varepsilon(\lambda) l c}. \tag{4.2}$$

Here, $\varepsilon(\lambda)$ is the extinction coefficient per mole of NCs (L/mol×cm), c is the molar concentration of the NCs (mol/L), and l is the thickness of the sample (cm). With the thickness of the sample already known, the concentration of the NCs can be calculated from the absorbance according to

$$c = \frac{A(\lambda)}{l\varepsilon(\lambda)}. \tag{4.3}$$

4.1.2 Photoluminescence spectroscopy

Photoluminescence (PL) emission and photoluminescence excitation (PLE) spectroscopy are used to give information on the steady-state photoluminescence of light emitting perovskite samples. A Xenon lamp provides a broad white light spectrum and a certain wavelength is selected to serve as a source. The emitted photons are collected by a photodiode array and the spectrum is recorded in the form of intensity versus wavelength. For PL measurement, a fixed excitation wavelength is used and the intensity of the PL emission is measured as a function of wavelength. While for PLE measurement, a fixed wavelength selected from the PL spectrum is used and the intensity of light which can excite this specific PL wavelength is recorded as a function of wavelength.

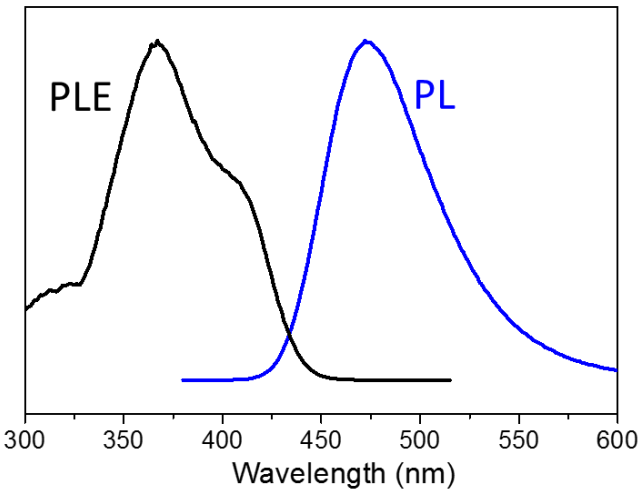

Figure 4.1: PL and PLE spectra of a Coumarin 102 dye solution (in methanol).

Two fluorescence spectrometers were used to measure the PL and PLE spectra. A Cary Eclipse photospectrometer (Agilent Technologies) was used to measure the PL of colloidal samples and a Fluorolog 3-22iHR fluorescence spectrometer (HORIBA Jobin-Yvon) was used to measure the PL and PLE spectra of samples on substrate as well as liquid samples with weak fluorescence. The

sensitivity for the latter one is higher due to the incorporated R928P photomultiplier (PMT). The PMT is mounted 90º with respect to the excitation light path and it needs to be cooled to 9 ºC during operation. It can detect the photons in the UV-visible range with the wavelength from 290 nm to 880 nm. Figure 4.1 shows the PL and PLE spectra of Coumarin 102 dye as an example.

4.1.3 Photoluminescence quantum yield

In general, the term quantum yield or quantum efficiency reflects how efficient one event can be converted from another. In a fluorescence system, this represents the efficiency of photon emission induced by photon excitation. The photons with suitable energy can be absorbed to stimulate the electrons to higher states and photons are emitted once the electrons go back to lower energy state through radiative relaxation. The ratio between the total number of the emitted photons and the absorbed ones is the photoluminescence quantum yield (PLQY), denoted as

$$\Phi_{\mathrm{PL}} = \frac{\int N_{em}(\lambda)d\lambda}{\int N_{abs}(\lambda')d\lambda'}, \tag{4.4}$$

Where Φ_{PL} is the PLQY. $\int N_{em}(\lambda)d\lambda$ and $\int N_{abs}(\lambda')d\lambda'$ represent the number of emitted and absorbed photons, respectively.

There are two main approaches to determine the PLQY of the studied system, i.e. (a) absolute PLQY measurement and (b) relative PLQY measurement.

(a) Absolute PLQY.

The absolute PLQY measurement requires the determination of the number of emitted photons and absorbed photons responsible for the emission, thus that the PLQY can be calculated according to the equation 4.4. Experimentally, an integrating sphere is used to collect all the photons involved in an excitation cycle. The sphere is incorporated in the Fluorolog 3-22iHR fluorescence spectrometer. As shown in figure 4.2 (a), a sample is mounted in the center of integrating sphere, an incident light with certain wavelength is guided into the sphere and partial of the photons are absorbed by the sample to induce photon emission. The residual incident photons that are not absorbed by the sample are collected together with the emitted photons from the output side of the integrating sphere. A spectrum covering both the excitation and emission range is taken on a blank

reference sample thus to determine the incident light as well as the emission baseline. Figure 4.2 (b) shows a representative result from absolute PLQY measurement on a fluorescence dye. The spectrum in black color is from the blank reference while the red one is from the sample.

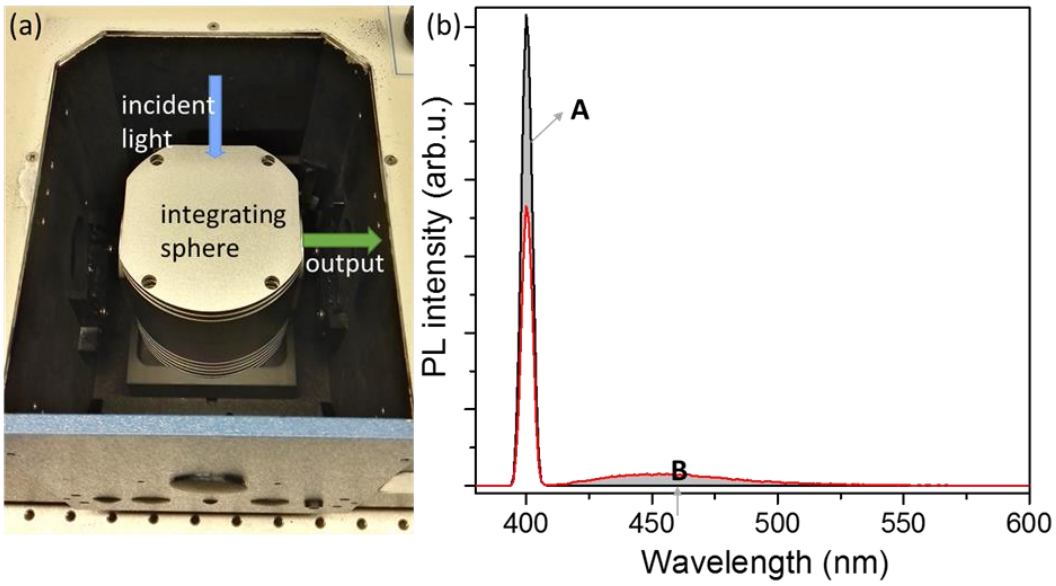

Figure 4.2: (a) Absolute PLQY measurement using an integrating sphere and (b) A representative absolute PLQY measurement result of a fluorescence dye solution (Coumarin 102 in methanol).

The number of absorbed photons is determined by the difference between the integral of input and output excitation photons (area A), and the number of emitted photons is calculated by integrating the emission spectrum over the emission wavelength after subtracting the baseline (area B). The absolute PLQY is thus calculated by

$$\Phi_{PL} = \frac{\int I_{em,sample}(\lambda)d\lambda - \int I_{em,blank}(\lambda)d\lambda}{\int I_{ex,blank}(\lambda')d\lambda' - \int I_{ex,sample}(\lambda')d\lambda'} = \frac{area\ B}{area\ A}. \quad (4.5)$$

The absolute PLQY measurement can be used for both solid and liquid samples.

(b) Relative PLQY

Instead of directly counting the number of emitted and absorbed photons in absolute PLQY measurement, relative PLQY measurement relies on standard fluorescence dye solutions with known Φ_{PL}. They serve as references for determining the PLQY of the samples through a

comparative way. This approach is usually applied on liquid samples, for example, colloidal NC dispersions. The underlying principle is that solutions with identical absorbance at the same excitation wavelength are considered to absorb an equal number of photons, thus that the integral of the PL emission excited by this wavelength is connected with the PLQY of the measured sample. Therefore, by keeping a same number of absorbed photons, and comparing the integrated PL of a sample with a reference, the PLQY of the sample can be calculated based on the known Φ_{PL} of the reference dyes.

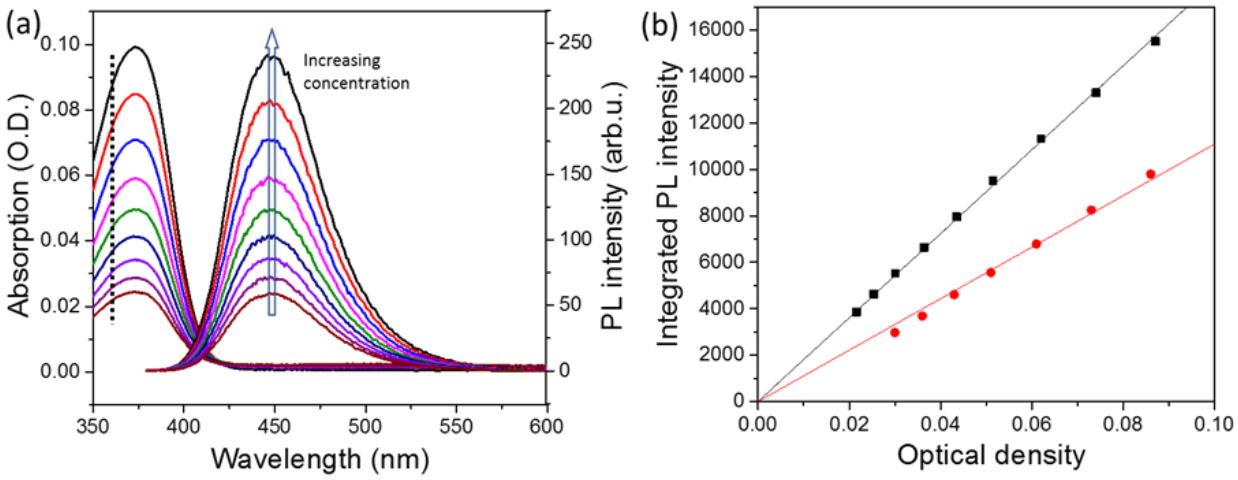

Figure 4.3: (a) Absorption and PL spectra of a reference dye (Coumarin 102). (b) Linear fitting of integrated PL versus optical density in reference dye (black) and sample (red).

In practical measuremnts, the following effects have to be taken into account: (i) fluorescence self-quenching effect at high concentration, (ii) the accuracy of Φ_{PL} of reference samples, (iii) different refractive indices of the host solvent for reference and the characterized samples. Therefore, a low concentration should be used for both reference and samples, absorbance in a 1 cm cuvette is kept below 0.1 at the excitation wavelength. Below this threshold, PL spectrum is measured at various concentrations. The integrated PL intensity versus optical density should show a linearity with a gradient ∇. At least two different reference dyes with known Φ_{PL} are used to enable cross-calibration thus ensure a trustable Φ_{PL} that can be used for the determination of the Φ_{PL} of characterized samples. Additionally, the different refractive indices (n) of the solvents for references and the samples are considered. Finally, Φ_{PL} of the samples can be calculated by

$$\Phi_{sample} = \Phi_{refernence} \cdot \frac{\nabla_{sample}}{\nabla_{reference}} \cdot \left(\frac{n_{sample}}{n_{reference}} \right)^2 . \quad (4.6)$$

Figure 4.3 gives an example for the relative PLQY measurement of a colloidal sample by using a fluorescence dye solution as a reference. The absorption and PL spectra of the dye solution with different concentrations are given in (a), similar measurement is performed on the diluted colloidal NC sample. PL increase gradient of the sample (∇_{sample}) and dye ($\nabla_{reference}$) are obtained from linear fitting, the refractive indices for the dye solvent (ethanol) and sample solvent (hexane) are $n_{reference}$ =1.36 and n_{sample} =1.37, respectively. With the $\Phi_{reference}$ known as 73%, Φ_{sample} is calculated to be 44%.

4.1.4 Time-resolved photoluminescence

Time-resolved photoluminesecence spectroscopy is an important analysis tool for understanding the physics processes involved in PL. It records the time-dependent intensity profile of the emitted light upon excitation. Experimentally, this can be achieved by using various techniques. In this thesis, a time-correlated single photon counting (TCSPC) system was used to study the time-resolved PL. A schematic of the measurement system is shown in figure 4.4.

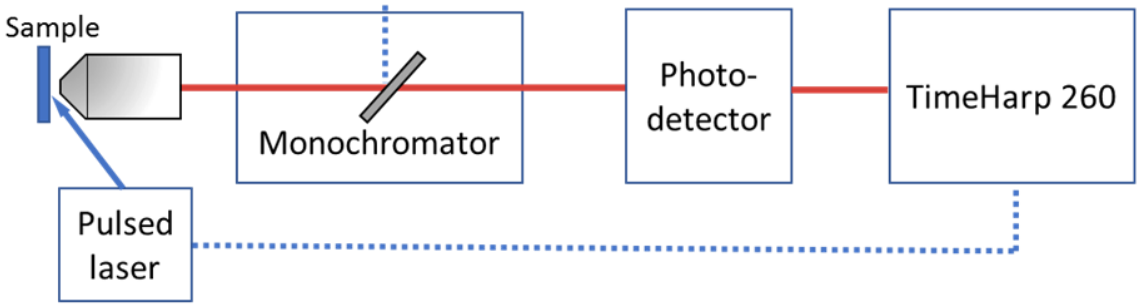

Figure 4.4: Schematic illustration of TCSPC system for time-resolved PL measurement.

A Timeharp 260 (PicoQuant) photon counter connected with a photodetector (avalanche photodiode) is combined with a monochromator (Princeton Instruments). The method is based on the repetitive, precisely timed registration of single photons. A pulsed laser (NKT) with tunable wavelength and repetition rate is used as an excitation source. This laser system can directly provide an electrical synchronization signal (sync) so that the reference for the timing of the registered photons is defined. By sufficiently attenuating the laser power to ensure only one photon

emission per excitation cycle, the histogram of photon arrivals per time bin represents the time decay expected to be obtained from a "single shot" time-resolved analog recording.

The histogram data can then be used for fluorescence lifetime calculation. A typical result in time-resolved fluorescence experiment is a histogram with an exponential drop of counts towards later times, which can be written as

$$N_t(\lambda) = N_0(\lambda) \cdot \sum_i A_i e^{-t/\tau_i}, \tag{4.7}$$

where $N_0(\lambda)$ and $N_t(\lambda)$ are the initial counts of photons with wavelength λ and the counts at delay time, respectively. A_i is the amplitude of decay process i and τ_i is the time at which the population of the photons is reduced to $1/e$.

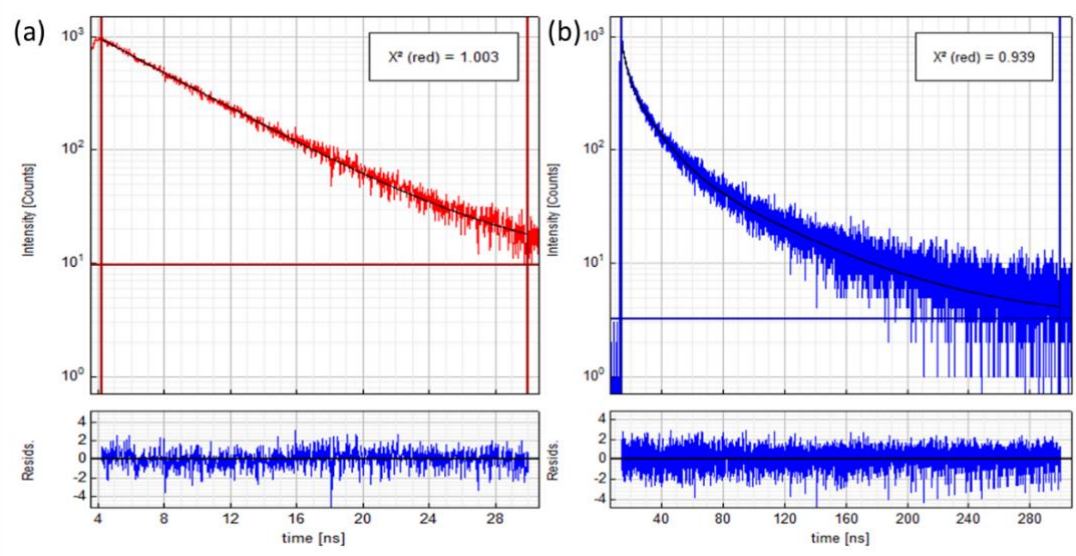

Figure 4.5: Time-resolved PL spectra showing a (a) monoexponential and (b) biexponential decay obtained by TCSPC system. Corresponding fittings are also included.

The time-resolved PL results are analyzed using a Fluofit software by fitting with either monoexponential or multiexponential function, and the amplitude of each component A_i and decay time τ_i can be obtained. Then the average fluorescence decay time τ_{av} can be obtained by an intensity weighted formula

$$\tau_{av} = \frac{\sum_i A_i \tau_i^2}{\sum_i A_i \tau_i} . \tag{4.8}$$

Figure 4.5 gives examples for monoexponential and biexponential PL decay curves obtained by the TCSPC system and the corresponding fittings by using Fluofit software.

4.1.5 Single-particle fluorescence spectroscopy

A single-particle spectroscopy setup was used to measure the PL spectra of a selected area or even a single crystal on a substrate. As schematically shown in figure 4.6, the substrate with sample is positioned in the vacuum chamber of a cryostat microscope (CryoVac GmbH and Co KG). The cryostat is placed on a xyz-movable stage and the internal temperature can be controlled between 5 K and 300 K by using liquid helium. The signal is collected using a microscope objective with a numerical aperture of 0.55 (Olympus, PlanFC model, 40-fold magnification) and a working distance of ~8 mm. The focus is adjusted in the z direction so that only a small area of the sample can be excited to obtain PL spectrum.

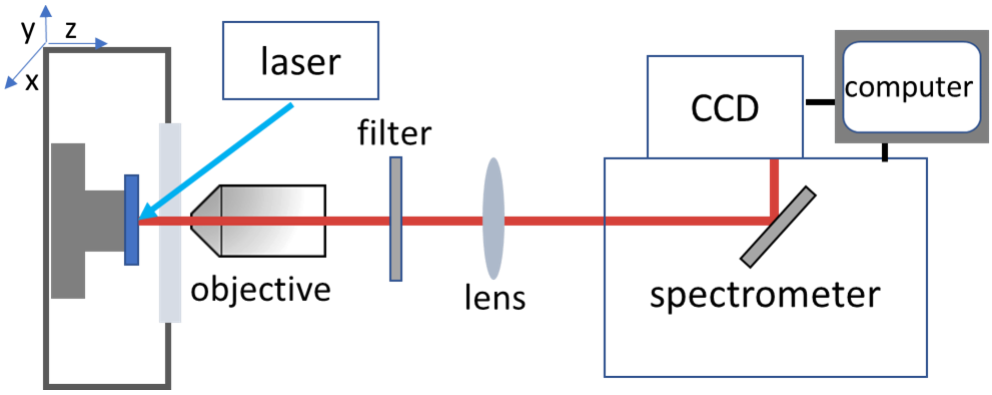

Figure 4.6: Schematic illustration of single-particle fluorescence spectroscopy setups.

Upon photoexcitation, the sample is viewed by a charge coupled device (CCD) using a maximum entrance slit and the position of the sample can be adjusted in xy direction. The selected area is moved to the center of view and the slit is sufficiently reduced to block the signal from other areas. In this way, only one or a few particles are present in view so that the PL spectrum of these particles can be recorded after switching from the CCD mode to the spectrometer mode. An example of this measurement is shown in figure 4.7, in which (a) is the image obtained by CCD with a wide

entrance slit, (b) is the image after reducing entrance slit which highlights the selected area, (c) is the PL mapping image and (d) is the integrated PL spectrum labeled in (c).

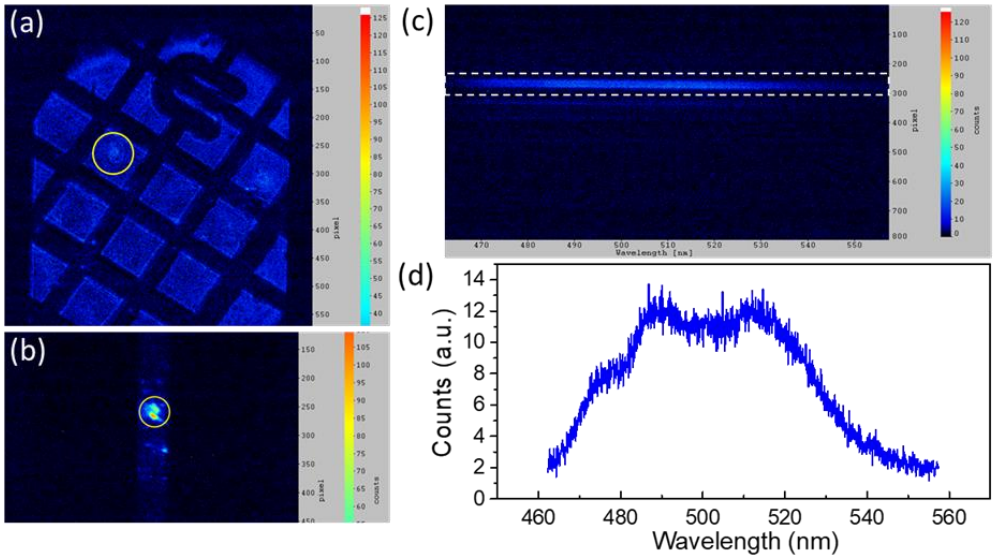

Figure 4.7: A representative single-particle PL measurement result. CCD images obtained with (a) a wide and (b) a narrow slit width. (c) PL mapping image and (d) the corresponding integrated PL profile.

4.1.6 Dark field microscopy and spectroscopy

A dark field optical microscope (Zeiss Axiotech 100) with an attached spectrometer (Princeton Instruments, Acton SpectraPro 300i) was used to measure the PL polarization anisotropy of luminescent single crystals or crystal arrays. The dark field aperture blocks the light which would propagate directly into the objective and produces a dark background with bright objects on it. As a result, the contrast of the sample is generally enhanced compared to normal bright field optical microscopy. The dark field microscopy is combined with a camera (Canon EOS 60D) for image acquiring. The system is used for PL polarization anisotropy measurement of perovskite NWs as schematically shown in figure 4.8 (a). Unpolarized light is used as excitation, going through the dark-field condenser and illuminating on the sample which is located on a moving stage. The scattered light as well as the PL from the sample are collected by the objective, making the sample visible in the microscope. The focus is adjusted in the z direction and the positioning of the target is precisely controlled in the xy direction to select a small area for measurement. Figure 4.8 (b) shows the image of a crystal under blue light illumination, the scattered blue light can be clearly seen. The PL can be separated from the scattered light by using a long path filter and the PL

spectrum is acquired by a spectrometer. To examine the polarizarion anisotropy of the PL, a polarizer is placed in front of the spectrometer and the PL spectrum at different polarizer angle is recorded.

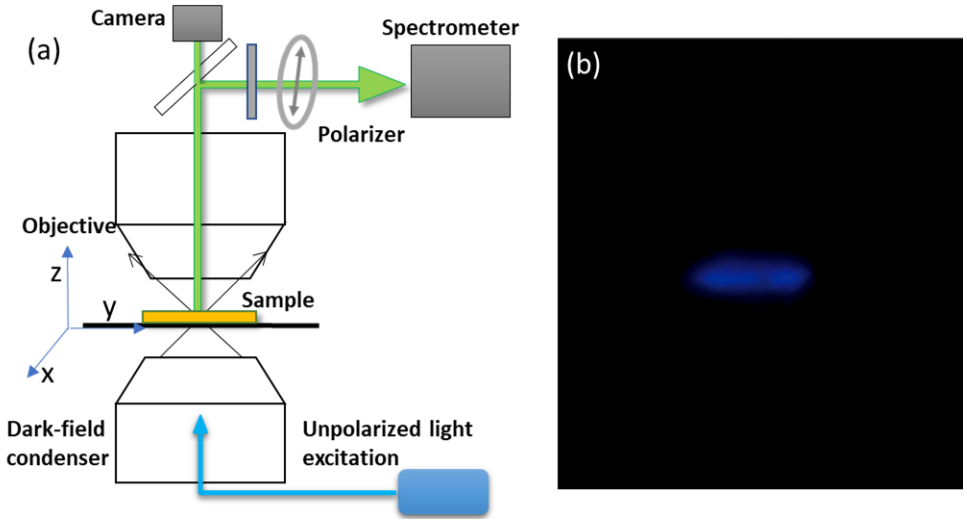

Figure 4.8: (a) Schematic illustration of dark field microscopy for the measurement of plolarizarion anisotropy of PL and (b) microscope image of the sample illuminated by blue light.

4.2 Morphological characterizations

Morphological characterizations are carried out to determine the shape and size of the NCs as well as their crystal structures. Details of the instruments are given below.

To measure the morphology and the size of nanostructures, a JEOL JEM 1011 transmission electron microscope is used to obtain TEM images, and the operating voltage is 80-100kV.

To determine the lattice parameter of perovskite NCs, HRTEM measurements are performed using a cubed FEI Titan microscope operating at 300 kV. The probe semi convergence angle is ~21 mrad.

SEM images are acquired using a Gemini Ultra Plus field emission scanning electron microscope at an electron accelerating voltage of 3 kV.

XRD measurements are carried out to determine the crystal phase structures of perovskite NCs. A BRUKER D8 ADVANCE diffractometer with an 8 keV Cu-Kα X-ray source is used for the XRD measurements.

5. Quantum size effects in low-dimensional lead halide perovskite nanocrystals

In chapter 2, it is introduced that the dimensionality of semiconductors has significant impacts on their optical properties. In this chapter, the dimensionality of both organic-inorganic hybrid perovskite ($MAPbBr_3$) and all-inorganic perovskite ($CsPbX_3$, X=Cl, Br, I) colloidal NCs are controlled and their optical properties are studied. It is demonstrated that the PL and absorption spectra of colloidal perovskite NCs show a significant blueshift with decreasing dimensionality from 3D to 2D, which is attributed to the strong quantum confinement in the 2D nanoplatelets (NPls). The thicknesses of the NPls are determined from the number of perovskite monolayers and confirmed by transmission microscope images. Considering the stacking nature of the 2D perovskite NPls, they can be seen as superlattice-like multiple quantum wells with capping ligands as barriers. Therefore, a Kronig-Penny model is used to quantitatively study the NPl thickness-dependent quantum confinement thus that the PL peak position can be correlated with the NPl thickness. Moreover, the thickness of $CsPbBr_3$ NPls can be precisely controlled in the monolayer level from 2 to 6 ML and they exhibit narrow emission and sharp excitonic absorption peaks. By modeling the absorption spectra of the colloidal NPls, it is found that the exciton binding energy gradually increases with the decrease of the NPl thickness. It is also discovered that the PLQYs of these NPls can be dramatically increased through a surface trap repair process, while their narrow PL emission and PL peak position are almost maintained.

5.1 Quantum confinement in $CH_3NH_3PbBr_3$ perovskite nanoplatelets

This section shows that the dimensionality of colloidal $MAPbBr_3$ perovskite NCs can be controlled from 3D to 2D. Colloidal 2D $MAPbBr_3$ perovskite NPls with different thicknesses are obtained and their thickness-dependent optical properties are studied. The quantum confinement in the NPls is also quantitatively studied by using theoretical models.

5.1.1 Blueshift in PL and absorption induced by quantum confinement

The dimensionality of $MAPbBr_3$ NCs are controlled by varying the amount of octylammonium bromide (OABr) as detailed in the experimental section. Figure 5.1 (a) shows that the PL and absorption spectra exhibit a significant blueshift while increasing the OABr content from 0% to 100%. At 0% OABr content, the absorption spectrum shows an onset at ~510 nm and a corresponding narrow and symmetric PL emission peak at 520 nm can be observed in the PL spectrum. The colloidal NCs exhibit a green emission under UV light as shown in the inset. With the OABr content increasing to 60%, the main PL peak slightly blueshifted to 510 nm and a shoulder emerges at shorter wavelength, the solution shows a blueish green emission color under UV light illumination.

Associated with the blueshift in PL, absorption peaks arise at shorter wavelength and become more prominent with the OA content increases. In the case of 80% OABr sample, both absorption and PL are further blueshifted with respect to the 60% OABr sample. Notably, the 80% OABr sample shares the same PL and absorption peak positions with the 60% OABr despite that the peak intensity at shorter wavelength is higher, and the sample exhibits blue emission. In the extreme case of 100% OABr, the sample shows a nearly 100 nm blueshift in PL and absorption spectra with respect to the 0% OABr sample, and a violet color emission can be seen upon UV excitation. The substantial change in the optical properties of these perovskite NCs is closely related to the change of their dimensionality as depicted by the TEM images in figure 5.1 (b). In all samples, rectangular-shaped perovskite crystals with a size of 200-500 nm are observed. With OABr content increasing from 0% to 100%, a significant decrease in the contrast of the NCs can be observed, indicating the decreasing thickness of the NCs, as schematically illustrated in figure 5.1 (c).

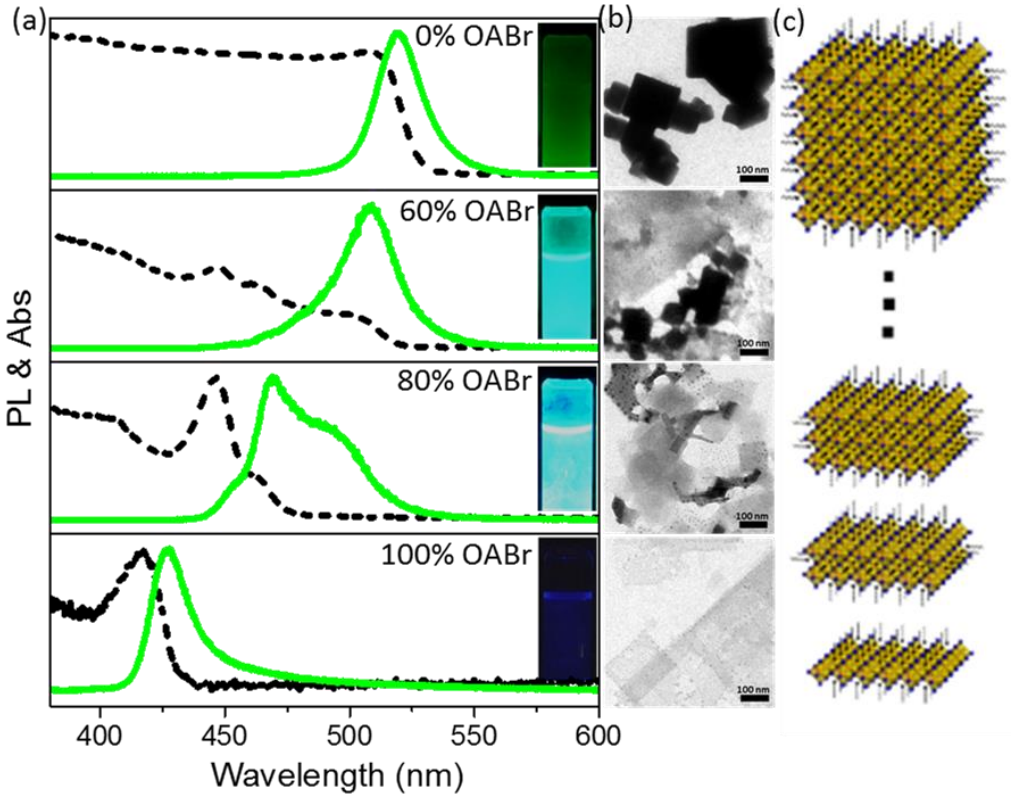

Figure 5.1: (a) PL (solid lines) and absorption (dashed lines) spectra of colloidal $MAPbBr_3$ perovskite NCs synthesized with different OABr content, insets show the photos of corresponding colloidal dispersions under UV light illumination. (b) TEM images of the NCs corresponding to (a), lower contrast indicates thinner structure. (c) Schematic presentation of the change in NC geometry from 3D bulk-like crystals to 2D NPls by increasing OABr content.

As displayed in figure 3.2 and figure 5.1, by using large OABr content, 3D perovskite crystals transform to 2D perovskite NPls with significantly decreased thickness. According to quantum mechanics, decreasing the thickness of the NPls down to the size of the exciton Bohr radius will lead to a significant spatial confinement of the charge carriers. The principle of quantum confinement can be shown by the smiplest model, i.e., particle in a 1D infinite potential well model. The wavefunction of the particle, ψ , is given by the Schrödinger equation. Considering an infinite quantum well model as shown in figure 5.2 (a), the time-dependent Schrodinger equation for the particle in one spatial dimension (along the x axis) is written as

$$-\frac{\hbar^2}{2m}\frac{\partial^2\psi(x,t)}{\partial x^2}+U(x)\psi(x,t)=i\hbar\frac{\partial\psi(x,t)}{\partial t} \qquad (5.1)$$

The stationary eigenstates with energy E is given by the time-independent Schrödinger equation:

$$-\frac{\hbar^2}{2m}\frac{\partial^2\psi(x)}{\partial x^2}+U(x)\psi(x)=E\psi(x)\,. \tag{5.2}$$

The position-dependent potential $U(x)$ is

$$U(x)=\begin{cases}0, & 0<x<L\\ \infty, & x\le 0,\ x\ge L\end{cases} \tag{5.3}$$

with L representing the thickness of the quantum well.

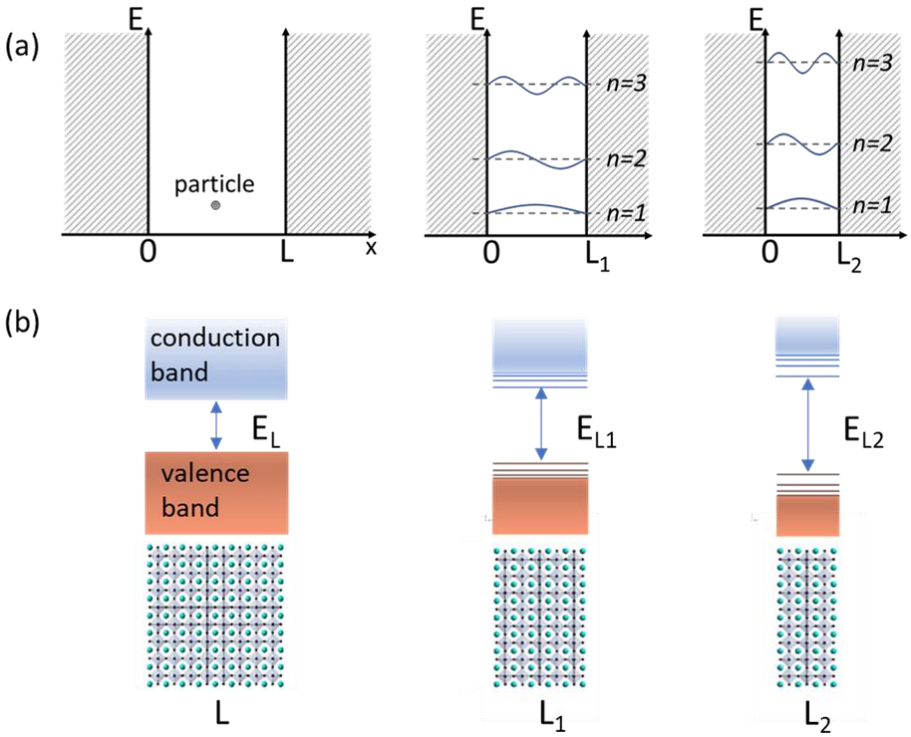

Figure 5.2: (a) Model of particle in a 1D quantum well with infinite large barrier outside the well. According to quantum mechanics, the particle in the quantum well have nonzero quantized energies. The energy levels are dependent on the width of the well. (b) Schematic illustration of the conduction and valence bands in perovskite crystals with decreasing thickness. Energy near to the band edge becomes quantized and energy gap increases, giving the tendency of $E_{L2}>E_{L1}>E_L$.

The particle can move freely inside the well but cannot penetrate the potential wall, so that the boundary condition for the wavefunction ψ is

$$\psi(0) = \psi(L) = 0\,. \tag{5.4}$$

The solution for the wavefunction is

$$\psi(x) = A\sin k_n x,\ x = \frac{n\pi}{L},\ n = \mathbb{Z}\,. \tag{5.5}$$

The corresponding energy of the particle is

$$E_n = \frac{\hbar^2 {k_n}^2}{2m} = \frac{n^2\pi^2\hbar^2}{2mL^2}\,, \tag{5.6}$$

where $\hbar$ is the reduced Plank constant and *m* is the mass of the particle.

Equation 5.6 indicates that the particle in the well has a nonzero quantized energy characterized by a quantum number *n* (*n*=integer). The energy is inversely proportional to the mass of the particle and the square of the quantum well thickness, so that particle in quantum well with smaller width is expected to show larger quantization energy as schematically shown in figure 5.2 (a).

As discussed earlier, the 2D $MAPbBr_3$ NPls have a similar lateral size with the 3D bulk-like crystals but a significantly decreased thickness. Therefore, the NPls are only confined in one dimension and can be seen as anologues of the ideal 1D potential well model. As shown in figure 5.2 (b), for the bulk perovskite crystals with large size in all three dimensions, there is no quantum confinement effect thus the crystals show quasi-continuous CB and VB. However, when the thickness of the crystal is dramatically decreased down to merely a few nanometers, the wavefunction of the carrier is spatially confined along the thickness direction thus that the allowed energy becomes quantized and shifts from the initial VBM and CBM. This effect results in an increased energy gap between the ground state and excited state, and energy gap increases with a further decrease of the NPl thickness ($E_{L2}>E_{L1}>E_L$) since the degree of the confinement is inversely related to the thickness of the NPl quantum wells according to equation 5.6.

5.1.2 Quantitative analysis of quantum confinement

As discussed above, the thickness of the perovskite NPls is a decisive factor for the quantum confinement, to be able to quantitatively analyze the quantum confinement, a determination of perovskite NPl thickness is necessary.

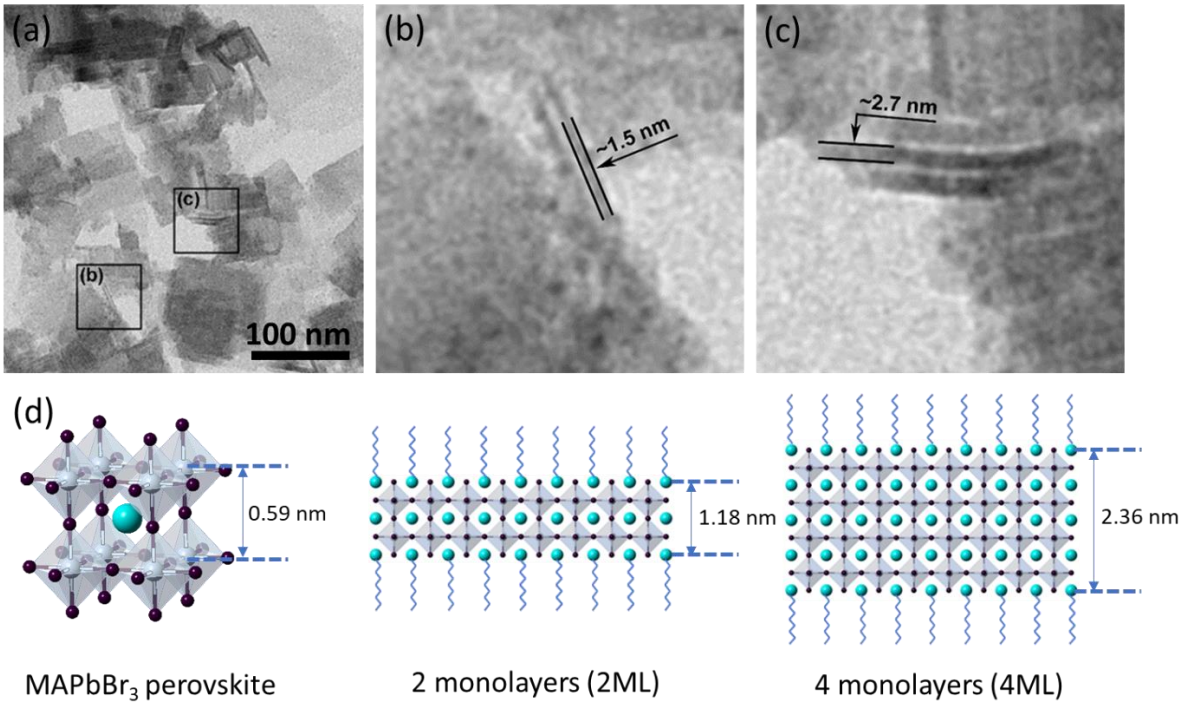

Figure 5.3: (a) TEM image of 80% OABr perovskite NPl sample on a large area. (b) and (c) High magnification TEM images of perovskite NPls standing on their sides corresponding to the labeled areas in (a). The thicknesses of the platelets in (b) and (c) are measured to be around 1.5 nm and 2.7 nm, respectively. (d) Schematic presentation of $MAPbBr_3$ perovskite lattice constant (0.59 nm) and side views of perovskite NPls containing two and four monolayers. The theoretical thickness of the corresponding NPls are 1.18 nm and 2.36 nm, respectively, matching well with the experimental results.

Figure 5.3 (a) shows the TEM image of 80% OABr sample, the low contrast indicates that the NPls are very thin. In some areas, for example, areas labeled as (b) and (c), the NPls stand on their sides, enabling a direct estimation of the NPl thickness from the TEM images. From the corresponding high magnification TEM images in Figure 5.3 (b) and (c), the thickness of the NPls are measured to be ~1.5 nm and ~2.7 nm, respectively. To make a precise determination of the perovskite NPl thickness, the crystal structure and lattice parameters of $MAPbBr_3$ perovskite need to be considered. The lattice constant is known as 0.59 nm [24], which means the thickness of a monolayer is 0.59 nm, therefore the thickness of $MAPbBr_3$ perovskite NPl containing two

monolayers (2ML) is supposed to be 1.18 nm and the 4ML NPls should have a thickness of 2.36 nm [124] as schematically shown in figure 5.3 (d). These values are consistent with the thicknesses determined from the TEM images in figure 5.3 (b) and (c).

The determined thickness of the colloidal $MAPbBr_3$ perovskite NPls can be correlated with the different PL peaks in figure 5.1 (a). The experimental PL peak positions from the spectra in figure 5.1 (a) are 427 nm, 455 nm, 470 nm, 480 nm and 518nm. According to previosu discussion, these peaks can be attributed to the NPls with thickness of 0.59 nm (1ML), 1.18 nm (2ML), 1.77 nm (3ML), 2.36 nm (4ML) and 2.95 nm (5ML), respectively, which is summarized in the table in figure 5.4 (a). To examine this correlation, a theoretical model for quantifying the quantum confinement is required. A simplest model is the infinite quantum well model which treats the charge carrier in the perovskite NPls as a particle in a 1D pntential well with infinite large barrier energy, as discussed earlier. In this model, the effective mass of the charge carrier inside the perovskite NPl needs to be considered and the quantum confinement effect can thus be determined according to equation 5.6, which is termed effective mass approximation (EMA).

(a)

number of layers (ML)	1	2	3	4	5
thickness L^{QW} (nm)	0.59	1.18	1.77	2.36	2.95
PL maxima (nm)	427	455	470	480	518

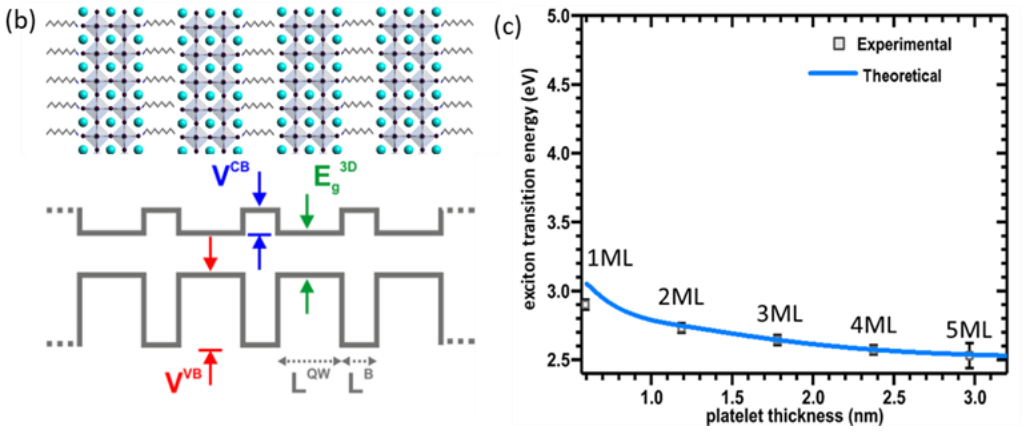

Figure 5.4: (a) Table summarizing the thicknesses and corresponding PL maxima of $MAPbBr_3$ perovskite NPls with different number of layers. (b) Schematic presentation of stacked perovskite NPls and the resultant periodic potential energy in the quantum well superlattice. (c) Experimentally (black squares) and

theoretically (blue line) determined exciton transition energies of $MAPbBr_3$ perovskite NPls with different thicknesses.

In fact, the quantum confinement in semiconductor nanostructures is generally treated using EMA, which can explain the PL blueshift with the decrease of NC size. Two confinement regimes need to be considered depending on the relation between the size of the nanostructure (d), and the exciton Bohr radius (a_B), i.e., the weak confinement regime and the strong confinement regime [125]. In the case of $d >> a_B$, a weak confinement regime is considered treating the electron-hole pair as a whole exciton, and the energy shift due to exciton confinement can be calculated by using the reduced mass of the exciton. In contrast, for $d << a_B$, a strong confinement regime is considered to treat the electron and hole as separate particles and calculate their respective confinement energies individually [125, 126]. As introduced in chapter 2, the Bohr radius of exciton in $MAPbBr_3$ perovskite is determined to be ~1.4 nm, in between the thicknesses of 2ML and 3ML NPls. Therefore, 1ML and 2ML $MAPbBr_3$ perovskite NPls are considered to be in the strong confinement regime while thicker NPls are in the weak confinement regime.

In fact, another effect may also contribute to the modification of the quantum confinement in these NPls, that is the stacking of these $MAPbBr_3$ perovskite NPls, which can be obviously seen from the TEM and SEM images shown earlier. As discussed in chapter 2 and depicted in figure 5.4 (b), stacking of the perovskite NPls enables the electron and hole wavefunctions to extend outside of the platelets, thus hybridizing with those from neighboring NPls and leading to the formation of minibands [124, 127]. This effect can be studied using the one-band effective-mass Kronig-Penney model. Here, this model is used to quantitatively correlate the quantum confinement with the thickness of $MAPbBr_3$ perovskite NPls. The separate dispersion relations for the electron and hole are written as

$$\cos(kL^{QW})\cosh(\alpha L^{B}) + \frac{1}{2}\left(\eta - \frac{1}{\eta}\right)\sin(kL^{QW})\sinh(\alpha L^{B}) = \cos(\delta)\,. \tag{5.7}$$

with $k = \sqrt{\frac{2m_{e(h)}^{QW}E_{e(h)}}{\hbar^2}}$, $k = \sqrt{\frac{2m_{e(h)}^{QW}E_{e(h)}}{\hbar^2}}$ and $\eta = \frac{\alpha m_{e(h)}^{QW}}{k m_{e(h)}^{B}}$.

Here, $E_{e(h)}$ is the quantization energies of the electron (hole), L^{QW} is the width of the quantum well (the thickness of the NPls) varying from 0.59 nm to 2.95 nm depending on the number of perovskite layers. L^B is the width of the barrier, being 0.15 nm. $m_{e(h)}^{QW}$ and $m_{e(h)}^{B}$ are the effective masses of electron (hole) in the quantum well and in the ligand barrier, respectively. $\delta=q(L^{QW}+L^B)$, with $q=2\pi n/L_c$ (n is integer and L_c is the length of the crystal lattice). By using the transfer matrix technique within the envelope function framework implemented to Kronig-Penney model, E_e and E_h can be obtained.

Furthermore, the impact of exciton binding energy E_b also needs to be considered. As discussed in chapter 2, the 2D $MAPbBr_3$ perovskite NPls are surrounded by organic ligands with small dielectric constant, the screening of the Coulomb interaction between electron and hole is decreased in these NPls. Therefore, the exciton binding energy of atomically thin perovskite NPls will be significantly increased compared to the corresponding 3D NCs.

Taking all the above mentioned factors into consideration, the theoretical exciton transition energy, E_x, can be written as

$$E_x = E_g^{3D} + E_e + E_h - E_b \,, \tag{5.8}$$

where E_g^{3D} is the bandgap energy of 3D bulk $MAPbBr_3$ perovskite without quantum confinement, E_e and E_h are the quantization energies of electrons and holes due to quantum confinement, respectively.

For weak confinement regime, the exciton binding energy is calculated according to

$$E_b = \left(\frac{\varepsilon}{\varepsilon_0}\right)^2 \frac{\mu}{m_0} R_H \,. \tag{5.9}$$

where R_H is the Rydberg constant, the effective mass for the electrons and holes are $m_e^{QW}=0.23m_0$ and $m_h^{QW}=0.29m_0$, respectively, and the dielectric constant is $\varepsilon^{QW}=3.29\varepsilon_0$ [128]. The effective mass of exciton is derived from

$$\frac{1}{\mu} = \frac{1}{m_e^{QW}} + \frac{1}{m_h^{QW}}, \tag{5.10}$$

In the case of the strong confinement regime, the exciton binding energy is calculated according to previous publication, i.e.

$$E_b = -\frac{e^2}{\varepsilon^{QW} L^{QW}} \left(\ln \frac{8\varepsilon^{QW} L^B}{\varepsilon^B a_B'} - 2C + 2\gamma_0 \right), \tag{5.11}$$

where ε^{QW} and ε^B=1.84ε_0 are the dielectric constants for the quantum well and barrier, respectively. The values are taken from literature as ε^{QW}=3.29ε_0 and ε^B=1.84ε_0. L^B is the width of the ligand barrier, C is Euler's constant, a_B' is the effective radius of exciton, and γ_0 is an eigenvalue independent on other parameter.

With input of all the necessary parameters described above, the theoretical exciton transition energy can be obtained, they are plotted as a function of NPl thickness as presented in figure 5.4 (c). The experimental exciton transition energies of perovskite NPls are obtained from the energy of PL maxima. It can be clearly seen that theoretical values match well with the experimental results, indicating a successful quantification of the quantum confinement in colloidal lead halide perovskite NCs.

5.2 MA replaced by Cs: tunable optical properties of $CsPbX_3$ perovskite NCs

In the previous section, it is shown that the optical properties of $MAPbBr_3$ perovskite NCs are tunable by decreasing their dimensionality from 3D nanocubes to 2D NPls. As introduced in chapter 2, the organic MA group can be replaced by an inorganic cation (for example, Cs^+) that can fit into the perovskite crystal lattice, yielding all-inorganic metal halide perovskites. Generally all-inorganic metal halide perovskites have relatively better stability compared to hybrid perovskite due to the fact that the organic cations are easy to decompose. Therefore, this section focuses on the tunable PL of $CsPbX_3$ (X=Cl, Br, I) perovskite NCs, achieved by either changing the NC dimensionality or halide composition.

5.2.1 $CsPbX_3$ nanocubes exhibiting weak quantum confinement

The optical properties (absorption and PL) of $CsPbX_3$ (X=halide) NCs are compared with those of the bulk film. The $CsPbBr_3$ perovskite NCs are prepared via a single-step ultrasonication approach as detailed in chapter 3 and the bulk $CsPbBr_3$ perovskite film is prepared using the method reported in ref [129]. The as-prepared NCs are dispersed in hexane or toluene while the bulk-like film is coated on glass substrate for PL and absorption measurements.

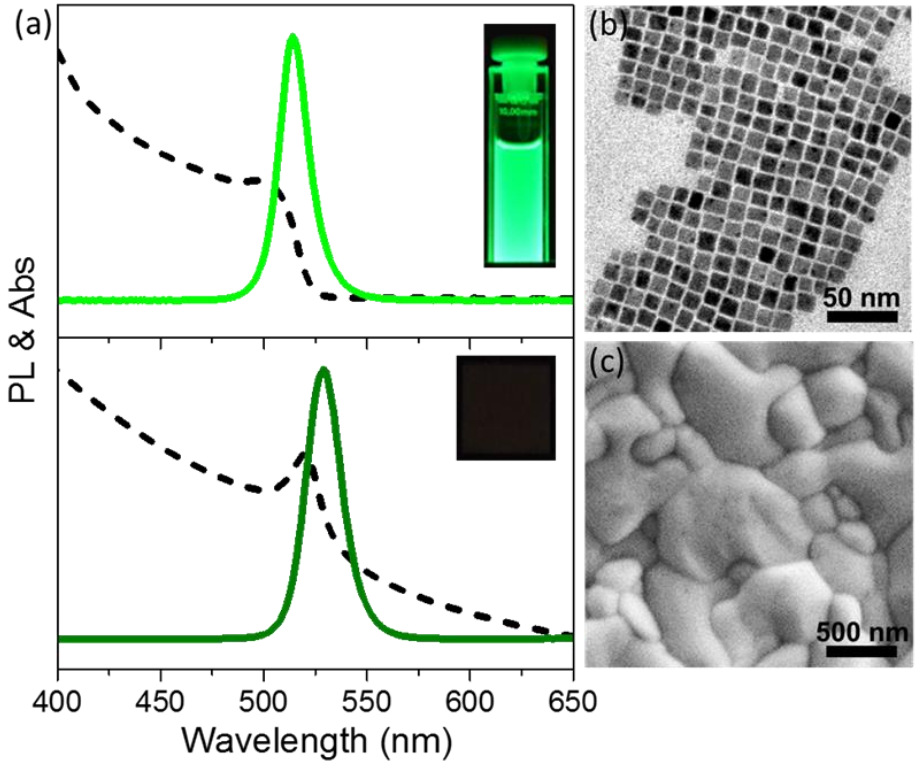

Figure 5.5: (a) PL (solid lines) and absorption (dashed lines) spectra of $CsPbBr_3$ perovskite nanocube colloid (top) and a $CsPbBr_3$ perovskite bulk-like film (bottom). The insets show the photos of the sample under UV light. (b) TEM image of $CsPbBr_3$ perovskite nanocubes and (c) SEM image of $CsPbBr_3$ bulk-like film.

Figure 5.5 (a) shows the PL and absorption spectra of the colloidal $CsPbBr_3$ NCs as well as the bulk-like film, with insets showing the photos of respective samples under UV light illumination. The corresponding TEM and SEM images are presented in figure 5.5 (b) and (c), respectively. For the $CsPbBr_3$ NCs, a cubic shape is observed, owing to the cubic structure of $CsPbBr_3$ perovskite crystals with Cs in the center of the cube surrounded by PbX_6 octahedras as introduced before. The

colloidal $CsPbBr_3$ nanocubes have a homogeneous size distribution in the range of 10-15 nm and the average size obtained from statistics measurement is ~14.3 nm [130]. Whereas in the case of bulk-like $CsPbBr_3$ perovskite film, large adjacent grains with a size range of 100-500 nm are observed in the SEM images. The colloidal dispersion of the $CsPbBr_3$ nanocubes exhibit an absorption onset at around 510 nm and a narrow emissision (FWHM ~20 nm) at 515 nm (figure 5.5 (a)). However, a clear excitonic absorption peak can be hardly distinguished, which may be ascribed to the small exciton binding energy that leads to an overlap between excitonic absorption and continuum absorption or a dissociation of excitons at room temperature [131, 132]. The $CsPbBr_3$ nanocube colloid shows an intensive PL emission with narrow linewidth. The full width at half maximum (FWHM) for the PL is around 20 nm, and the position for the PL maxima is around 515 nm. In contrast, bulk-like $CsPbBr_3$ film exhibits a PL peak at 532 nm with a full width at half maximum (FWHM) of ~ 25 nm. The PL peak position of the nanocube shows a 17 nm blueshift compared with that of the bulk-like film due to the quantum confinement effect. However, since the average size of the nanocubes (~14.3 nm) is larger than the exciton Bohr radius of $CsPbBr_3$ perovskite which is reported to be ~4 nm [131], the confinement effect is weak, thus that the PL of $CsPbBr_3$ nanocubes is not significantly blueshifted with respect to bulk-like crystals.

Importantly, it is found that the $CsPbBr_3$ perovskite nanocubes exhibit much higher (~80%) PLQY compared to that of bulk film (<0.1%), as can be clearly seen from the inset photos in figure 5.5 (a). The high PLQY of nanocubes is attributed to their small size, defect-free nature and surface passivation by ligands which promote the raditative recombination of charge carriers [133]. While in the case of bulk-like film, there is a strong tendency of trap-assisted nonraditive recombination due to their large size and long carrier diffusion.

As discussed, the optical properties of bulk $CsPbBr_3$ perovskite material can be altered by reducing their size to nanoscale with the help of ligand molecules. In addition, the emission colour of these perovskite nanocubes is tunable across the entire visible spectrum of light by changing the halide composition while preserving their morphology [130]. Figure 5.6 (a) shows the PL and absorption spectra of colloidal $CsPbX_3$ perovskite nanocubes with different halide compositions. Apparently, the positions of the PL peak and the absorption band edge are closely associated with the respective halide composition. This is mainly attributed to the halide dependent bandgap in these metal halide perovskite materials, which has been reported before and also discussed in chapter 2. Figure 5.6

(b) displays the bonding diagram of PbX_6 cluster, the major contributor to the lead halide perovskite band structures. The VBM is mainly formed from the hybridization of halide p and Pb 6s states while the CBM is domibated by Pb 6p character with a minor contribution from halide contribution. This results in the fact that the VBM can be easily modulated by the halide composition while the CB is relatively insensitive to halide chemistry, making the bandgap of $CsPbX_3$ perovskite follow the tendency of $E_g(Cl) > E_g(Br) > E_g(I)$. Here, all the $CsPbX_3$ nanocube samples show a weak quantum confinement compared to bulk crystals, while the degree of the confinement can be different due to the difference in exciton Bohr radius and carrier effective mass depending on the halide composition [131].

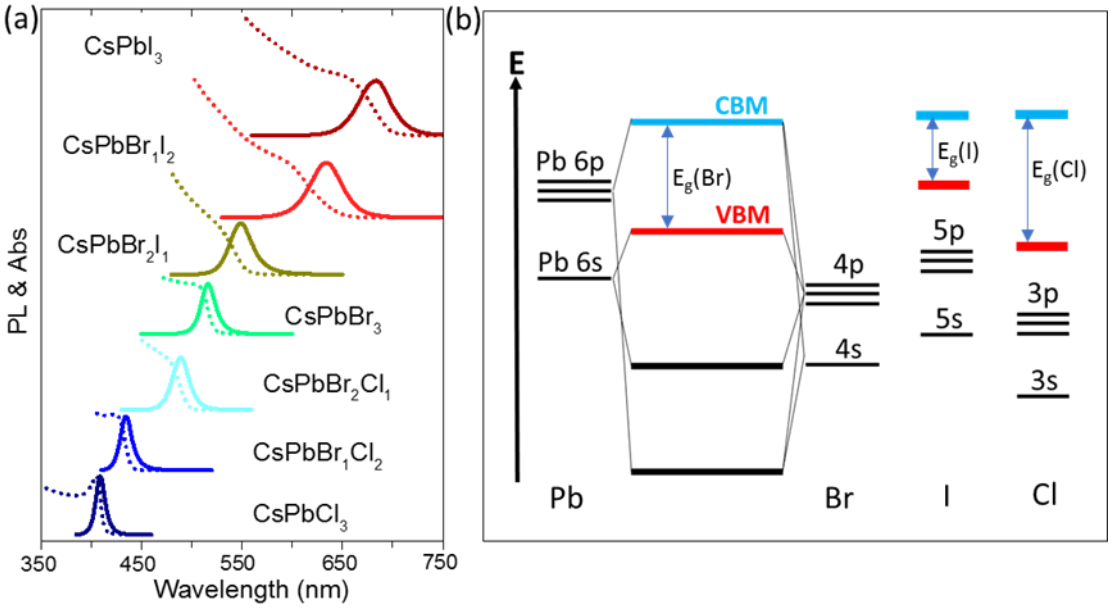

Figure 5.6: (a) PL (solid lines) and absorption spectra (dashed lines) of colloidal $CsPbX_3$ (X=Cl, Br, I or their mixtures) perovskite nanocubes. (b) Schematic illustration of the bandgap change due to different halide composition, based on ref [95].

5.2.2 Increasing quantum confinement by reducing dimensionality

As discussed above, the $CsPbX_3$ nanocubes exhibit a weak quantum confinement, thus the PL is only slightly blueshifted compared to that of the bulk material. Considering the strong quantum confinement observed in 2D $MAPbBr_3$ NPls as discussed earlier, the thickness dependent quantum confinement effects of $CsPbX_3$ perovskite NPls are explored.

First, I start with the study of quantum confinement effect in $CsPbI_3$ perovskite NCs. Figure 5.7 (a) shows the PL and absorption spectra of the colloidal $CsPbI_3$ NCs with tunable dimensionality, which is achieved by changing the Cs to Pb precursor ratio in the ultrasoinocation assisted synthesis approach, as described in the experimental part. It can be obviously seen that there is a significant change in the absorption and PL spectra of the obtained $CsPbI_3$ NCs by decreasing the molar ratio of Cs_2CO_3 and PbI_2 precursors. At the molar ratio of 1:3, there is a single PL peak centered at 685 nm with a FWHM of ~40 nm. The corresponding TEM image shown in figure 5.7 (b) shows the cubic shape of the obtained $CsPbI_3$ NCs with an average size of ~12 nm. Therefore, the peak at 685 nm is attributed to the quasi-3D $CsPbI_3$ nanocubes showing weak quantum confinement as the average size of the nanocubes (~12 nm) is larger than the reported exciton Bohr radius of $CsPbI_3$ peovskites (~6 nm) [130]. With the Cs to Pb precursor ratio decreasing, the dimensionality of the $CsPbI_3$ NCs significantly changes from 3D nanocubes to 2D NPls with different thicknesses as can be seen from the TEM images (figure 5.7 (c)-(e)).

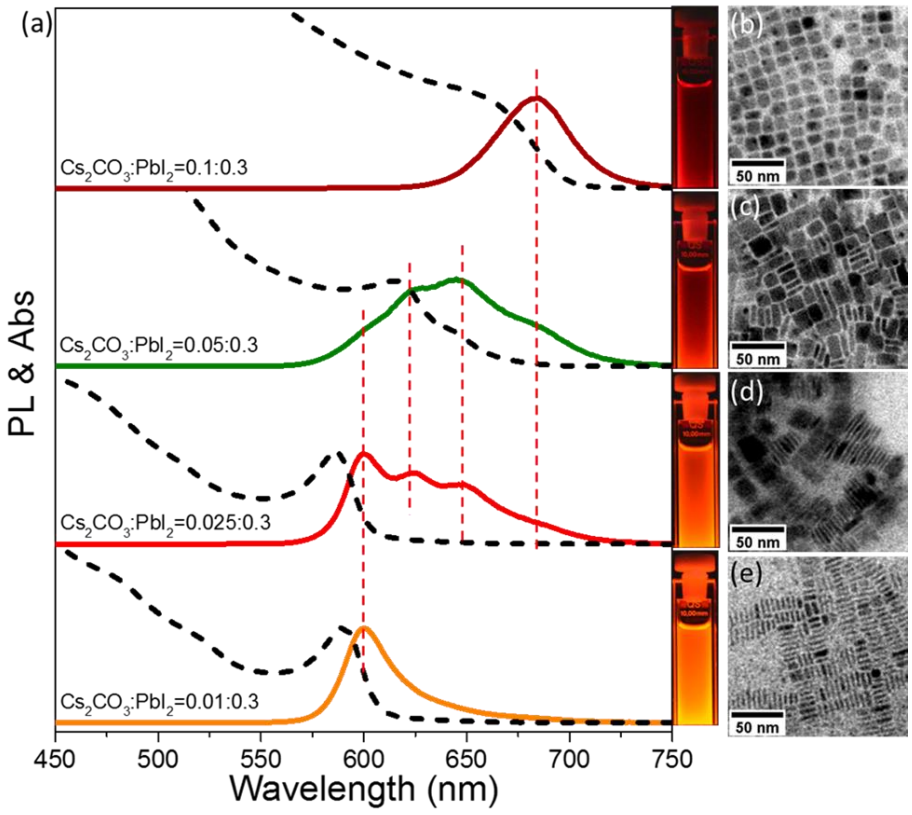

Figure 5.7: (a) PL (solid lines) and absorption spectra (dashed lines) of colloidal $CsPbI_3$ perovskite NCs obtained with different molar ratios of Cs to Pb precursors in the ultrasonication assisted synthesis approach.

Photos of the corresponding sample under UV light are also included. (b-e) TEM images of the samples showing a transition from nanocubes to NPls with decrease of Cs to Pb precursor ratio.

Therefore, the multiple peaks of the PL spectra obtained for NPls can be assigned to the $CsPbI_3$ NPls of different thicknesses. As the dimensionality changes from 3D to 2D, new PL peaks arise at shorter wavelength due to stronger quantum confinement, similar to the case of $MAPbBr_3$ NPls. The PL spectra of NPl samples show that the NPls with different thicknesses always coexist but the amount of thinner NPls increases with decreasing precursor ratio. Therefore, the relative intensity of the PL peak with shorter wavelength increases while the positions of the peaks remain almost unchanged. The resultant luminescence color of the NC colloids changes from dark red to bright orange. There is also a remarkable change in the absorption spectra in accompany with the corresponding PL change. The colloidal $CsPbI_3$ nanocubes exhibit a smooth absorption spectrum with an absorption onset at 670 nm, but without distinguishable excitonic absorption peak, being a result of the small exciton binding energy (~20 meV) in these NCs. As the dimentioanlity changes from nanocubic to NPls, excitonic peaks becomes more prominent due to an increased exciton binding energy in the 2D NPls [7, 99, 134, 135]. In the extreme case of lowest Cs_2CO_3 to PbI_2 ratio, a narrow PL peaked at 600 nm is observed and the FWHM is around ~25 nm. The TEM image in figure 5.7 (e) shows that only thin NPls are present with an almost homogenous thickness of ~2nm. This should correspond to the $CsPbI_3$ NPl with three perovskite monolayers (3ML) considering the thickness of each monolayer is ~0.63 nm for $CsPbI_3$ perovskite [131]. Notably, the linewidth of PL centered at 600 is much narrower than that of the 685 nm one, further suggesting that the PL is coming from the NPl with 2D nature [44]. Likewise, the PL peaks at 623 nm, 638 nm and 647 nm can be assigned to the 4, 5, 6ML $CsPbI_3$ NPls, respectively.

As described for $MAPbBr_3$ NPls system, due to the stacking nature of NPls, the Kronig-Penny model is applied for the quantitative determination of the thickness-dependent quantum confinement in these $CsPbI_3$ NPls. Two quantum confinement regimes are to be considered, the strong confinement regime when the thickness is smaller than the exciton Bohr radius and the weak confinement regime otherwise. The exciton Bohr radius of $CsPbI_3$ perovskite is determined according to the equation 2.25. Taking the dielectric constant of $\varepsilon = 6.32\varepsilon_0$ into account [131], the exciton Bohr radius is calculated to be 5.6 nm. Knowing that the thickness of each monolayer is ~0.63 nm in $CsPbI_3$ NCs, the NPls below 9 ML are considered to be in the strong confinement regime. Thereafter, the quantum confinement in $CsPbI_3$ NPls can be modeled by using related

parameters taken from literatures [99, 136], and the obtained theoretical results match well with the experimental data as shown in figure 5.8 (a).

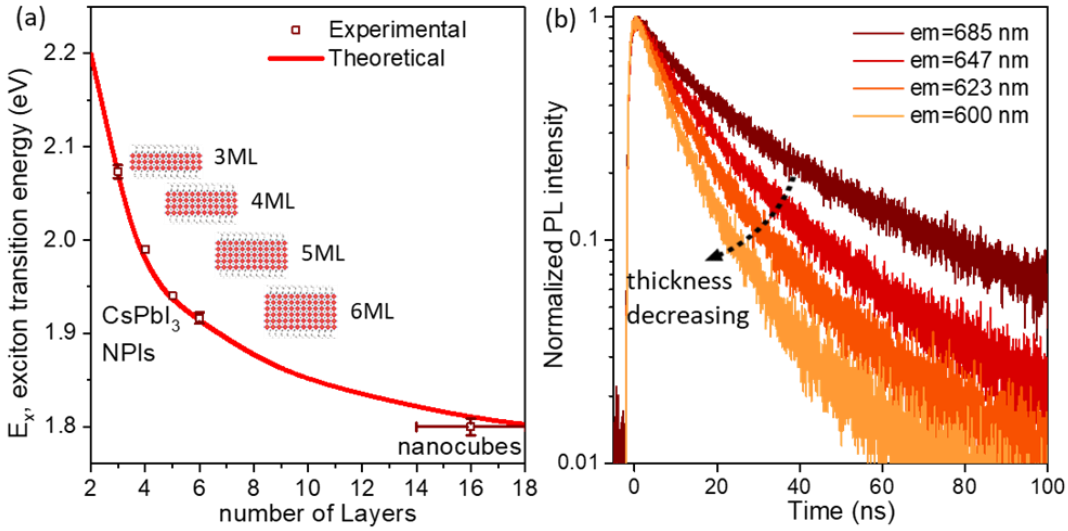

Figure 5.8: (a) Theoretically determined exciton transition energy (solid line) using Kronig-Penny model and the experimental values (open squares) obtained from the PL spectra. The exciton transition energy increases with the number of monolayers (ML) decreasing in $CsPbI_3$ NPls due to quantum confinement. The insets schematically shows the corresponding NPl thicknesses. (b) PL dynamics of $CsPbI_3$ NCs with different thicknesses. The arrow shows the decreasing tendency of PL lifetime with the decrease of NPl thickness.

In addition, time-resolved PL measurements are carried out on the colloidal $CsPbI_3$ NPls to examine the change of charge carrier dynamics with the dimensionality. Figure 5.8 (b) shows the PL decay dynamics of colloidal $CsPbI_3$ NPls with different thicknesses by looking at respective PL peak positions of NPls. A sample containing a mixture of $CsPbI_3$ perovskite NCs with different dimensionalities is used (prepared by using 0.25:0.3 precursor ratio as shown in figure 5.7 (a)). To reduce the interaction between individual NPls and the possible energy transfer, the sample is first sufficiently diluted with hexane. It can be seen that with the decrease of NPl thickness, the PL decays faster. The the PL lifetime (τ_{PL}, determined from the time delay when the PL intensity decays to $1/e$ of the initial value) significantly decreases from 25 ns to 10 ns. Assuming that the PL decay in colloidal $CsPbI_3$ perovskite NCs involves a monoexponential excitonic radiative decay together with other nonradiative processes, the radiative and nonradiative decay rates can be determined by combining PLQY and PL lifetime.

The PL decay rate (k_{PL}) is given by

$$k_{PL} = \frac{1}{\tau_{PL}} = k_r + k_{nr}, \tag{5.12}$$

with k_r and k_{nr} representing the radiative and nonradiative decay rate, respectively.

The PLQY, Φ_{PL}, is related to the decay rates by

$$\Phi_{PL} = \frac{k_r}{k_{PL}} = \frac{k_r}{k_r + k_{nr}}, \tag{5.13}$$

Thus, the radiative and nonradiative decay rate can be derived as

$$k_r = \frac{\Phi_{PL}}{\tau_{PL}},\ k_{nr} = \frac{1-\Phi_{PL}}{\tau_{PL}}. \tag{5.14}$$

The PLQYs of the colloidal $CsPbI_3$ perovskite nanocubes (PL ~685 nm) and 3ML NPls (PL ~600 nm) are experimentally measured to be 92% and 70%, respectively. Therefore, according to equation 5.14, the k_r is calculated to be 0.07 ns^{-1} for NPls and 0.037 ns^{-1} for nanocubes, respectively, while the k_{nr} is 0.03 ns^{-1} for NPls and 0.003 ns^{-1} for nanocubes. It can be seen that both radiative and nonradiative decay rates increase when the dimesionality decreases from 3D to 2D. The larger k_r can be attributed to an increased exciton binding energy in the 2D NPls [44], while the larger k_{nr} is likely due to a high amount of surface traps in the 2D NPl and a resultant nonradiative recombination .

In fact, the change of carrier type could also contribute to the difference in the PL decay dynamics in these colloidal $CsPbI_3$ perovskite NCs. As discussed earlier, the exciton binding energies of the 2D perovskite NPls are much larger than that of the corresponding 3D bulk materials, so that the excitons are less likely to be dissociated in the 2D NPls and this is also reflected in the absorption spectra with a stronger excitonic absorption peak for NPls, as shown figure 5.7 (a). Therefore, the carriers existing in the 2D $CsPbI_3$ perovskite NPls are dominated by the excitons instead of free electrons and holes. In contrast, in the quasi-3D $CsPbI_3$ perovskite nanocubes, the charge carriers are expected to be populated mainly by the free electrons and holes rather than excitons due to

weaker confinement and smaller exciton binding energy. Hence, the electrons and holes are two separate charge carrier species, so their radiative recombination will lead to a PL with bimolecular decay. [137-139]. Consequently, the PL decay curve of perovskite nanocubes is better fitted using a bimolecular decay mode whereas the PL decay of NPls can be fitted monoexponentially.

Similar to the $CsPbI_3$ NCs, the dimensionality of $CsPbBr_3$ NCs is contrtolled from 3D to 2D and their optical properties are studied. As shown in figure 5.9 (a), the colloidal $CsPbBr_3$ nanocubes show bright cyan-green emission with a PL peak at ~515 nm due to weak quantum confinement as discussed before. In contrast, the colloidal NPls containing a mixture of NPl with different thicknesses exhibit sharp excitonic absorption peaks and significantly blueshifted PL due to strong quantum confinement. The PL peaks at shorter wavelengths, i.e., 460 nm, 478 nm and 487 nm correspond to the exciton transition energies of 2.7 eV, 2.6 eV and 2.55 eV, respectively. According to Kronig-Penny model calculation, these peaks are attributed to $CsPbBr_3$ NPls with 3ML, 4ML and 5ML, respectively as displayed in figure 5.9 (b). However, similar to the case of $MAPbBr_3$ NPls, the obtained colloidal samples always contain a mixture of NPls with different thicknesses and it is difficult to separate them into individual homogeneous thicknesses. This leads to the difficulties of study the optical properries of NPls with individual thickness.

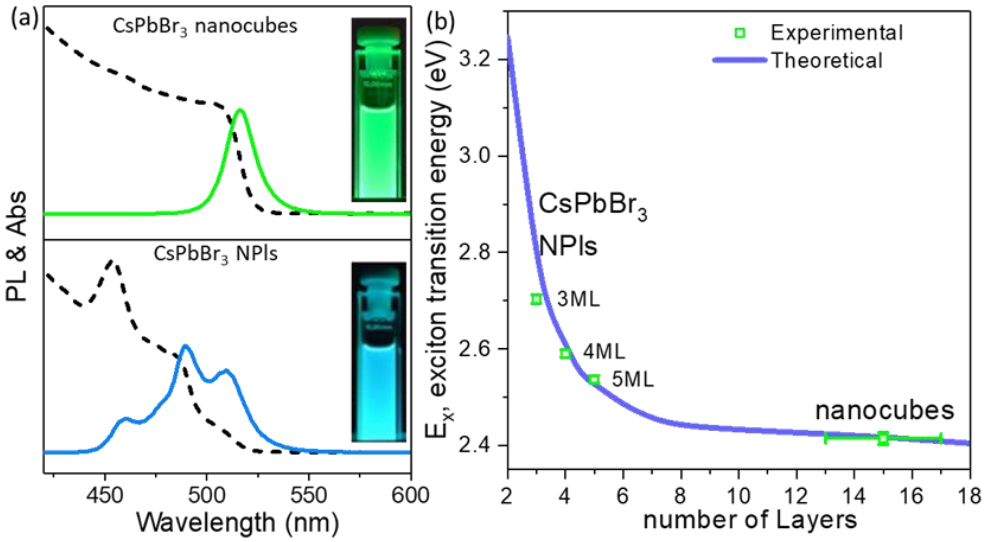

Figure 5.9: (a) PL (solid lines) and absorption (dashed lines) spectra of colloidal $CsPbBr_3$ nanocubes (top) and NPls (bottom) obtained with different molar ratios of Cs to Pb using the ultrasonication approach. Insets are the photos of the corresponding samples under UV light illumination. (b) Experimentally (open squares)

and theoretically (solid line) determined exciton transition energies of $CsPbBr_3$ NPls as a function of NPl thickness.

5.3 Thickness control and surface defects repair of $CsPbBr_3$ perovskite nanoplatelets

In the previous sections, it is shown that in both organic-inorganic and all-inorganic perovskite NCs, the optical properties are tunable through quantum confinement effects by changing their dimensionality from 3D nanocubes to 2D NPls. The PL peak position can be quantitatively correlated with their thickness by means of theoretical calculations. It is also shown that the 2D NPls exhibit faster PL decay dynamics compared to quasi-3D nanocubes. However, one main problem with the NPls is the difficulty to have a precise control over their thickness. The previous synthesis normally leads to the formation of a mixtrure of NPls with different thicknesses, which makes it difficult to individually study their optical properties. In the following, the optical properties of $CsPbBr_3$ perovskite NPls with precisely controlled thicknesses are presented by the preparation with adjustable number of perovskite monolayers at room temperature. This enables a deeper understanding of their thickness-dependent optical properties. In addition, it is shown that the PL of NPls can be significantly enhanced by post-synthetic surface trap repair.

5.3.1 Controlling thickness and optical properties of nanoplatelets

Motivated by the fact that the dimensionality of the $CsPbBr_3$ NCs can be readily changed by varying the ratio between Cs_2CO_3 and $PbBr_2$ precursors in the reaction medium. A simple room temperature synthesis is developd to prepare colloidal $CsPbBr_3$ perovskite NPls with monolayer-level thickness control. The details of the synthesis are provided in the experimental part.

As shown in figure 5.10 (a), the emission color of the colloidal $CsPbBr_3$ perovskite NCs is tunable from violet-blue via sky blue to green by increasing the ratio of Cs to Pb precursors. This, according to this previous discussion, suggests that the thickness of the $CsPbBr_3$ NPls is increasing (figure 5.10 (b)) thus that the quantum confinement effect is weakening. Notably, in contrast to the previous case, these colloidal $CsPbBr_3$ NPls dispersions exhibit narrow PL linewidth as depicted in figure 5.10 (c). The narrow FWHMs of the PL of the colloidal NPls, ranging from 11 nm to 25 nm, indicate a homogeneous thickness distribution in each NPl dispersion due to the fact

that the PL peak position is dependent on the thickness of the NPls. Based on the quantitative analysis of the quantum confinement in perovskite NPls as discussed earlier, the PL peaks at 435 nm, 460 nm, 477 nm, 487 nm and 496 nm can be attributed to the $CsPbBr_3$ NPls with 2ML, 3ML, 4ML, 5ML and 6ML, respectively. As shown before, the quasi 3D $CsPbBr_3$ colloidal perovskite NCs exhibits a PL peak at 515 nm due to only weak quantum confinement [130]. The morphology and dimensionality of the colloidal NPls are further confirmed by the TEM images as shown in figure 5.10 (d)-(f), which display that all the NPl samples have a nearly uniform thickness. The measured thicknesses for 2ML, 3ML and 5ML NPl are ~1.5 nm, ~2 nm and ~3 nm, respectively, matching well with the theoretical predictions of the PL peaks for respective thicknesses.

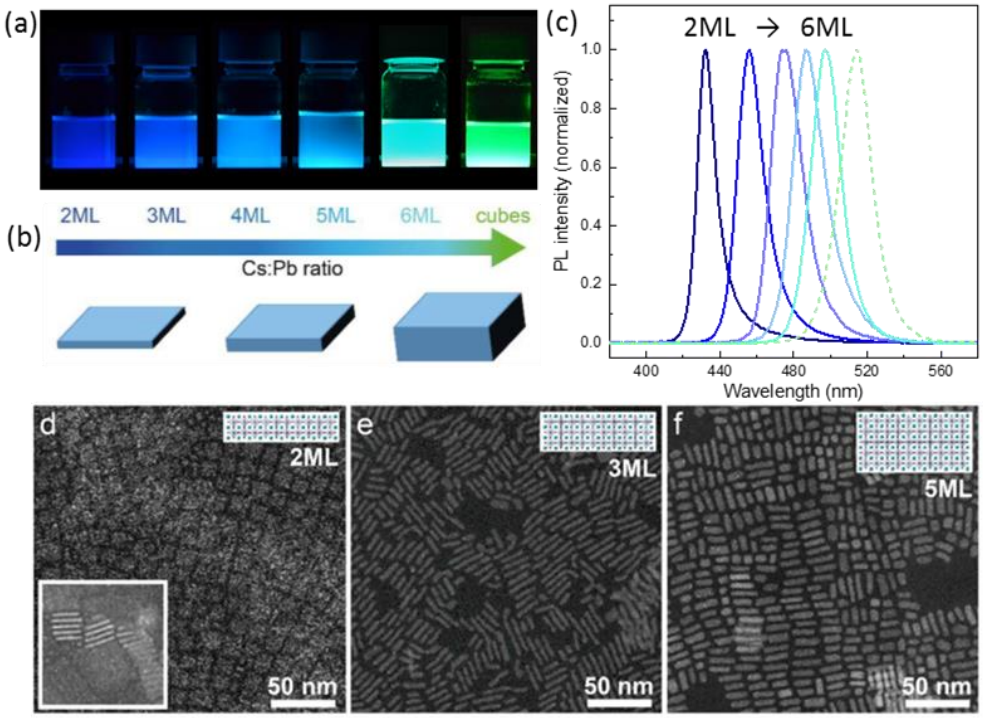

Figure 5.10: (a) Photos of colloidal $CsPbBr_3$ NPls with different thicknesses under UV light. (b) Shematic illustration of the change in NPl thickness. (c) PL spectra of colloidal NPls with thickness controlled from 2ML to 6ML (solid lines), the PL of the quasi 3D $CsPbBr_3$ NCs is also included for comparison (dashed line). (d-f) STEM images of NPls with different thicknesses (2, 3 and 5MLs). The insets schematically show the perovskite NPls with corresponding number of layers.

The success in obtaining nearly-monodisperse $CsPbBr_3$ perovskite NPls of precise thickness enables a further investigation of the thickness-dependent optical properties. Figure 5.11 (a) presents the optical absorption spectra of colloidal $CsPbBr_3$ NPls with different thicknesses. It can

be seen that all 2D NPls exhibit strong excitonic absorption peaks at the lower energy part of the continuum. The position of excitonic peak gradually redshifts with the increase of NPl thickness, and it is consistent with the PL peak shifting presented in figure 5.10 (c) which is attributed to a weakened quantum confinement in thicker NPls. In addition to the redshift of excitonic absorption peak, a change in the shape of the absorption spectrum can also be observed when the NPl thickness is changing. With increasing the NPl thickness, the excitonic feature becomes less prominent and no obvious excitonic peak can be identified in quasi-3D NCs. Moreover, the absorption continuum, which is related to the DOS of electrons in semiconductor materials as introduced in chapter 2, becomes steeper with the increase of NPl thickness. This implies the change of the dimensionality of these NCs as the DOS are distinct in 2D and 3D semiconductors as described earlier.

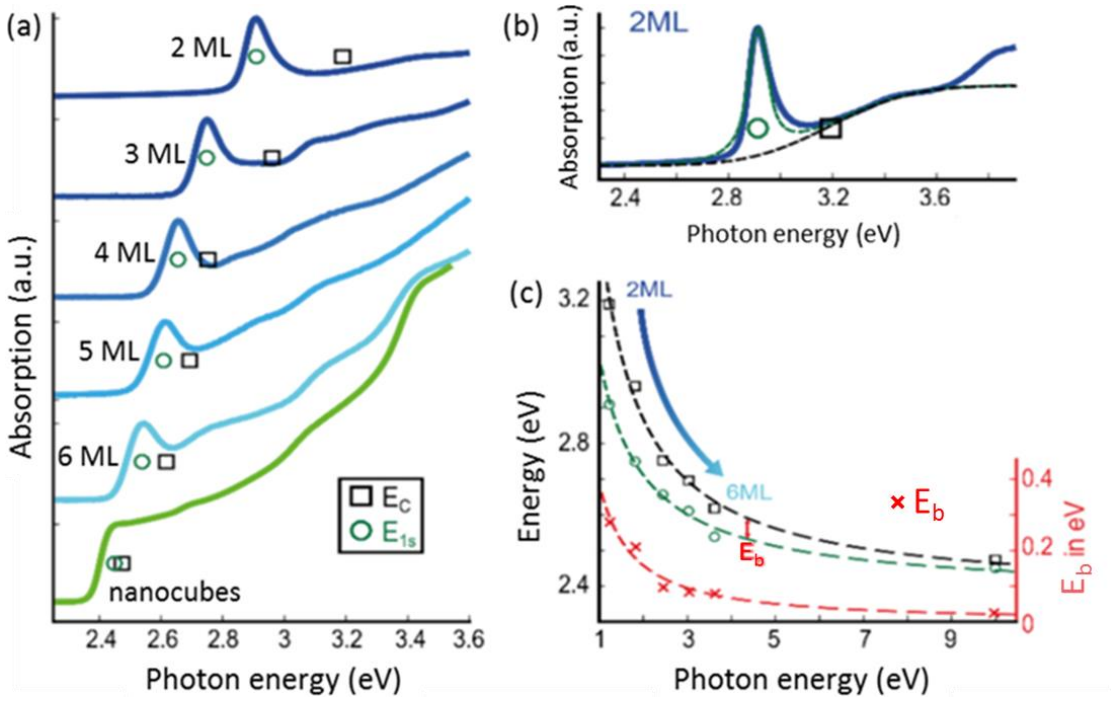

Figure 5.11: (a) Linear optical absorption spectra of colloidal $CsPbBr_3$ perovskite NPls with different thicknesses and the spectrum of the nanocube is shown for comparison. The continuum energy level (E_C) and exciton energy level (E_{1s}) of each sample are marked by black squares and green circles, respectively. (b) A representative (2ML) modeling of absorption spectrum for the determination of excitonic (green) and continuum (black) transitions. (c) The E_C, E_{1s} and exciton binding energy (E_b) as a function of NPl thickness. The E_C and E_{1s} are directly obtained from modeling of the absorption spectra and E_B is calculated according to $E_b = E_C - E_{1s}$.

The optical absorption spectra can be theoretically modeled according to the Elliott's formula to distinguish the excitonic absorption and the continuum band onset. Here, by using a reported method described in the introduction chapter [140], the continuum absorption onset energy (E_C) as well as the energetic position of the dominant 1s excitonic transition (E_{1s}) in each NC sample can be determined. As an example, the modeling on the absorption spectrum of the 2ML sample is shown in figure 5.11 (b), and the assigned positions of E_C and E_{1s} are marked with black squares and green circles, respectively. Using a similar method, the positions of E_C and E_{1s} of all samples are determined and labeled (black squares and green circles, respectively) in the corresponding absorption spectrum as shown in figure 5.11 (a). The obtained values are plotted as a function of the NPl thickness and presented in figure 5.11 (c). It can be clearly seen that both E_C and E_{1s} are increasing with the increase of NPl thickness. The differences between the E_C and E_{1s} is exactly the exciton binding energy E_b, described by

$$E_b = E_C - E_{1s}. \tag{5.15}$$

It can be clearly seen that the exciton binding energy E_b gradually increases with the decrease of NPl thickness, reaching a value of 280 meV for the thinnest (2ML) $CsPbBr_3$ perovskite NPls. This is much larger than the E_b of quasi 3D NC which is ~40 meV [130, 131]. As discussed earlier, the large exciton binding energy in these 2D NPls can be attributed to a decreased dielectric screening of the Coulumb interaction between the electron and hole.

5.3.2 Enhancing photoluminescence of nanoplatelets by surface trap repair

As discussed earlier, the thickness of $CsPbBr_3$ perovskite NPls can be precisely controlled to achieve narrow and tunable emission. However, their PLQY decreases with decreasing their thickness due to an increased density of surface defects in thinner NPls. For example, the 2ML and 3ML exhibit PLQYs of ~7 % and ~9 %, respectively, while the nanocubes exhibit over 80 % PLQY. Such low PLQYs observed in 2D colloidal semiconductor NCs are commonly attributed to the high surface-to-volume ratio of these 2D nanostructures which causes large amount of surface traps [83]. In particular, the mobility of halide ions in perovskite is found to be high [141-143]. As a result, they can easily escape from the surface of the NPl thus leading to the formation of defects on the NPl surface. These surface defects likely increase the probability of trap-assisted nonradiative carrier recombination in these NPls, thus resulting in a low PLQY. In this section, it

is shown that an effective repair of these surface defects can significantly enhance the PLQY of the $CsPbBr_3$ perovskite NPls.

The surface of $CsPbBr_3$ NPls are generally composed of lead hexabromide octahedral and/or Cs-oleate. It is likely that the lack of some of these species on the surface can lead to the formation of defects. It is found that such surface defects can be repaired through the addition of $PbBr_2$-ligand (oleic acid and oleylamine) solution into the pre-synthesized colloidal $CsPbBr_3$ perovskite NPls.

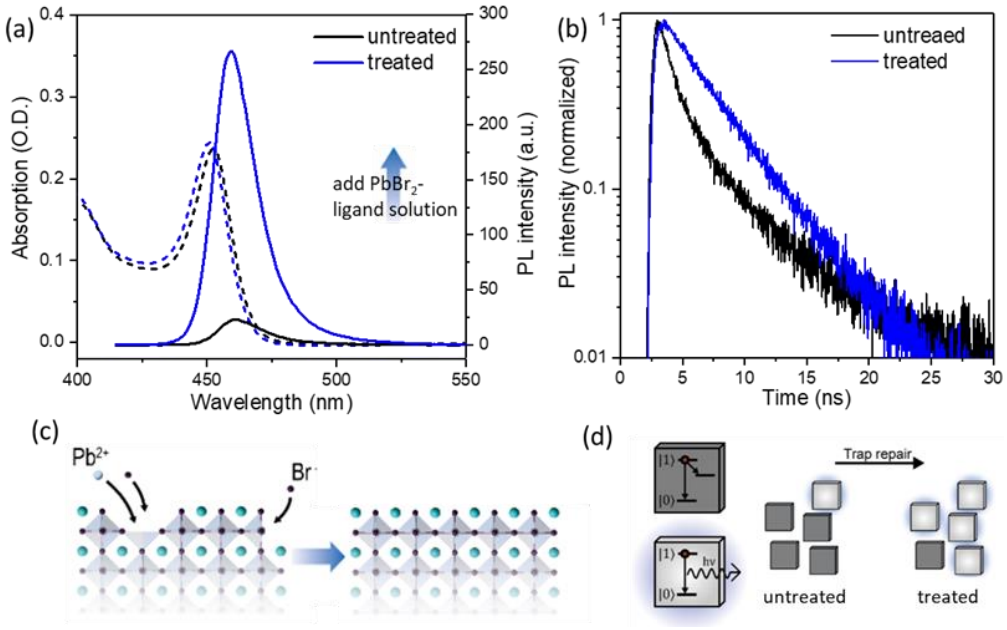

Figure 5.12: (a) PL (solid lines) and absorption (dashed lines) spectra of untreated (black) and treated (blue) colloidal 3ML $CsPbBr_3$ perovskite NPls. (b) PL decay curves of untreated (black) and treated (blue) colloidal NPls. (c) Schemetic illustration of the repair of surface defects in a $CsPbBr_3$ perovskite NPl. (d) Scheme showing that the non-emissive perovskite NPls become emissive after surface trap repair.

Figure 5.12 (a) shows the PL and absorption spectra of the initial and and $PbBr_2$ treated 3ML NPl colloidal dispersion, and it can be clearly seen that the PL intensity is significantly enhanced by the addition of $PbBr_2$-ligand solution to the NPl dispersion, while the absorption spectra remains nearly unchanged. The PLQY of the treated sample is measured to be ~60%, which is almost 7 times higher compared to that of the initial colloidal dispersion. These results clearly indicate that the $PbBr_2$ treatment enhances the PL efficiency of the colloidal NPls without affecting their thickness or uniformity. Moreover, as shown by the time-resolved PL spectra in figure 5.12 (b), the treated NPl colloidal sample shows a dramatic difference in its PL decay compared with the

untreated one. The untreated sample exhibits a nonexponentional PL decay, indicating that several decay channels are involved in the carrier recombination. On the contrary, the PL of the treated sample exhibits a nearly monoexponential decay. This, in combination with the high PLQY, suggests an efficient radiative excitonic recombination in the treated NPl.

The significant PL enhancement after treatment is attributed to the effect of surface trap repair in $CsPbBr_3$ perovskite NPls. As schematically shown in figure 5.12 (c), the addition of $PbBr_2$ leads to the filling of Pb and Br defects in the initial $CsPbBr_3$ NPls. The ensemble effect of surface trap repair on the PLQY and PL decay dynamics of $CsPbBr_3$ perovskite NPls is schematically illustrated in figure 5.12 (d). The surface defects on the untreated NPls result in trap states below the conduction band. As a result, the excited charge carriers can recombine nonradiatively through defect-induced trap states and make the NPl weekly emissive or nonemissive (dark platelets in the scheme), while the charge carries will recombine radiatively in defect free NPls (bright plates in the scheme). Therefore, the $CsPbBr_3$ perovskite NPls exist in two ensembles, highly emissive and nonemissive as shown in the scheme in figure 5.12 (d). In the untreated colloidal NPls, the fraction of the non-emissive NPls is large. As a consequence, the NPl dispersion shows a low overall PLQY and the PL decay is nonexponential due to non-emissive NPls. In contrast, for the treated NPls, the repair of surface defects renders a larger fraction of the NPls emissive. As a result, the PLQY of the colloidal NPls is significantly increased, and the PL decay becomes dominated by excitonic recombination, thus exhibiting a nearly-monoexponential decay.

In fact, the $PbBr_2$ treatment induced PL enhancement is effective for all the NPls starting from 2 ML to 6 ML samples while the degree of enhancement is strongly dependent on their thickness, with the PLQY increasing by a much larger factor for the thinner NPls. This further supports that the enhancement of PLQY is due to a repair of the surface traps as the surface defect density depends on the thickness of the NPls. The surface-to-volume ratios of NPls with different thicknesses are calculated by assuming that each individual NPl has a similar average lateral size of 30*30 nm (estimated from TEM images shown in figure 5.10) while a varied thickness depending on the number of monolayers. Knowing that the thickness of a $CsPbBr_3$ perovskite monolayer is ~0.6 nm, the surface-to-volume ratio (S_V) of the NPls can be related to the number of monolayers (n) by

$$S_V = \frac{2\times 30^2 + 4\times 30\times (0.6n)}{30^2\times (0.6n)} = \frac{2}{15} + \frac{10}{3n}. \qquad (5.16)$$

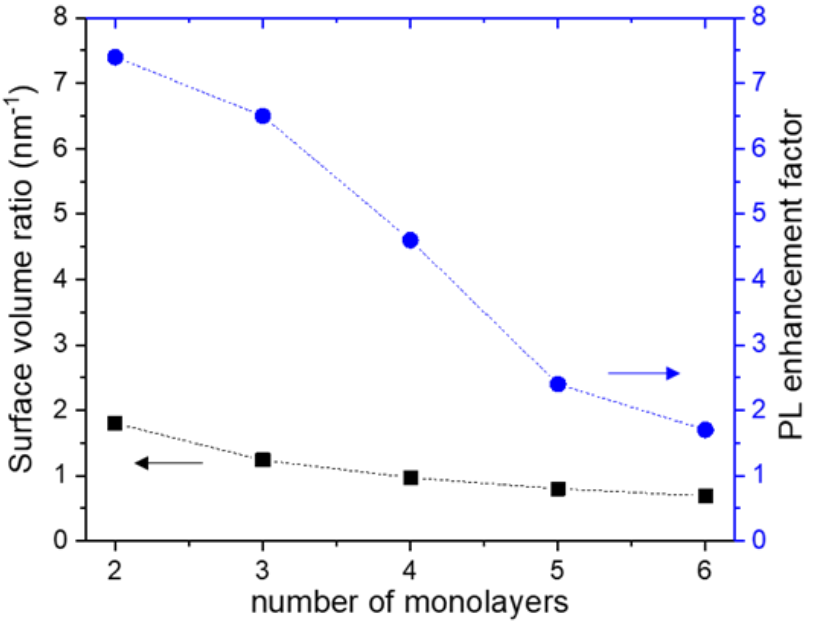

Figure 5.13: Plots of surface-to-volume ratio (black squares) and PL enhancement factor (blue circles) vesus the number of monolayers of $CsPbBr_3$ perovskite NPls. The dashed lines are guides to the eyes.

S_V and PL enhancement factor after treatment are plotted as a function of n as shown in figure 5.13. The plots clearly show that the surface-to-volume ratio and the PL enhancement factor (determined from the PLQYs of the treated and untreated NPl colloids) increases with NPl thickness decreasing. For the 2 ML perovskite NPls, the PLQY increases by almost 8 times after $PbBr_2$ treatment, reaching nearly 50%. The drastic enhancement suggests the efficient repair of the surface defects which abundantly exist in the untreated thin NPls. While for the 6 ML sample, the enhancement is only small due to a relatively low defect density in the untreated thick NPls. In fact, the initial PLQY of 6 ML sample is relatively high due to the low S_V and and low surface defect density, therefore the enhancement factor is relatively small. The results above clearly suggest that the surface trap repair is an effective way to enhance the PLQY of the 2D $CsPbBr_3$ NPls. The post-synthetic surface trap repair is more effective for thinner NPls with higher defect density, thus leading to a larger enhancement factor.

5.4 Summary

This chapter focuses on the investigation of dimensionality dependent optical properties of both organic-inorganic hybrid and all-inorganic perovskite NCs. It is shown that the dimensionality of hybrid perovskite ($MAPbBr_3$) can be decreased from 3D cubes to 2D NPls by increasing the ratio of long chain to short chain alkyl ammonium cations. As the dimensionality changes from 3D to 2D, the absorption onset and PL peak are significantly blueshifted due to strong quantum confinement. In addition, the quantum size effects of $MAPbBr_3$ perovskite NPls are studied by theoretical models and correlated the corresponding PL with the NPls thickness. To enhance the stability of NCs, the organic cation MA is replaced with Cs to obtain all-inorganic $CsPbX_3$ (X=Cl, Br, I) NCs with optical properties tunable by dimensionality and halide composition. It is found that the $CsPbX_3$ nanocubes exhibit quasi-3D optical properties showing only weak quantum confinement with respect to the bulk crystals, whereas the NPls show strong quantum confinement. The PL peak positions of the NPls are calculated by theoretical model and they are in good agreement with experimental results. Time-resolved PL measurements reveals that the NPls exhibit faster PL decay compared to nanocubes. Furthermore, it is shown that the thickness of $CsPbBr_3$ NPls can be controlled in the monolayer level from 2 to 6 ML and they exhibit narrow emission and sharp excitonic absorption peaks. By modeling the absorption spectra of the colloidal NPls, it is found that the exciton binding increases with decreasing the thickness of NPls. The exciton binding energy of 2 ML $CsPbBr_3$ NPls is found to be ~280 meV, while it is only ~40 meV for the quasi-3D nanocubes. The as-obtained 2D NPls generally exhibit low PLQYs, however, it is discovered that the PLQYs of NPls can be remarkably enhanced by postsynthetic surface trap repair. These results clearly show that highly luminescent and narrow emissive perovskite NPls with tunable optical properties can be achieved by perfect control over their dimensnality.

6. From perovskite nanocubes to nanowires and supercrystals: different optical properties

In the previous chapter, it is shown that the optical properties of metal halide perovskite NCs can be effectively tuned by decreasing the dimensionality from 3D to 2D. This chapter will focus on the control of the optical properties of $CsPbBr_3$ perovskite NCs by changing their shape and making NC assemblies. First it is shown that $CsPbBr_3$ NWs can be formed through an oriented attachment of the nanocubes. The NWs show redshifted PL compared with the nanocubes due to an elongated shape and charge carrier delocalization. Due to an anisotropic shape, the NWs exhibit a polarization anisotropy in their PL. Meanwhile, compared with the corresponding nanocubes, the NWs have much lower PLQY due to a dominant nonradiative recombination. This is attributed to the carrier diffusion in the NWs and resultant trap-assisted nonradiative process, which is further confirmed by the significant PL enhancement of the NWs at low temperature. Furthermore, the $CsPbBr_3$ perovskite nanocubes can self-assemble into supercrystals exhibiting different optical properties compared to the isolated nanocubes. The PL and PLE spectra of the supercrystals show obvious redshift in comparison with the isolated nanocubes, suggesting an electronic coupling between the neighboring nanocubes. In comparison with the NWs showing low PLQY, the supercrystals preserve the high PLQY of the nanocube subunits.

6.1 Oriented attachment of $CsPbBr_3$ nanocubes to form nanowires

This section studies the shape tranformation from $CsPbBr_3$ nanocubes to NWs using optical spectroscopy methods including PL and absorption spectroscopy as wll as morphological measurements. In addition, the changes in the optical properties from nanocube to NWs are discussed.

6.1.1 Change in photoluminescence by transforming nanocubes to nanowires

As discussed in previous chapter, $CsPbBr_3$ perovskite nanocubes with narrow PL emission can be obtained by ultrasonication method. Interestingly, it is discovered that through a similar approach but a prolonged sonication time, $CsPbBr_3$ perovskite NWs can be produced [144]. In the following, the optical probing of this shape transformation in combination with morphological characterization will be shown.

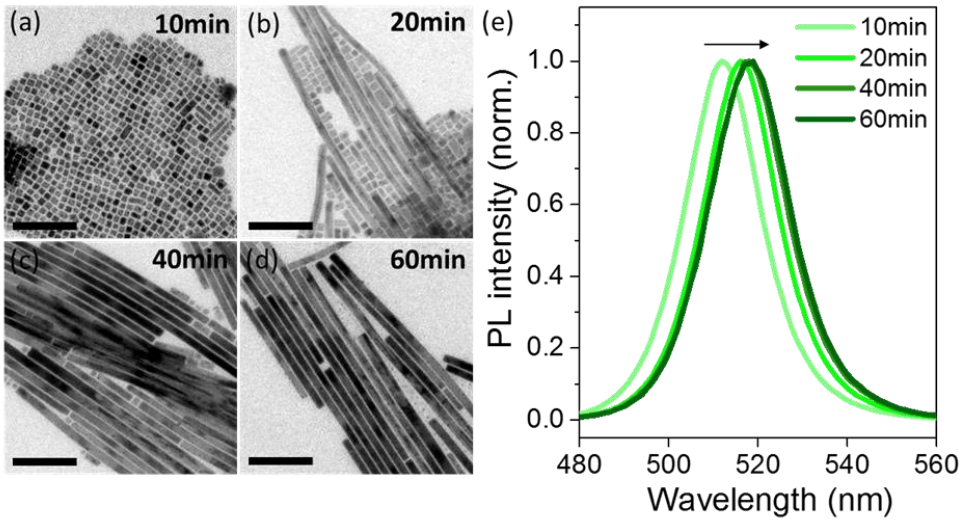

Figure 6.1: (a)-(d) TEM images of $CsPbBr_3$ NCs obtained at different reaction time (10 min, 20 min, 40 min and 60min as labeled in the corresponding images. Scale bar: 100 nm). The shape evolution from nanocubes to NWs can be clearly seen. (e) Normalized PL spectra of the NC colloids obtained at different reaction time, corresponding to those shown in (a)-(d), the arrow shows the redshift in PL peak position with increasing reaction time.

TEM images of colloidal $CsPbBr_3$ NCs obtained at different sonication time are shown in figure 6.1 (a)-(d), a significant change in the shape of the NCs can be clearly observed. After 10 min of

sonication, most of the NCs show a cubic shape with a homogeneous edge length of 10-15 nm and this is consistent with the formation of nanocubes as discussed in the previous chapter [130]. After 20 min, as shown in figure 6.1 (b), the amount of the nanocubes decreases and NWs begin to appear. The NWs have a lateral size (~12 nm) similar to the nanocubes whereas their length ranges from 500 nm to several micrometers. As the sonication time further increases, the ratio of NWs over nanocubes increased drastically, leaving behind the NWs with increased length as displayed in figure 6.1 (c) and (d). Associated with the shape changing, the corresponding PL spectra also show a progressive redshift with reaction time as depicted in figure 6.1 (e). At 10 min, there is a narrow PL emission centered at 514 nm with a FWHM of ~23 nm, matching well with that of $CsPbBr_3$ nanocubes that exhibit weak confinement as discussed before. With increasing reaction time, the PL peak position gradually redshifts to 519 nm due to an elongation of the NCs and consequent charge carrier delocalization in the NWs.

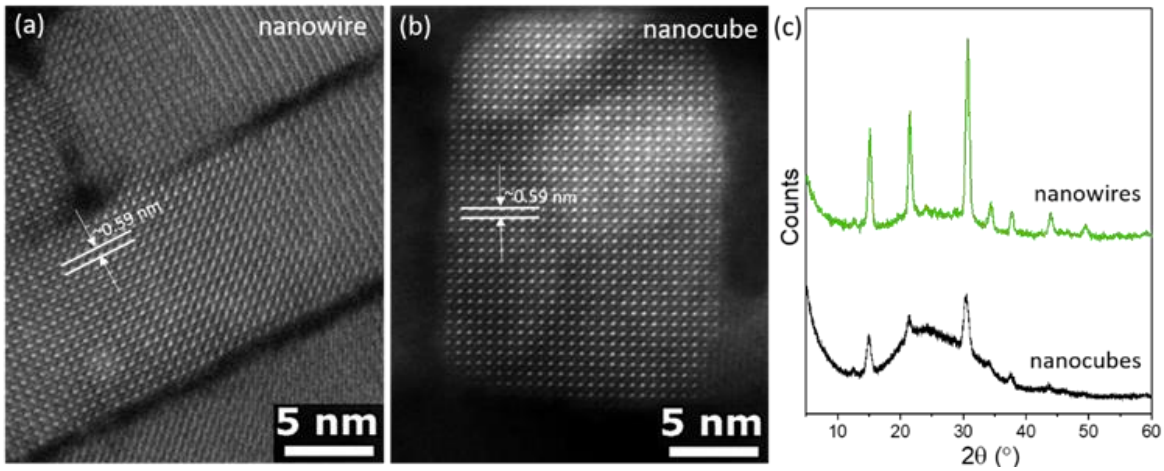

Figure 6.2: HRTEM images of (a) $CsPbBr_3$ NWs and (b) a single nanocube with lattice contant labeled. (c) XRD patterns of $CsPbBr_3$ NWs and nanocubes.

In order to examine whether there is a change in the crystal structure that might also contribute to the PL shift of the NCs, the crystal structure of $CsPbBr_3$ perovskite NWs is also compared with that of the $CsPbBr_3$ nanocubes by HRTEM and XRD measurements. Figure 6.2 shows the acquired HRTEM images of (a) $CsPbBr_3$ perovskite NWs and a nanocube (b). The images clearly show that the $CsPbBr_3$ perovskite nanocubes as well as NWs are single crystalline with high degree of crystallinity. The XRD data of nanocubes and NWs (figues 6.2 (c)) show that they exhibit either cubic or orthorhombic perovskite phase. However, it is difficult to distinguish these two phases

because they are quite similar while only the tilting of [$PbBr_6$] octahedrals makes the difference, which is hard to be identified. In fact, there is still an ongoing debate on the crystal structure of $CsPbBr_3$ perovskite NCs, both cubic and orthorhombic phases have been reported in literature [131, 145]. Nevertheless, the lattice constant of the $CsPbBr_3$ perovskite NWs is determined to be ~0.59 nm, which is in good agreement with the lattice constant of $CsPbBr_3$ nanocubes. Overall, it can be concluded from the HRTEM and XRD measurements that $CsPbBr_3$ perovskite NWs exhibit the same crystal structure as the $CsPbBr_3$ nanocubes. In other words, the $CsPbBr_3$ perovskite crystal structure does not undergo a significant change during the transformation from nanocubes to NWs. Therefore, the crystal structure change can be ruled out from the main reasons responsible for the observed change in the PL spectra, indicating that the change is mainly caused by the shape transformation.

6.1.2 Understanding nanowire formation by absorption spectroscopy

It is shown that the $CsPbBr_3$ perovskite nanocubes can be transformed into NWs and the PL is redshifted. However, the formation mechanism of $CsPbBr_3$ perovskite NWs is still not clear from the morphological and PL characterizations. Here it is shown that linear absorption spectroscopy can be utilized to understand the formation mechanism of $CsPbBr_3$ perovskite NWs.

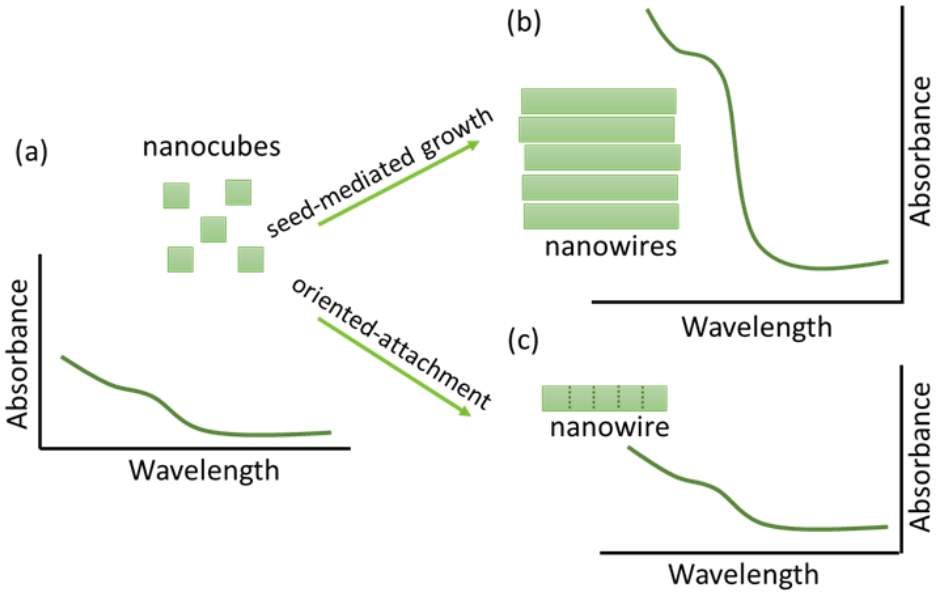

Figure 6.3: Schematic illustration of the comparision of change in absorbance induced by seed-mediated growth and oriented-attachment during NW formation. (a) Absorbance spectrum of initial colloidal

nanocubes. (b) Expected absorbance spectrum of colloidal NWs if they are formed through seed-mediated growth. (c) Expected absorbance spectrum of colloidal NWs if they are formed by oriented-attachement. Insets in (b) and (c) schematically show the amount of NWs formed through corresponding formation routes.

In general, there are two possible distinct mechanisms governing the formation of the NWs, i.e., the seed-mediated growth mechanism and the oriented attachment mechanism [146-148]. Figure 6.3 schematically shows the transformation of $CsPbBr_3$ perovskite nanocubes (a) to NWs through seed-mediated growth (b) and oriented-attachment (c). In the seed-mediated growth, each single perovskite nanocube grows into a NW with a significant increase in the absorbance. In contrast, the oriented-attachment of several nanocubes into a single NW does not increase the absorbance significantly as there is no dramatic change in the total amount of perovskite materials in the colloidal solution.

In order to elucidate the mechanism of NW formation, the absorbance spectrum of the colloid solution is recorderd at different sonication time durig the reaction. The absorbance spectra are normalized at 600 nm to exclude the impact of scattering [144]. As depicted in figure 6.4 (a), the absorbance spectra of $CsPbBr_3$ perovskite NC colloids obtained at different reaction time clearly show that there is no significant increase in the absorbance. After 10 min of sonication, the absorption spectra exhibit an onset at ~510 nm corresponding to $CsPbBr_3$ nanocubes and it is also confirmed by the TEM image as shown in figure 6.1 (a). After 20 min reaction, the absorbance of the colloidal solution is increased and the absorption onset is redshifted. The increase of the absorbance is likely due to the formation of more perovskite NCs in the reaction medium. The slight redshift in the absorption onset is accompanied by a redshift in the PL as shown in figure 6.1 (e). This is attributed to the progressively formed NWs in the reaction medium as evidenced by TEM analysis. As the sonication time increases further, from 20 to 40 min, the absorption onset continues shifting to the longer wavelength and saturates at 520 nm. Notably, despite the redshift in the absorption onset during NWs formation, the absorbance shows no substantial change from 20 min to 60 min. This indicates that the formation of the NWs in the colloid is through an oriented-attachment of the nanocubes instead of a seed-mediated growth, as the latter one will lead to a significant increase in the absorbance of the $CsPbBr_3$ perovskite NC colloid as shown in figure 6.3.

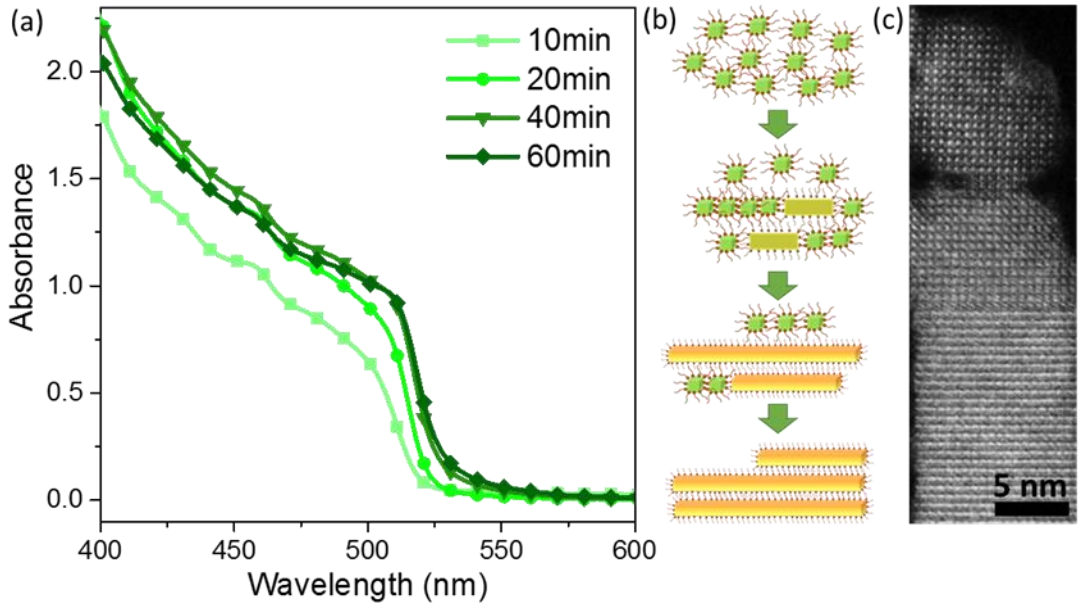

Figure 6.4: (a) Absorbance spectra of $CsPbBr_3$ perovskite NC colloids obtained at different reaction time. (b) Schematic illustration of the oriented-attachment for $CsPbBr_3$ NW formation. (c) HRTEM image of an intermediate stage of the NW formation, showing the oriented-attachment.

Therefore, it can be concluded that the formation of the $CsPbBr_3$ perovskite NWs occurs through an oriented attachment of the nanocubes in the colloidal dispersion as schematically shown in figure 6.4 (b). Further evidence for the oriented-attachment process comes from the HRTEM imaging of an intermediate sample obtained during the sonication (reaction time 20 min) as shown in figure 6.4 (c). From the image, the attachment of a nanocube to the side of an elongated wire-shaped NC can be clearly seen. The width of the obtained NWs and their crystallinity is similar to those of the nanocubes, being indicative that the $CsPbBr_3$ perovskite nanocubes attach to each other in one preferential direction to form NWs with their initial crystal structure and diameter retained.

6.2 Photoluminescence comparison of $CsPbBr_3$ nanowires and nanocubes

As discussed in the previous section, $CsPbBr_3$ perovskite nanocubes are elongated in one direction through oriented-attachment, thus forming NWs with a similar diameter but much larger length compared to nanocubes. The transformation of nanocubes into NWs causes changes in the PL and

absorption spectra, suggesting that the NWs and nanocubes have different optical properties. This section will focus on a comparative study on the PL of $CsPbBr_3$ NWs and nanocubes.

6.2.1 Photoluminescence polarization anisotropy of $CsPbBr_3$ nanowires

In general, 1D semiconductor nanostructures exhibit optical anisotropy and it has been explored in a wide range of materials [149-151]. Likewise, in the current $CsPbBr_3$ perovskite NW system, as the NWs have a much larger size in one dimension than the other two dimensions, they have a highly anisotropic quasi-1D shape, thus an optical anisotropy can be expected. Here the optial anisotropy is explored in the $CsPbBr_3$ perovskite NWs.

In fact, the anisotropic optical properties of semiconductor materials with an anisotropic geometry are of high interest for both fundamental studies and applications. Semiconductor NWs have a quasi-1D shape since the size in one dimension is much larger than the other two dimensions. The quasi-1D nature of semiconductor NWs makes them attractive for electronic transport, sensing, and polarization sensitive applications, as well as fundamental studies [149-153]. In the past decades, semiconductor NWs with various chemical compositions, a range of diameters, and aspect ratios have been prepared through different techniques and their optical anisotropies have been extensively studied. Large polarization anisotropies of excitation, photoluminescence, and photoconductivity have been reported for semiconductor NW, rendering them promising materials for polarization sensitive optical and optoelectronic applications [151]. Two models have been proposed for explaining the optical anisotropy in semiconductor NWs depending on the diameter of the NWs in comparison with their exciton Bohr radius. For a quantum wire with diameter smaller than its exciton Bohr radius, the quantum confinement in two spatial directions gives rise to a valence-band mixing at the center of the Brillouin zone [56, 154]. The mixing of the heavy hole and light hole states leads to modified energies of the optical interband transitions and to a redistribution of the oscillator strength, resulting in an intrinsic optical anisotropy which can be tuned by the lateral confinement potential [155, 156]. On the other hand, for the NWs with diameter larger than the exciton Bohr radius but still smaller than the wavelength of interacting light, strong optical polarization anisotropy is observed and it is attributed to the polarization dependent electrostatic field in the NW due to a dielectric contrast between the NW and its environment [151]. In the context of the current $CsPbBr_3$ perovskite NW system, the diameter of the NW is around 12 nm which is larger than their exciton Bohr radius (~4 nm) [131, 144].

Therefore, there is only a weak quantum confinement in the $CsPbBr_3$ NWs reported in this thesis, thus the second model is suitable to explain the anisotropy in the PL of these NWs.

Since the light is essentially a form of electromagnetic radiation, the classical electromagnetic theory can be used to understand how the light pass through or propagate in a specific material. Maxwell's equations are the fundamental equations describing the evolution of electromagnetic fields under a certain condition. The equations include Gauss', Faraday's, and Ampère's laws, relating the electric flux density, electric field, magnetic flux density, magnetic field, charge density and current density to each other in space and time [157]. When the light interacts with a matter, a field will be generated in the matter. To describe the interactions of the matter with the electric and magnetic fields of light using electrodynamic theory, the properties of the materials, such as the complex dielectric function, are required as input parameters. These parameters can be obtained from either experimental data or calculations using solid state theory.

To determine the fields produced in the material as a response to the external field, the electric flux density $\vec{D}$ and the induced electrical polarization $\vec{P}$ need to be related to the electric field $\vec{E}$ according to

$$\vec{P} = \vec{D} - \varepsilon_0 \vec{E} = (\varepsilon_m - \varepsilon_0)\vec{E} = (\varepsilon\varepsilon_0 - \varepsilon_0)\vec{E} = \varepsilon_0(\varepsilon - 1)\vec{E} = \varepsilon_0 \chi \vec{E}, \tag{6.1}$$

where ε_m represents the permittivity, ε is the dielectric constant, a dimensionless term, and the susceptibility χ is defined as

$$\chi = \varepsilon - 1 = \chi_R + i\chi_I, \tag{6.2}$$

From microscopic aspect, the real part of the susceptibility χ is derived from the dipole response of atoms and electrons in the material to an electromagnetic wave, forming the basis of polarization.

Similarly, the magnetic field vector $\vec{H}$ is related to the magnetic flux density $\vec{B}$ by $\vec{B} = \mu_m \vec{H}$ with μ_m representing the permeability.

Since the spatial variation of $\vec{E}$ is related to a time variation of $\vec{H}$ and vice versa, the propagation of electromagnetic waves can be described explicitly by means of a wave equation.

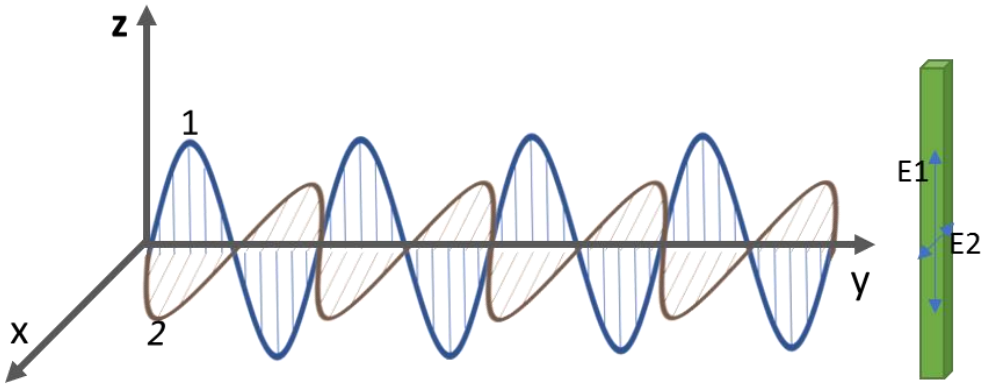

Figure 6.5: Schematic illustration of the photo-induced electric field in a NW depending on the polarization direction of the light (in **z** direction parallel to the NW or in **x** direction perpendicular to the NW)

Assuming that the electric field propagates in the **y** direction as shown in Figure 6.5, the propagation constant in the material is $k=2\pi/\lambda$ and the angular frequency is ω. The electric field $\vec{E}$ and the polarization $\vec{P}$ can be described as plane waves:

$$\vec{E} = \vec{E_0} e^{i(ky-\omega t)} \text{ and } \vec{P} = \vec{P_0} e^{i(ky-\omega t)}. \tag{6.3}$$

The electric field can be presented by the components of absorption, propagation and time dependence of a wave in a material:

$$\vec{E} = \vec{E_0} e^{-\frac{1}{2}\alpha y} \cdot e^{ik_y y} \cdot e^{i\omega t}, \tag{6.4}$$

where α is the intensity loss coefficient. The equation gives the magnitude, phase, and time dependence of the electric field propagating in the **y** direction in a material.

In a homogeneous medium, the electric and magnetic fields are continuous functions of space. However, at the boundary between two dielectric media, due to the absence of free electric charges and currents, the tangential components of the electric and magnetic fields $\vec{E}$ and $\vec{H}$ are continuous, while the electric and magnetic flux densities $\vec{D}$ and $\vec{B}$ are continuous.

According to the above discussion on the electrodynamic theory, in semiconductor NWs with 1D geometry, anisotropies in absorption, emission and scattering at different polarizations can be expected due to an ansiotropic dielectric screening of the electric field

For example, Wang et al. investigated the optical anisotropies of InP NWs satisfying the electrostatic limit [151]. Figure 6.6 illustrates the dielectric contrast model for explaining the optical anisotropies in the InP NW. This model is based on the anisotropic dielectric mismatch between the InP NW and its environment, i.e., the anisotropic refractive index contrast. In this model, the InP NW in the electrostatic limit is treated as an infinite dielectric cylinder in a vacuum. When the polarization of the incident field is parallel to the cylinder, the electric field inside the cylinder (E_i) is not reduced in comparison with the external electric filed (E_e), expressed by

$$E_{i\parallel} = E_{e\parallel}. \tag{6.5}$$

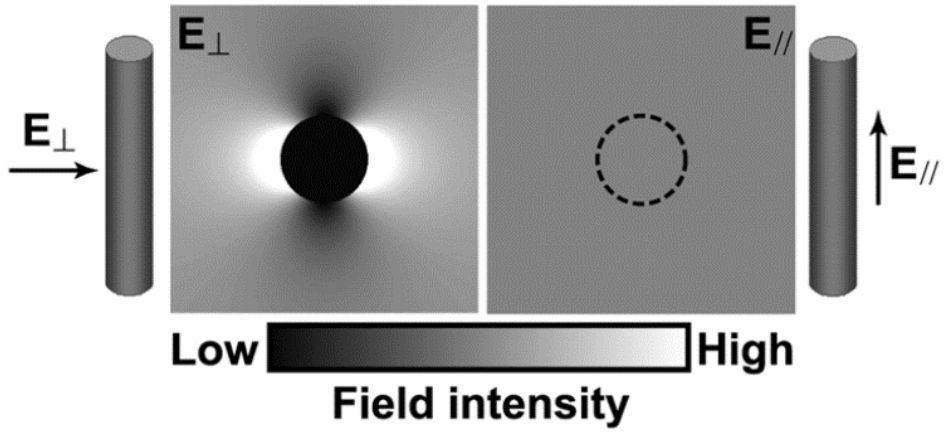

Figure 6.6: Dielectric contrast model of polarization anisotropy in InP NW. The laser polarizations are considered as electrostatic fields with depicted orientation. Field intensities are calculated from Maxwell's equations. It clearly shows that for the perpendicular polarization, the field is significantly attenuated inside the NW, whereas the field inside the NW is unaffected for the parallel polarization. From [66]. Reprinted with permission from AAAS.

On the contrary, while the polarization of the excitation is perpendicular to the axis of the NW, due to a dramatic difference in the dielectric constant between the NW and its surrounding, the intensity of the electric field in the NW is attenuated following the equation:

$$E_{i\perp} = E_{e\perp}\left(\frac{2\varepsilon}{\varepsilon(\omega)+\varepsilon}\right), \tag{6.6}$$

where ε is the dielectric constants of medium surrounding the NW (considered to be $\varepsilon = \varepsilon_0$), and $\varepsilon(\omega)$ is the wavelength dependent dielectric constant in the NW material due to light dispersion in the NW.

The polarization ratio of the NW is given by

$$P = \frac{I_{\parallel} - I_{\perp}}{I_{\parallel} + I_{\perp}} = \left[1 - \left(\frac{2\varepsilon_0}{\varepsilon_{NW} + \varepsilon_0}\right)^2\right] \Big/ \left[1 + \left(\frac{2\varepsilon_0}{\varepsilon_{NW} + \varepsilon_0}\right)^2\right]. \quad (6.7)$$

In their InP NW system, the dielectric constant of the material is very large, which is reported to be $\varepsilon(\text{InP}) = 12.4\varepsilon_0$. Thus that the calculated polarization ratio is P =0.96, matching well with the value determined by their experiment.

The $CsPbBr_3$ perovskite NWs reported in this thesis are analogous to the InP NWs reported by Wang [151]. As discussed in the introduction, these $CsPbBr_3$ NCs are also semiconductrors with a reported dielectric constant of $\varepsilon(CsPbBr_3) = 4.96\varepsilon_0$ [131]. These NWs do not belong to the class of 1D quantum wires because their diameter (~12 nm) is larger than the exciton Bohr radius of this material. Nevertheless, due to a highly anisotropic geometry and high dielectric contrast compared to its surroundings, these $CsPbBr_3$ perovskite NWs are expected to show an anisotripc interaction with incident light polarization. Assuming that the $CsPbBr_3$ perovskite NW is aligned in the **z** direction as schematically illustrated in figure 6.5, and the light propagates in the **y** direction. Light 1 has the polarization in **z** direction, parallel to the direction of NW, while the polarization of light 2 is in along **x** direction, perpendicular to the direction of NW. According to the discussion above, due to a dielectric contrast between the $CsPbBr_3$ perovskite NW and the surrounding medium, the electric field along the **x** and **z** direction in the NW will be different. Using a similar electrostatic model as the one described in the InP NW system, the field intensity of light 1 inside the $CsPbBr_3$ perovskite NW should not be reduced. In contrast, according to equation 6.6, the field intensity of light 2 in the $CsPbBr_3$ perovskite NW is calculated to be attenuated by 2/3 considering a dielectric constant of $\varepsilon_{NW}(CsPbBr_3) = 4.96\varepsilon_0$. Considering an un-polarized incident light which means that the initial field intensity of the light 1 and light 2 outside the NW are the same, the field intensity at the **x** direction in the NW is only 1/3 of that in the **z** direction. This will lead to an anisotropic PL of the NW, and the theoretical polarization ratio of the $CsPbBr_3$ perovskite NW is determined

to be 0.8 according to equation 6.7. However, the $CsPbBr_3$ perovskite NWs formed by the oriented-attachment of nanocubes have a rectangular shaped cross section instead of round shape as assumed for the modeling of polarization in InP NW, making a difference in reality.

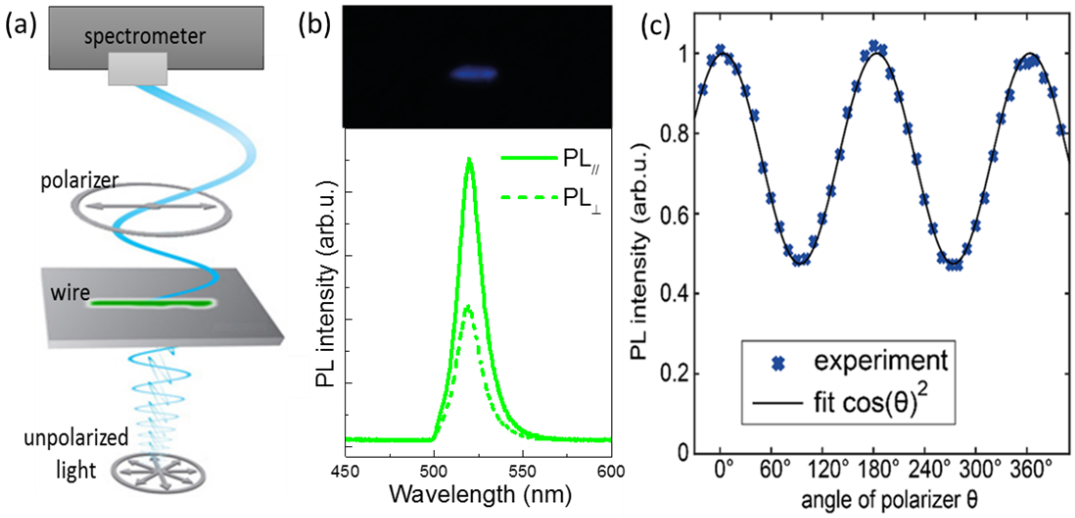

Figure 6.7: (a) Schematic illustration of experimental measurement of polarization-dependent PL in $CsPbBr_3$ perovskite NWs on the substrate. The NWs are excited by an unpolarized light and a polarizer is placed between the NWs and the spectrometer to examine the polarization anisotropy of PL from NWs. (b) PL spectra obtained when the polarizer axis is parallel (solid lines) or perpendicular (dashed line) to the direction of the NW, a substantial difference can be observed. Inset is the image of NWs due to scattering of blue excitation light. (c) PL intensity (blue crosses) as a function of polarizer angle and the fitting by $\cos^2\theta$ function (black line), the maximum PL intensity is normalized as 1.

In order to check the optical polarization anisotropy, polarization dependent PL measurements are carried out on the $CsPbBr_3$ perovskite NWs. Well-separated NWs on the substrate are prepared by spincoating a dilute solution of colloidal NWs. As illustrated in figure 6.7 (a), $CsPbBr_3$ perovskite NW on a substrate is illuminated with an un-polarized light in a dark field setup. A polarizer was mounted between the NW and the spectrometer to determine the polarization of the PL from the NW. When the NWs are illuminated by the excitation light, the dark field scattering enables the determination of the position of the wire-like particles as shown in figure 6.7 (b). However, it is difficult to determine whether it is a single NW or a bundle of parallelly aligned NWs. The setup also enables the comparison of the PL spectrum obtained when the direction of the polarizer is parallel or perpendicular to the direction of the NW. A dramatic difference between the intensity

of the PL with different polarization direction can be seen, indicating an anisotropic PL emission in the $CsPbBr_3$ NWs. The angle of the polarizer is continuously changed and the PL spectra at various detecting angles are recorded. The maximum values of the PL intensity are extracted from the PL spectra and plotted as a function of the polarizer angle as shown in figure 6.7 (d). As expected, the PL intensity shows a periodic variation with the change of polarizer angle and the experimental results can be well fitted with a $\cos^2\theta$ function, with θ representing the angle between the NW and the polarizer. This can be explained by the Malus's Law [158].

According to Malus's Law, when a perfect polarizer is placed in a polarized beam of light, the irradiance, *I*, of the light that passes through is given by

$$I = I_0 \cos^2 \theta . \tag{6.8}$$

where I_0 is the initial intensity and θ is the angle between the light's initial polarization direction and the axis of the polarizer. This can be understood by considering the transmission of the electric vector of the light through the polarizer. The electric field vector $\overrightarrow{E_0}$ can be resolved into two rectangular components, i.e. $\overrightarrow{E_0}\cos\theta$ and $\overrightarrow{E_0}\sin\theta$. The analyzer will transmit only the component which is parallel to its transmission axis, namely the $\overrightarrow{E_0}\cos\theta$, and the intensity of the light is proportional to the square of electric vector amplitude, i.e.

$$I \propto E^2 . \tag{6.9}$$

Thus that the intensity of the light detected by the spectrometer will follow equation 6.8 and can explain the results presented in figure 6.7 (c). Particularly, at θ =90° and θ =270°, meaning that the polarizer is parallel to the investigated $CsPbBr_3$ perovskite NW, the PL intensity shows a maximum value. By contrast, when θ equals 0°, 180° and 360°, meaning that the polarizer is perpendicular to the NW, a minimum PL intensity is observed. However, the minimum PL intensity is not 0, but rather 0.47 times of the maximum intensity ($I_\perp = 0.47 I_\parallel$). The result strongly indicates that the emission from the $CsPbBr_3$ perovskite NW shows a polarization anisotropy in PL yet not completely polarized. If the PL is fully polarized, then the minimum PL intensity should have a zero value according to equation 6.8.

The polarization anisotroy of the $CsPbBr_3$ perovskite NW is calculated to be $P_{NW}(CsPbBr_3)=0.36$ according to equation 6.8, which is much smaller than the theoretical value calculated using the dielectric contrast model (0.8). A few possible reasons are postulated to be responsible for this deviation. Firstly, the $CsPbBr_3$ perovskite NWs are actually surrounded by organic capping ligands, resulting in a reduced dielectric constant contrast between the NW and the surroundings, thus leading to a smaller polarization ratio. Secondly, the $CsPbBr_3$ perovskite NWs tend to attach to each other and form bundles. In fact, the selected area shown in figure 6.7 (c) more likely contains a bundle of NWs rather than a single NW. The NWs in the bundle cannot perfectly align in the same direction, causing a decrease in the polarization ratio. Nevertheless, the anisotropic PL in $CsPbBr_3$ perovskite NWs is a result of the anisotropic quasi 1D geometry of the NWs. In contrast, no PL anisotropy is detected in the nanocubes with an isotropic shape.

6.2.2 Comparison of photoluminescence quantum yield and decay rates

The elongated shape of $CsPbBr_3$ perovskite NWs not only makes them polarized emitters, but also affects the recombination of excited charge carriers compared with their nanocube counterparts. This section presents a comparative study on the charge carrier recombination in $CsPbBr_3$ perovskite NWs and nanocubes by using steady-state and time-resolved PL spectroscopy. Figure 6.8 (a) presents the absorption and PL spectra of $CsPbBr_3$ perovskite NWs and nanocubes dispersed in hexane with corresponding photographs under room light and UV light shown as insets. First, obvious difference between NWs and nanocubes can be seen from the appearance of the respective colloidal solutions. $CsPbBr_3$ perovskite nanocubes form a clear solution while NWs precipitates due to their larger mass and aggregation. The NW dispersion is diluted and stirred well for optical characterizations. The colloidal $CsPbBr_3$ NW dispersion exhibits a sharp excitonic absorption peak at around 515 nm and a narrow PL emission (FWHM=22nm) centered at 520 nm. Whereas the nanocube dispersion shows broad excitonic absorption peak at 510 nm and a PL at ~ 515 nm.

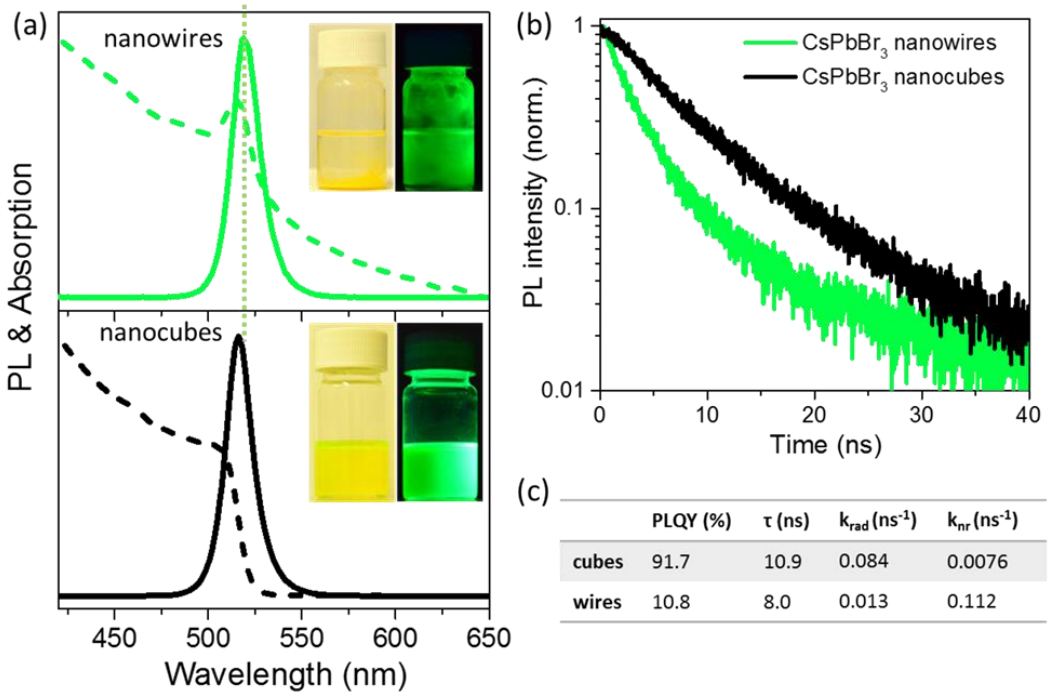

(c)

	PLQY (%)	τ (ns)	k_{rad} (ns^{-1})	k_{nr} (ns^{-1})
cubes	91.7	10.9	0.084	0.0076
wires	10.8	8.0	0.013	0.112

Figure 6.8: (a) Comparison of PL and absorption spectra of NW (top) and nanocube (bottom) dispersions. The insets are the photos of the dispersion under room light (left) and UV light (right). (b) PL decay curve of $CsPbBr_3$ NW (green line) and nanocube (black line) dispersions. (c) Table comparing the PLQYs, PL lifetimes and calculated PL decay rates of the NWs and nanocubes.

Moreover, the colloidal dispersion of $CsPbBr_3$ perovskite NWs exhibits a weak green emission as compared with the dispersion of nanocubes under UV light illumination. Indeed it is found that the colloidal dispersion of NWs exhibit a much lower PLQY as compared to that of nanocube dispersion. In addition, time-resolved PL measurements show that the NWs decay faster compared to nanocubes, as depicted in figure 6.8 (b). A combination of PLQY and PL decay time (τ, obtained by fitting the decay curve) enables the calculation of radiative and nonradiative decay rates according to equation 5.14 and the results are presented in figure 6.8 (c). The results clearly show that the NWs have a much larger nonradiative decay rate compared with nanocubes, meaning that there is a higher possibility for the charge carriers to recombine through nonradiative channels instead of radiative channel in the NWs. Whereas the opposite happens in the nanocubes, in which the radiative recombination of the charge carriers is the dominant process.

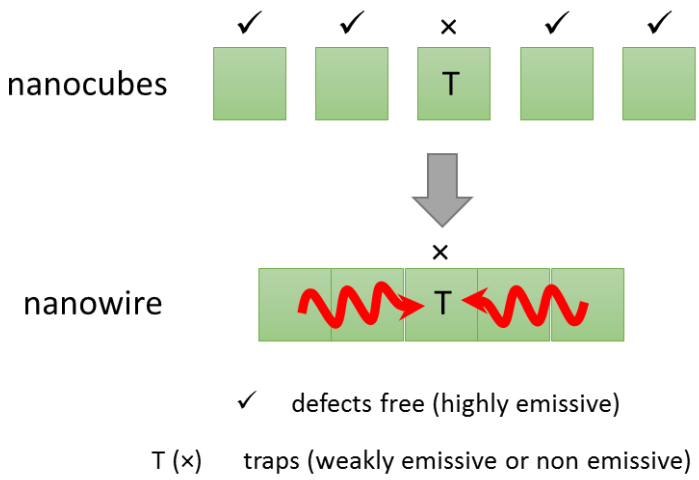

Figure 6.9: Schematic illustration of different carrier recombination processes in nanocubes and a NW.

The differences in the decay rates are attributed to the different shapes of $CsPbBr_3$ perovskite NCs, as schematically illustrated in figure 6.9. In the case of nanocubes, the effective surface passivation by ligands reduces the density of traps and suppresses the trap-assisted nonradiative processes. Moreover, as discussed earlier, the nanocubes are weakly quantum-confined and this increases the probability of the interaction between the photogenerated electrons and holes thus leading to an increase in the radiative recombination rate. However, the PLQY is not 100% due to the presence of a small percentage of nanocubes with defects. In contrast, in the case of NWs, the purification step leads to the removal of surface ligands and causes an increased number of defects at the surface. Furthermore, as the NW has a length of several micrometers, the delocalization of the excitons becomes stronger in the elongated NCs. Consequently, the exciton is more likely to encounter a trap during its diffusion within the long NW, thereafter loss the energy nonradiatively rather than emitting photons. Considering the fact that the NWs are made up by the nanocubes, if some of the nanocubes initially contain trap states, the probability that excitons from neighboring nanocrystal diffuse to the trap and recombine there nonradiatively will be strongly enhanced.

For further insights about the the differences in the recombination processes in these $CsPbBr_3$ perovskite NWs and the nanocubes, temperature dependent PL measurements are carried out on these samples and the results are presented in figure 6.10.

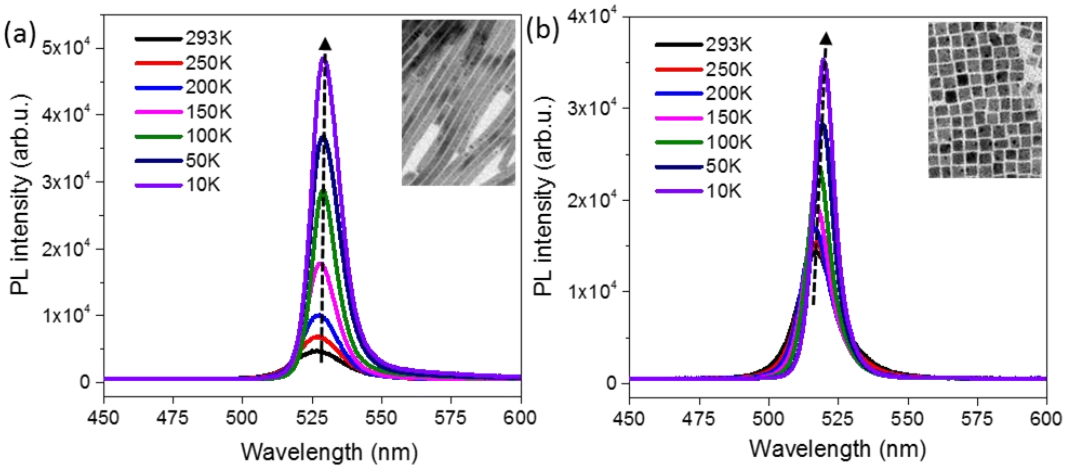

Figure 6.10: PL spectra of (a) $CsPbBr_3$ perovskite NW and (b) nanocube samples at different temperatures. Insets are the TEM images showing the morphology of the corresponding sample. The arrows indicate the increase tendency in the PL intensity with the decrease of temperature.

Figure 6.10 (a) and (b) display the PL spectra of $CsPbBr_3$ perovskite NWs and nanocubes at different temperature with the insets showing the TEM images of corresponding sample, respectively. It can be seen that the PL intensities for both NWs and nanocube sample show gradual increase with the decrease of temperature. However, the increase in the NW sample is more significant than that in the nanocube sample. The significantly enhanced PL intensity of NWs with decreasing temperature indicates that the nonradiative recombination process in the NWs is effectively suppressed at low temperature.

The temperature dependent PL intensity is normally analyzed by using the Arrhenius equation [159, 160]. For one nonradiative recombination channel, the Arrhenius formula is given by

$$I(T) = \frac{I_0}{1 + a\exp(-E_a/k_B T)}, \tag{6.10}$$

where $I(T)$ is the integrated PL intensity at temperature of T, I_0 is the integrated PL intensity at 0 K. E_a is the activation energy of nonradiative channel and k_B is the Boltzmann's constant. The parameter a is related to the radiative and nonradiative processes, given by

$$a = \frac{\tau_r}{\tau_{nr}} = \frac{k_{nr}}{k_r}, \tag{6.11}$$

where τ_r and τ_{nr} are the radiative and nonradiative lifetimes of carriers, respectively, k_r and k_{nr} are the rates of radiative and nonradiative processes, respectively [159].

In $CsPbBr_3$ perovskite NWs, the ratio between radiative and nonradiative decay rate at room temperature is around 100 times larger than that of nanocubes (figure 6.8 (c)), meaning a larger parameter "*a*" in NWs than in nanocubes. According to equation 6.10, when the temperature increases from 0 K, the PL intensity of the $CsPbBr_3$ perovskite NWs drops more steeply than the nanocubes and this is in agreement with the experimental results shown in figure 6.10.

6.3 Electronic coupling in $CsPbBr_3$ nanocube subunits of perovskite supercrystals

In the previous section, the differences in the optical properties and carrier recombination behaviors in $CsPbBr_3$ perovskite NWs and nanocubes have been discussed. The NWs are formed through an oriented attachment of nanocubes and they exhibit redshifted PL but significantly decreased PLQY in comparison with the nanocubes. This section will focus on the self assembly of $CsPbBr_3$ nanocubes into supercrystals and the resultant optical properties. It is found that the PL of $CsPbBr_3$ perovskite nanocubes can also be tuned by assembling them into supercrystals while the high PLQY can be retained.

6.3.1 Optical properties of self-assembled $CsPbBr_3$ supercrystals

As discussed earlier, $CsPbBr_3$ nanocubes can be prepared by a simple single-step tip sonication of precursor powders. It is also shown that the nanocubes transform into NWs under prolonged ultrasonication. Interstingly, it is found that the increase of precursor concentration in the reaction medium leads to the precipitation of preformed particles and the obtained precipitates exhibit strong green PL under UV light illumination (inset in figure 6.11 (a)) [161]. This is different from bulk-like $CsPbBr_3$ big crystals in which a weak PL is expected due to trap-assisted nonradiative process [144, 162].

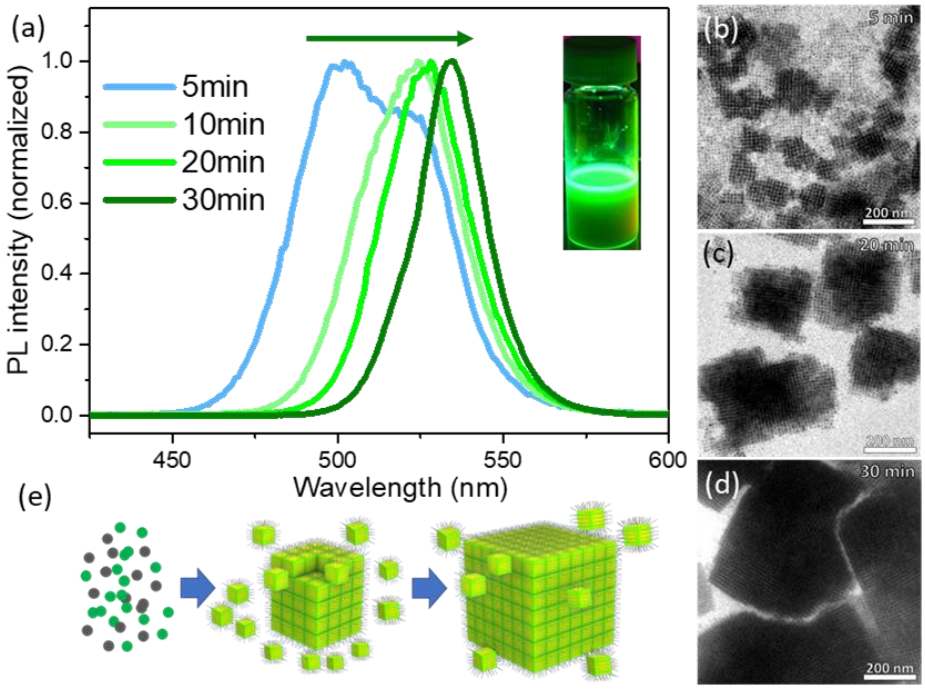

Figure 6.11: (a) PL spectra of $CsPbBr_3$ perovskite supercrystal colloids obtained at different reaction time. Inset is the photo of supercrystal colloids under UV light. (b)-(d) TEM images of $CsPbBr_3$ perovskite supercrystals obtained at different reaction time. (e) Schematic illustration of the formation of $CsPbBr_3$ perovskite supercrystals through spontaneous self-assembly of NCs.

To understand the optical properties of these precipitated particles, the PL of the reaction medium is monitored over a period of time during the formation of precipitates and the spectra are depicted in figure 6.11 (a). The PL spectra clearly show a redshift with increasing reaction time. After 5 min, the PL spectrum shows two peaks, one is centered at ~500 nm while the other is centered at ~530 nm. As discussed earlier, the $CsPbBr_3$ nanocubes of size ~12 nm exhibit PL at ~515 nm and they are formed by seeded growth during tip-sonication [130]. Therefore, the PL spectra clearly suggest the presence of smaller $CsPbBr_3$ NCs in the reaction medium. This is further evidenced by the TEM image in figure 6.11 (b), where the NCs with diameter of ~ 8 nm can be identified. It is worth noting that no big crystals are present, while instead, some clusters comprising NCs can be observed, which are expected to be the origin of the redshifted PL peak at ~530 as displayed in figure 6.11 (a).

As the reaction proceeds further, the PL spectrum of the colloidal solution gradually changes over time. At 10 min, the PL peak at 500 nm vanishes and the main peak is slightly redshifted to 532

nm with a shoulder peak arising at ~515 nm. The shoulder peak matches well with the normal $CsPbBr_3$ perovskite nanocubes with diameter of ~12 nm as demonstrated before. After 20 min and 30 min, the ratio of the shoulder component significantly decreases and the major peak redshifted to ~ 535nm. The change in PL spectrum is associated with the change of NC morphology as shown by the TEM images in figure 6.11 (c) and (d). It can be seen that at 20 min, NC assemblies with sizes of several hundreds nanometers are present, which consist of small nanocube subunits of size ~12 nm. While at 30 min, larger assemblies comprising nanocubes can be seen, the nanocubes are closely packed thus forming well-packed polyhedral supercrystals.

In fact, in the past two decades, tremendous efforts have been devoted to the self-assembly of metal and conventional semiconductor NCs into supercrystals to control their optical, magnetic and electrical properties [163-168]. The self-assembly process is typically accomplished by several methods, 1) slow solvent evaporation of the concentrated colloidal NC solution, 2) self-assembly at air/liquid or liquid/liquid interfaces-Langmuir technique, and 3) interactions between NCs via surface ligands by incorporating anti-solvent [165-167, 169]. In the present $CsPbBr_3$ supercrystal system, based on the results presented above, it is most likely that the formation of the $CsPbBr_3$ perovskite supercrystal occurs in colloidal solution. As schematically illustrated in figure 6.11 (e), once the $CsPbBr_3$ perovskite NCs are formed in the solution, they spontaneously self-assemble into supercrystals and precipiate at the bottom of the reaction vial due to their heavy mass. The supercrystal colloidal solution clearly show distinct optical properties with redshifted emission compared to the nanocube colloidal solution. The PL shift due to the energy transfer to large NCs can be ruled out based on the fact that no larger size crystals are observed from TEM measurements. Hence the low energy PL peak at 535 nm is attributed to the supercrystals present in the colloidal solution

6.3.2 Electronic coupling and minibands formation in nanocube assemblies

The results presented above clearly show that the self-assembled $CsPbBr_3$ nanocubes exhibit a redshift of ~20 nm in their PL compared to that of the the isolated NCs. To further understand the origin of the redshift in the supercrystals, the optical properties of perovskite films made of isolated NCs and supercrystals are characterized by comparing their PL and PLE spectra, which are depicted in figure 6.12 (a).

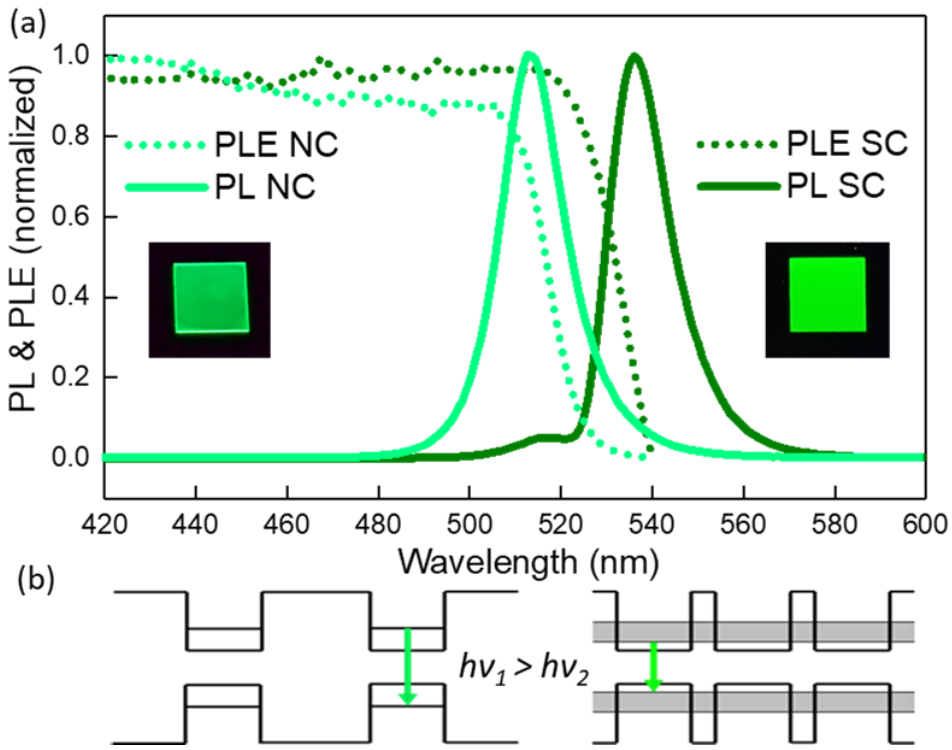

Figure 6.12: (a) PL (solid lines) and PLE (dashed lines) spectra of $CsPbBr_3$ perovskite NC film (light green lines, labeled as NC) and supercrystal film (dark green lines, labeled as SC). Insets show the photos of NC film (left) and supercrystal film (right) under UV light. (b) Schematic illustration of the miniband formation through the electronic coupling between neighboring $CsPbBr_3$ perovskites NCs in supercrystals.

In fact, the difference of isolated NC and supercrystal film can be seen from the emission colours under UV illumination (insets of figure 6.12 (a)). Both films are highly luminescent and the NC film (left) shows a cayan green color while the supercrystal film (right) exhibits pure green, indicating a redshifted PL in the supercrystal film. The PL of supercrystal film exhibits a major PL peak centered at 538 nm with a small shoulder remaining at 515 nm, and these peaks are attributed to supercrystals and isolated NCs, respectively. The redshift in the photoluminescence of perovskite supercrytals is likely due to the electronic coupling between individual NC subunits. Such electronic coupling has been reported in a variety of semiconductor NC assemblies [59-61, 170, 171]. In $CsPbBr_3$ perovskite nanocubes, as discussed earlier, they exhibit a certain degree of quantum confinement and show blueshifted PL compared to their bulk counterpart. While the nanocubes are assembled into supercrystals, if the spacing between neighboring NCs are sufficiently small, the wavefunctions of the NC subunits can interact strongly, and lead to the formation of minibands in both VB and CB, as illustrated in figure 6.12 (b). Such miniband

formation lowers the bandgap of supercrystals and leads to redshifted PL. Further evidence for the electronic coupling of nanocube subunits comes from the redshift in the PLE specrum of supercrystals compared to that of isolated NCs as shown in the figure 6.12 (a).

The minibands in quantum well superlattice have been widely reported in literature and they are also discussed in the introduction chapter as well as in chapter 5 to explain the PL redshift in the stacked 2D perovskite NPls [105]. These minibands are formed for the tunneling of both the electrons and holes. The width of the miniband depends on how much the wave function can penetrate into the classical forbidden area, and it can be calculated based on the Kronig-Penney model using the effective mass approximation [172, 173]. The width of the miniband for conventional semiconductor quantum well superlattice, for example GaAs/AlAs superlattice has been calculated, and it was concluded that the coupling of the electronic wavefunction decreases with increasing barrier thickness provided the thickness of the quantum well stays constant [60]. While in the case of constant barrier thickness, decreasing the thickness of quantum well will increase the energy of the subband states. The reported calculations clearly indicate that the width of the miniband can be tuned in between zero and a few hundreds meV [60]. In GaAs/AlAs superlattice, the width of the heavy-hole miniband is narrower than that of electron miniband due to a larger effective mass of heavy holes. While in the case of perovskite supercrystals, as the effective masses of electrons and holes are similar in the $CsPbBr_3$ NC subunits, the tunneling effects should be similar thus yielding a similar miniband formation for the electron and hole energy states, as schematically displayed in figure 6.12 (b).

The coupling strength in the NC assemblies is determined by the distance between the adjacent NCs. When the inter-particle distance is between 0.5 and 10 nm, the interaction between NCs is dominated by dipolar coupling [27], leading to an electronic energy transfer [174, 175]. Energy transfer often occurs in solids containing two or more size distributions of NCs, in which the energy transfer to the larger particles having lower bandgaps. Energy transfer has been experimentally realized in many artificial semiconductor NC assemblies [176-180]. When the distance between neighboring NCs in an assembly is smaller than 0.5 nm, exchange interactions become significant, and electronic excitations are delocalized over many NCs. It has been shown that in closely packed NC assemblies, the electronic wavefunctions of the NCs extend toward

neighboring NCs [181, 182]. For example, it is reported that the optical spectra of closely packed CdSe NC assemblies are similar to those of bulk CdSe [182].

In the case of $CsPbBr_3$ perovskite supercrystals, the length of the capping ligands (oleylamine and oleic acid) for the initial NCs is around 1.8 nm. However, when the NCs self-assemble into close-packed superlattices, the ligands can be compressed due to their soft nature [183, 184]. The inter-particle distance in the $CsPbBr_3$ perovskite supercrystals determined from electron microscope images is in the range of 0.5 nm to 1.5 nm. Therefore, both resonance energy transfer and electronic coupling by tunneling effect can be postulated to be present in the supercrystals. However, the TEM images show that there is only one size distribution of NCs in the superlattices and this can exclude the energy transfer process from small NCs to large NCs.

According to the above discussion, by assembling $CsPbBr_3$ perovskite NCs into supercrystals, the optical properties can be tuned through the electronic coupling between the neighboring NCs. These NC assemblies exhibit bulk-like optical properties due to a carrier delocalization, while the assemblies preserve the high PLQY of NC due to a lower density of trap states compared to the bulk crystals. Therefore, the $CsPbBr_3$ perovskite NC assemblies exhibit unique optical properties compared with the isolated NCs and the bulk materials. For example, Manzi et al. recently reported that multiple exciton generation in $CsPbBr_3$ perovskite NC assemblies can be induced by resonant multiphoton absorption, while this phenomenon is absent in isolated NCs. This is attributed to a suppressed Auger recombination in the NCs that are closely packed to each other [185]. Moreover, as the optical properties can be further controlled by adjusting the inter-particle distance as well as the size of the semiconductor NCs, the new collective phenomena in these $CsPbBr_3$ perovskite NC assemblies offer enormous possibility in the design of novel materials with controlled optical and electronic properties. Furthermore, these NC assemblies not only provide a unique model system for the study of fundamental physical processes, such as charge carrier transport, exciton diffusion, and energy transfer, etc., but also open a new avenue toward the fabrication of new devices with novel optical properties.

6.4 Summary

This chapter deals with the spontaneous self-assembly of $CsPbBr_3$ perovskite nanocubes into larger structures including NWs and supercrystals and the resultant optical properties with morphology changes. First, by combining absorption spectroscopy and morphological characterization, it is revealed that $CsPbBr_3$ perovskite NWs are formed through an oriented-attachment of nanocubes in the colloidal solution. The NWs exhibit a slightly redshifted PL with respect to corresponding nanocubes due to the elongated morphology and carrier delocalization. The anisotropic shape of $CsPbBr_3$ perovskite NWs endows them an optical anisotropy, which is revealed by the polarization anisotropy in the PL of the NWs. Compared with nanocubes, the $CsPbBr_3$ perovskite NWs exhibit a much lower PLQY and shorter PL decay time due to a dominant nonradiative recombination. This is attributed to the carrier diffusion in the NWs and resultant trap-assisted nonradiative process. Furthermore, it is shown that the supercrystals obtained from self-assembly of nanocubes exhibit distinct optical propeprties with redshift in their emission compared to that of isolated NCs. The redshift is attributed to the interparticle electronic coupling of nanocube subunits in the supercrystals. The $CsPbBr_3$ supercrystals exhibit bulk like optical properties while the high PLQY of the NC subunits can be retained.

7. Conclusions and outlook

In this thesis, luminescent organic-inorganic hybrid and all-inorganic perovskite NCs were prepared with controlled dimensionalities and their optical properties were investigated in correlation with their shape, size and dimensionality. The synthesis of colloidal perovskite NCs were performed by two different approaches, namely ligand-assisted reprecipitation and ultrasonication of precursor powders. Various colloidal NCs with different shapes such as nanocubes, NPls with tunable thicknesses, and NWs have been successfully synthesized for studying their optical properties.

In the first part of the thesis, quantum confinement effects in the organic-inrganic hybrid perovskite ($MAPbBr_3$) NPls were explored. The dimensionality of the hybrid perovskite colloidal NCs can be changes from 3D cubes to 2D NPls in the presence of long chain alkylammonium cations and the thickness of the hybrid NPls were controlled from few monolayers to merely single layer. This enabled the quantitative study of the quantum confinement effects in these perovskite NPls for the first time, thus correlating the respective PL positions of NPls with their thicknesses.

To increase the stability and PLQY of colloidal perovskite NCs, the organic cation MA^+ of hybrid perovskites was replaced by Cs^+ to obtain highly luminescent all-inorganic $CsPbX_3$ (X=Cl, Br, I) perovskite colloidal NCs. The optical properties of these $CsPbX_3$ NCs can be effectively tuned by halide composition as well as dimensionality. It was shown that the shape of $CsPbX_3$ NCs changed from nanocubes to NPls with decreasing the molar ratio of Cs to Pb precursors in the reaction. The quasi-3D $CsPbBr_3$ and $CsPbI_3$ nanocubes exhibited weak quantum confinement while the 2D NPls showed strong quantum confinement. The thickness-dependent optical properties of these colloidal NCs were investigated by using steady-state absorption and PL spectroscopy as well as time-resolved PL spectroscopy. The colloidal NPls showed sharp excitonic absorption peaks with blueshifted PL compared to the corresponding nanocubes. The PL decay became faster with decrease of NPl thickness due to increased radiative and nonradiative recombination rates.

The synthesis of NPls was optimized to obtain $CsPbBr_3$ NPls with narrow emission and tunable thickness from 2 to 6 monolayers. By fitting the absorption spectra of perovskite NPls with Elliot's formula, it was revealed that the exciton binding energy increased with decreasing the thickness of NPls. For the thinnest NPls (2ML), the exciton binding energy was found to be ~280 meV while for the quasi-3D nanocubes it was only ~40 meV. The as-synthesized thin colloidal NPls generally exhibit relatively low PLQY compared to that of the nanocubes due to a high surface defects density. In this thesis it was discovered that the post-synthetic surface treatment of NPls with $PbBr_2$ led to a dramatic enhancement of their PL through trap sate repair. Time-resolved PL revealed that the radiative excitonic recombination became prominent after the repair of traps and and the PL decay became monoexponential.

The second part of this thesis showed that the $CsPbBr_3$ perovskite nanocubes can self-assemble into either NWs or supercrystals depending on the reaction parameters and this enabled the investigation of shape-dependent optical properties. It was found that the prolonged ultrasonication of precursors led to the transformation of $CsPbBr_3$ nanocubes into single crystalline NWs with a similar crystal structure as nanocubes. The morphological characterization in combination with absorption spectroscopy revealed that the NWs were formed through an oriented attachment of pre-formed nanocubes in the colloidal solution. The $CsPbBr_3$ NWs exhibited a redshifted PL with much lower PLQY and shorter PL decay time compared to those of the $CsPbBr_3$ nanocubes. These were attributed to the charge carrier delocalization in the NWs, which resulted in an increased probability for the trap-assisted nonradiative recombination of the charge carriers. The nonradiative process can be effectively suppressed at low temperature hence the NWs showed a steeper increase in the PL intensity with decreasing temperature compared with the nanocubes. Moreover, due to the anisotropic geometry and a dielectric contrast between the NWs and their surroundings, the $CsPbBr_3$ NWs exhibited polarization anisotropy in their PL.

The experimental parameters are quite sensitive to the final geometry of perovskite NCs. Interestingly, it was discovered that the pre-formed $CsPbBr_3$ nanocubes could spontaneously self-assemble into supercrystals with distinct optical properties. The supercrystals exhibited redshifted emission compared to that of uncoupled perovskite NCs. The redshifted emission is attributed to the miniband formation through the electronic coupling between neighboring nanocube subunits

of supercrystals. Importantly, in contrast to the NWs, the supercrystals preserved the high PLQY of the the NC subunits.

In summary, this thesis has presented a detailed study of shape, size and dimensionality dependent optical properties of colloidal lead halide perovskite NCs. Controllable synthesis has been achieved to obtain monodisperse colloidal NCs of various shapes such as nanocubes, NWs, NPls and supercrystals, thus enabling the study of their optical properties. The results of this study is likely to have significant impacts in the emerging field of low-dimensional perovskites for optoelectronic applications. The promising results of this PhD thesis has been communicated in scientific journals as listed in publications.

Bibliography

[1] H.L. Wells, Über die Cäsium- und Kalium-Bleihalogenide, Zeitschrift für anorganische Chemie, 3 (1893) 195-210.
[2] C.K. MØLler, A phase transition in cæsium plumbochloride, Nature, 180 (1957) 981-982.
[3] C.K. MØLler, Crystal structure and photoconductivity of cæsium plumbohalides, Nature, 182 (1958) 1436.
[4] D. Weber, $CH_3NH_3PbX_3$, ein Pb(II)-System mit kubischer Perowskitstruktur, Zeitschrift für Naturforschung B, 33 (1978) 1443-1445.
[5] E. Wainer, High titania dielectrics, Transactions of The Electrochemical Society, 89 (1946) 331-356.
[6] R. Willett, H. Place, M. Middleton, Crystal structures of three new copper(II) halide layered perovskites: structural, crystallographic, and magnetic correlations, Journal of the American Chemical Society, 110 (1988) 8639-8650.
[7] X. Hong, T. Ishihara, A.V. Nurmikko, Dielectric confinement effect on excitons in PbI_4-based layered semiconductors, Physical Review B, 45 (1992) 6961-6964.
[8] E. Hanamura, N. Nagaosa, M. Kumagai, T. Takagahara, Quantum wells with enhanced exciton effects and optical non-linearity, Materials Science and Engineering: B, 1 (1988) 255-258.
[9] D.B. Mitzi, C.A. Feild, W.T.A. Harrison, A.M. Guloy, Conducting tin halides with a layered organic-based perovskite structure, Nature, 369 (1994) 467-469.
[10] D.B. Mitzi, S. Wang, C.A. Feild, C.A. Chess, A.M. Guloy, Conducting layered organic-inorganic halides containing <110>-oriented perovskite sheets, Science, 267 (1995) 1473-1476.
[11] T. Hattori, T. Taira, M. Era, T. Tsutsui, S. Saito, Highly efficient electroluminescence from a heterostructure device combined with emissive layered-perovskite and an electron-transporting organic compound, Chemical Physics Letters, 254 (1996) 103-108.
[12] C.R. Kagan, D.B. Mitzi, C.D. Dimitrakopoulos, Organic-inorganic hybrid materials as semiconducting channels in thin-film field-effect transistors, Science, 286 (1999) 945-947.
[13] A. Kojima, K. Teshima, Y. Shirai, T. Miyasaka, Organometal halide perovskites as visible-light sensitizers for photovoltaic cells, Journal of the American Chemical Society, 131 (2009) 6050-6051.
[14] M.M. Lee, J. Teuscher, T. Miyasaka, T.N. Murakami, H.J. Snaith, Efficient hybrid solar cells based on meso-superstructured organometal halide perovskites, Science, 338 (2012) 643.

[15] J. Burschka, N. Pellet, S.-J. Moon, R. Humphry-Baker, P. Gao, M.K. Nazeeruddin, M. Grätzel, Sequential deposition as a route to high-performance perovskite-sensitized solar cells, Nature, 499 (2013) 316-319.
[16] M. Liu, M.B. Johnston, H.J. Snaith, Efficient planar heterojunction perovskite solar cells by vapour deposition, Nature, 501 (2013) 395-398.
[17] Newcomer juices up the race to harness sunlight, Science, 342 (2013) 1438.
[18] M. Peplow, HENRY SNAITH: Sun worshipper. An energetic physicist pushes a promising solar-cell material into the spotlight, Nature, 504 (2013) 357-365.
[19] S.D. Stranks, G.E. Eperon, G. Grancini, C. Menelaou, M.J.P. Alcocer, T. Leijtens, L.M. Herz, A. Petrozza, H.J. Snaith, Electron-hole diffusion lengths exceeding 1 micrometer in an organometal trihalide perovskite absorber, Science, 342 (2013) 341-344.
[20] G. Xing, N. Mathews, S. Sun, S.S. Lim, Y.M. Lam, M. Grätzel, S. Mhaisalkar, T.C. Sum, Long-range balanced electron- and hole-transport lengths in organic-inorganic organic-inorganic $CH_3NH_3PbI_3$, Science, 342 (2013) 344-347.
[21] D. Bi, A.M. El-Zohry, A. Hagfeldt, G. Boschloo, Improved morphology control using a modified two-step method for efficient perovskite solar cells, ACS Applied Materials & Interfaces, 6 (2014) 18751-18757.
[22] Z.-K. Tan, R.S. Moghaddam, M.L. Lai, P. Docampo, R. Higler, F. Deschler, M. Price, A. Sadhanala, L.M. Pazos, D. Credgington, F. Hanusch, T. Bein, H.J. Snaith, R.H. Friend, Bright light-emitting diodes based on organometal halide perovskite, Nature Nanotechnology, 9 (2014) 687-692.
[23] G. Xing, N. Mathews, S.S. Lim, N. Yantara, X. Liu, D. Sabba, M. Grätzel, S. Mhaisalkar, T.C. Sum, Low-temperature solution-processed wavelength-tunable perovskites for lasing, Nature Materials, 13 (2014) 476-480.
[24] L.C. Schmidt, A. Pertegás, S. González-Carrero, O. Malinkiewicz, S. Agouram, G. Mínguez Espallargas, H.J. Bolink, R.E. Galian, J. Pérez-Prieto, Nontemplate synthesis of $CH_3NH_3PbBr_3$ perovskite nanoparticles, Journal of the American Chemical Society, 136 (2014) 850-853.
[25] A.M. Smith, S. Nie, Semiconductor nanocrystals: structure, properties, and band Gap engineering, Accounts of Chemical Research, 43 (2010) 190-200.
[26] S. Suresh, Semiconductor nanomaterials, methods and applications: A review, Nanoscience and Nanotechnology, 3 (2013) 62-74.
[27] C. Kittel, Introduction to solid state physics, 8 ed., John Wiley and Sons Ltd, 2004.
[28] J. Frenkel, On the transformation of light into heat in solids. I, Physical Review, 37 (1931) 17-44.
[29] G.H. Wannier, The structure of electronic excitation levels in insulating crystals, Physical Review, 52 (1937) 191-197.
[30] M. Saba, F. Quochi, A. Mura, G. Bongiovanni, Excited state properties of hybrid perovskites, Accounts of Chemical Research, 49 (2016) 166-173.

[31] J. Tilchin, D.N. Dirin, G.I. Maikov, A. Sashchiuk, M.V. Kovalenko, E. Lifshitz, Hydrogen-like Wannier-Mott excitons in single crystal of methylammonium lead bromide perovskite, ACS Nano, 10 (2016) 6363-6371.
[32] C.F. Klingshirn, Semiconductor Optics, Springer, 2007.
[33] R.J. Elliott, Intensity of optical absorption by excitons, Physical Review, 108 (1957) 1384-1389.
[34] T. Kazimierczuk, D. Fröhlich, S. Scheel, H. Stolz, M. Bayer, Giant Rydberg excitons in the copper oxide Cu_2O, Nature, 514 (2014) 343-347.
[35] A. Miyata, A. Mitioglu, P. Plochocka, O. Portugall, J.T.-W. Wang, S.D. Stranks, H.J. Snaith, R.J. Nicholas, Direct measurement of the exciton binding energy and effective masses for charge carriers in organic-inorganic tri-halide perovskites, Nature Physics, 11 (2015) 582-587.
[36] V. D'Innocenzo, G. Grancini, M.J.P. Alcocer, A.R.S. Kandada, S.D. Stranks, M.M. Lee, G. Lanzani, H.J. Snaith, A. Petrozza, Excitons versus free charges in organo-lead tri-halide perovskites, Nature Communications, 5 (2014) 3586.
[37] K. Galkowski, A. Mitioglu, A. Miyata, P. Plochocka, O. Portugall, G.E. Eperon, J.T.-W. Wang, T. Stergiopoulos, S.D. Stranks, H.J. Snaith, R.J. Nicholas, Determination of the exciton binding energy and effective masses for methylammonium and formamidinium lead tri-halide perovskite semiconductors, Energy & Environmental Science, 9 (2016) 962-970.
[38] B.J. Bohn, T. Simon, M. Gramlich, A.F. Richter, L. Polavarapu, A.S. Urban, J. Feldmann, Dephasing and quantum beating of excitons in methylammonium lead iodide perovskite nanoplatelets, ACS Photonics, 5 (2018) 648-654.
[39] A.I. Ekimov, A.L. Efros, A.A. Onushchenko, Quantum size effect in semiconductor microcrystals, Solid State Communications, 56 (1985) 921-924.
[40] E.H. Sargent, G. Konstantatos (Eds.), Colloidal quantum dot optoelectronics and photovoltaics, Cambridge University Press, 2013.
[41] L. Esaki, L.L. Chang, New transport phenomenon in a semiconductor "superlattice", Physical Review Letters, 33 (1974) 495-498.
[42] L.L. Chang, L. Esaki, R. Tsu, Resonant tunneling in semiconductor double barriers, Applied Physics Letters, 24 (1974) 593-595.
[43] G. Bastard, E.E. Mendez, L.L. Chang, L. Esaki, Exciton binding energy in quantum wells, Physical Review B, 26 (1982) 1974-1979.
[44] J. Feldmann, G. Peter, E.O. Göbel, P. Dawson, K. Moore, C. Foxon, R.J. Elliott, Linewidth dependence of radiative exciton lifetimes in quantum wells, Physical Review Letters, 59 (1987) 2337-2340.
[45] S. Glutsch, Excitons in low-dimensional semiconductors: Theory, numerical methods, applications, Springer, 2011.
[46] D.S. Chemla, D.A.B. Miller, Room-temperature excitonic nonlinear-optical effects in semiconductor quantum-well structures, Journal of the Optical Society of America B (1985) 1155-1173.

[47] A. Sommerfeld, Über die Beugung und Bremsung der Elektronen, Annalen der Physik, 403 (1931) 257-330.
[48] S. Schmitt-Rink, D.S. Chemla, D.A.B. Miller, Linear and nonlinear optical properties of semiconductor quantum wells, Advances in Physics, 38 (1989) 89-188.
[49] J. Hegarty, M.D. Sturge, Studies of exciton localization in quantum-well structures by nonlinear-optical techniques, Journal of the Optical Society of America B, 2 (1985) 1143-1154.
[50] G.W. Bryant, Electronic structure of ultrasmall quantum-well boxes, Physical Review Letters, 59 (1987) 1140-1143.
[51] A. Hidefumi, One-dimensional excitons in GaAs quantum wires, Journal of Physics: Condensed Matter, 10 (1998) 3095.
[52] T. Ogawa, T. Takagahara, Optical absorption and Sommerfeld factors of one-dimensional semiconductors: An exact treatment of excitonic effects, Physical Review B, 44 (1991) 8138-8156.
[53] R. Dingle, W. Wiegmann, C.H. Henry, Quantum states of confined carriers in very thin $Al_xGa_{1-x}As$-GaAs- $Al_xGa_{1-x}As$ heterostructures, Physical Review Letters, 33 (1974) 827-830.
[54] T. Uenoyama, L.J. Sham, Hole relaxation and luminescence polarization in doped and undoped quantum wells, Physical Review Letters, 64 (1990) 3070-3073.
[55] P. Ils, C. Gréus, A. Forchel, V.D. Kulakovskii, N.A. Gippius, S.G. Tikhodeev, Linear polarization of photoluminescence emission and absorption in quantum-well wire structures: Experiment and theory, Physical Review B, 51 (1995) 4272-4277.
[56] M. Tsuchiya, J.M. Gaines, R.H. Yan, R.J. Simes, P.O. Holtz, L.A. Coldren, P.M. Petroff, Optical anisotropy in a quantum-well-wire array with two-dimensional quantum confinement, Physical Review Letters, 62 (1989) 466-469.
[57] F. Vouilloz, D.Y. Oberli, M.A. Dupertuis, A. Gustafsson, F. Reinhardt, E. Kapon, Polarization Anisotropy and valence band mixing in semiconductor quantum wires, Physical Review Letters, 78 (1997) 1580-1583.
[58] A.J. Nozik, Spectroscopy and hot electron relaxation dynamics in semiconductor quantum wells and quantum dots, Annual Review of Physical Chemistry, 52 (2001) 193-231.
[59] D. Mukherji, B.R. Nag, Band structure of semiconductor superlattices, Physical Review B, 12 (1975) 4338-4345.
[60] H.T. Grahn, Semiconductor superlattices: Growth and electronic properties, World Scientific Publishing Company, 1995.
[61] R. Tsu, A. Koma, L. Esaki, Optical properties of semiconductor superlattice, Journal of Applied Physics, 46 (1975) 842-845.
[62] B. Dieter, Quantum dots for lasers, amplifiers and computing, Journal of Physics D: Applied Physics, 38 (2005) 2055.
[63] Y. Arakawa, A. Yariv, Quantum well lasers--Gain, spectra, dynamics, IEEE Journal of Quantum Electronics, 22 (1986) 1887-1899.
[64] D. Ahn, S.L. Chuang, Y.C. Chang, Valence-band mixing effects on the gain and the refractive index change of quantum-well lasers, Journal of Applied Physics, 64 (1988) 4056-4064.

[65] M.A. Reed, J.N. Randall, R.J. Aggarwal, R.J. Matyi, T.M. Moore, A.E. Wetsel, Observation of discrete electronic states in a zero-dimensional semiconductor nanostructure, Physical Review Letters, 60 (1988) 535-537.
[66] T.A. Fulton, G.J. Dolan, Observation of single-electron charging effects in small tunnel junctions, Physical Review Letters, 59 (1987) 109-112.
[67] I. Suemune, L.A. Coldren, Band-mixing effects and excitonic optical properties in GaAs quantum wire structures-comparison with the quantum wells, IEEE Journal of Quantum Electronics, 24 (1988) 1778-1790.
[68] R. Nötzel, K.H. Ploog, Direct synthesis of semiconductor quantum-wire and quantum-dot structures, Advanced Materials, 5 (1993) 22-29.
[69] K. Kalyanasundaram, E. Borgarello, D. Duonghong, M. Grätzel, Cleavage of water by visible-light irradiation of colloidal CdS solutions; Inhibition of photocorrosion by RuO_2, Angewandte Chemie International Edition, 20 (1981) 987-988.
[70] D. Dung, J. Ramsden, M. Grätzel, Dynamics of interfacial electron-transfer processes in colloidal semiconductor systems, Journal of the American Chemical Society, 104 (1982) 2977-2985.
[71] R. Rossetti, S. Nakahara, L.E. Brus, Quantum size effects in the redox potentials, resonance Raman spectra, and electronic spectra of CdS crystallites in aqueous solution, The Journal of Chemical Physics, 79 (1983) 1086-1088.
[72] C.B. Murray, D.J. Norris, M.G. Bawendi, Synthesis and characterization of nearly monodisperse CdE (E = sulfur, selenium, tellurium) semiconductor nanocrystallites, Journal of the American Chemical Society, 115 (1993) 8706-8715.
[73] R. Mastria, A. Rizzo, Mastering heterostructured colloidal nanocrystal properties for light-emitting diodes and solar cells, Journal of Materials Chemistry C, 4 (2016) 6430-6446.
[74] A.P. Alivisatos, Perspectives on the physical chemistry of semiconductor nanocrystals, The Journal of Physical Chemistry, 100 (1996) 13226-13239.
[75] A.P. Alivisatos, Semiconductor clusters, nanocrystals, and quantum dots, Science, 271 (1996) 933.
[76] L.E. Brus, Electron-electron and electron-hole interactions in small semiconductor crystallites: The size dependence of the lowest excited electronic state, The Journal of Chemical Physics, 80 (1984) 4403-4409.
[77] V.L. Colvin, M.C. Schlamp, A.P. Alivisatos, Light-emitting diodes made from cadmium selenide nanocrystals and a semiconducting polymer, Nature, 370 (1994) 354-357.
[78] B.O. Dabbousi, J. Rodriguez-Viejo, F.V. Mikulec, J.R. Heine, H. Mattoussi, R. Ober, K.F. Jensen, M.G. Bawendi, (CdSe)ZnS core-shell quantum dots: Synthesis and characterization of a size series of highly luminescent nanocrystallites, The Journal of Physical Chemistry B, 101 (1997) 9463-9475.

[79] V.I. Klimov, A.A. Mikhailovsky, S. Xu, A. Malko, J.A. Hollingsworth, C.A. Leatherdale, H.J. Eisler, M.G. Bawendi, Optical gain and stimulated emission in nanocrystal quantum dots, Science, 290 (2000) 314-317.
[80] X. Peng, L. Manna, W. Yang, J. Wickham, E. Scher, A. Kadavanich, A.P. Alivisatos, Shape control of CdSe nanocrystals, Nature, 404 (2000) 59-61.
[81] C. Burda, X. Chen, R. Narayanan, M.A. El-Sayed, Chemistry and properties of nanocrystals of different shapes, Chemical Reviews, 105 (2005) 1025-1102.
[82] J. Yang, J.S. Son, J.H. Yu, J. Joo, T. Hyeon, Advances in the colloidal synthesis of two-dimensional semiconductor nanoribbons, Chemistry of Materials, 25 (2013) 1190-1198.
[83] S. Ithurria, M.D. Tessier, B. Mahler, R.P.S.M. Lobo, B. Dubertret, A.L. Efros, Colloidal nanoplatelets with two-dimensional electronic structure, Nature Materials, 10 (2011) 936.
[84] S. Ithurria, B. Dubertret, Quasi 2D colloidal CdSe platelets with thicknesses controlled at the atomic level, Journal of the American Chemical Society, 130 (2008) 16504-16505.
[85] C.E. Rowland, I. Fedin, H. Zhang, S.K. Gray, A.O. Govorov, D.V. Talapin, R.D. Schaller, Picosecond energy transfer and multiexciton transfer outpaces Auger recombination in binary CdSe nanoplatelet solids, Nature Materials, 14 (2015) 484-489.
[86] B. Guzelturk, O. Erdem, M. Olutas, Y. Kelestemur, H.V. Demir, Stacking in colloidal nanoplatelets: Tuning excitonic properties, ACS Nano, 8 (2014) 12524-12533.
[87] M. Lomascolo, A. Cretì, G. Leo, L. Vasanelli, L. Manna, Exciton relaxation processes in colloidal core/shell ZnSe/ZnS nanocrystals, Applied Physics Letters, 82 (2003) 418-420.
[88] R. Gustav, Beschreibung einiger neuen Mineralien des Urals, Annalen der Physik, 124 (1839) 551-573.
[89] C.J. Howard, H.T. Stokes, Group-theoretical analysis of octahedral tilting in perovskites, Acta Crystallographica Section B, 54 (1998) 782-789.
[90] A. Glazer, Simple ways of determining perovskite structures, Acta Crystallographica Section A, 31 (1975) 756-762.
[91] G. Kieslich, S. Sun, A.K. Cheetham, Solid-state principles applied to organic-inorganic perovskites: new tricks for an old dog, Chemical Science, 5 (2014) 4712-4715.
[92] Y. Zhao, D.J. Weidner, J.B. Parise, D.E. Cox, Critical phenomena and phase transition of perovskite-data for $NaMgF_3$ perovskite. Part II, Physics of the Earth and Planetary Interiors, 76 (1993) 17-34.
[93] T. Vogt, W.W. Schmahl, The high-temperature phase transition in perovskite, Europhysics Letters, 24 (1993) 281.
[94] S. Hirotsu, Experimental studies of structural phase transitions in $CsPbCl_3$, Journal of the Physical Society of Japan, 31 (1971) 552-560.
[95] J.S. Manser, J.A. Christians, P.V. Kamat, Intriguing optoelectronic properties of metal halide perovskites, Chemical Reviews, 116 (2016) 12956-13008.

[96] K. Matsuishi, T. Ishihara, S. Onari, Y.H. Chang, C.H. Park, Optical properties and structural phase transitions of lead-halide based inorganic–organic 3D and 2D perovskite semiconductors under high pressure, physica status solidi (b), 241 (2004) 3328-3333.
[97] C. Li, X. Lu, W. Ding, L. Feng, Y. Gao, Z. Guo, Formability of ABX_3 (X = F, Cl, Br, I) halide perovskites, Acta Crystallographica Section B, 64 (2008) 702-707.
[98] V.M. Goldschmidt, Die Gesetze Der Krystallochemie, Naturwissenschaften, 14 (1926) 477-485.
[99] I.B. Koutselas, L. Ducasse, G.C. Papavassiliou, Electronic properties of three- and low-dimensional semiconducting materials with Pb halide and Sn halide units, Journal of Physics: Condensed Matter, 8 (1996) 1217.
[100] D.B. Mitzi, C.D. Dimitrakopoulos, L.L. Kosbar, Structurally tailored organic-inorganic perovskites: Optical properties and solution-processed channel materials for thin-film transistors, Chemistry of Materials, 13 (2001) 3728-3740.
[101] D.B. Mitzi, K. Chondroudis, C.R. Kagan, Organic-inorganic electronics, IBM J. Res. Dev., 45 (2001) 29-45.
[102] T. Umebayashi, K. Asai, T. Kondo, A. Nakao, Electronic structures of lead iodide based low-dimensional crystals, Physical Review B, 67 (2003) 155405.
[103] I. Borriello, G. Cantele, D. Ninno, Ab initio investigation of hybrid organic-inorganic perovskites based on tin halides, Physical Review B, 77 (2008) 235214.
[104] B.R. Vincent, K.N. Robertson, T.S. Cameron, O. Knop, Alkylammonium lead halides. Part 1. Isolated PbI_6^{4-} ions in $(CH_3NH_3)_4PbI_6 \cdot 2H_2O$, Canadian Journal of Chemistry, 65 (1987) 1042-1046.
[105] L.-y. Huang, W.R.L. Lambrecht, Electronic band structure, phonons, and exciton binding energies of halide perovskites $CsSnCl_3$, $CsSnBr_3$, and $CsSnI_3$, Physical Review B, 88 (2013) 165203.
[106] G.C. Papavassiliou, I.B. Koutselas, Structural, optical and related properties of some natural three- and lower-dimensional semiconductor systems, Synthetic Metals, 71 (1995) 1713-1714.
[107] D. Fröhlich, K. Heidrich, H. Künzel, G. Trendel, J. Treusch, Cesium-trihalogen-plumbates a new class of ionic semiconductors, Journal of Luminescence, 18-19 (1979) 385-388.
[108] J. Even, L. Pedesseau, M.A. Dupertuis, J.M. Jancu, C. Katan, Electronic model for self-assembled hybrid organic/perovskite semiconductors: Reverse band edge electronic states ordering and spin-orbit coupling, Physical Review B, 86 (2012) 205301.
[109] A.X. Gray, C. Papp, S. Ueda, B. Balke, Y. Yamashita, L. Plucinski, J. Minár, J. Braun, E.R. Ylvisaker, C.M. Schneider, W.E. Pickett, H. Ebert, K. Kobayashi, C.S. Fadley, Probing bulk electronic structure with hard X-ray angle-resolved photoemission, Nature Materials, 10 (2011) 759-764.
[110] Y. Yan, Q. Wang, W. Shu, Z. Jia, X. Ren, X. Zhang, Y. Huang, First-principle study of the electronic and optical properties of BInGaAs quaternary alloy lattice-matched to GaAs, Physica B: Condensed Matter, 407 (2012) 4570-4573.

[111] K. Matsuishi, T. Ishihara, S. Onari, Y.H. Chang, C.H. Park, Optical properties and structural phase transitions of lead-halide based inorganic–organic 3D and 2D perovskite semiconductors under high pressure, Physica Status Solidi (b), 241 (2004) 3328-3333.
[112] S. Maintz, L.D. Volker, A.L. Tchougréeff, R. Dronskowski, Analytic projection from plane-wave and PAW wavefunctions and application to chemical-bonding analysis in solids, Journal of Computational Chemistry, 34 (2013) 2557-2567.
[113] P. Umari, E. Mosconi, F. De Angelis, Relativistic GW calculations on $CH_3NH_3PbI_3$ and $CH_3NH_3SnI_3$ perovskites for solar cell applications, Scientific Reports, 4 (2014) 4467.
[114] N.-G. Park, Perovskite solar cells: an emerging photovoltaic technology, Materials Today, 18 (2015) 65-72.
[115] H. Zhou, Q. Chen, G. Li, S. Luo, T.-b. Song, H.-S. Duan, Z. Hong, J. You, Y. Liu, Y. Yang, Interface engineering of highly efficient perovskite solar cells, Science, 345 (2014) 542.
[116] W. Nie, H. Tsai, R. Asadpour, J.-C. Blancon, A.J. Neukirch, G. Gupta, J.J. Crochet, M. Chhowalla, S. Tretiak, M.A. Alam, H.-L. Wang, A.D. Mohite, High-efficiency solution-processed perovskite solar cells with millimeter-scale grains, Science, 347 (2015) 522.
[117] W. Zhang, S. Pathak, N. Sakai, T. Stergiopoulos, P.K. Nayak, N.K. Noel, A.A. Haghighirad, V.M. Burlakov, D.W. deQuilettes, A. Sadhanala, W. Li, L. Wang, D.S. Ginger, R.H. Friend, H.J. Snaith, Enhanced optoelectronic quality of perovskite thin films with hypophosphorous acid for planar heterojunction solar cells, Nature Communications, 6 (2015) 10030.
[118] S. De Wolf, J. Holovsky, S.-J. Moon, P. Löper, B. Niesen, M. Ledinsky, F.-J. Haug, J.-H. Yum, C. Ballif, Organometallic halide perovskites: Sharp optical absorption edge and its relation to photovoltaic performance, The Journal of Physical Chemistry Letters, 5 (2014) 1035-1039.
[119] D. Shi, V. Adinolfi, R. Comin, M. Yuan, E. Alarousu, A. Buin, Y. Chen, S. Hoogland, A. Rothenberger, K. Katsiev, Y. Losovyj, X. Zhang, P.A. Dowben, O.F. Mohammed, E.H. Sargent, O.M. Bakr, Low trap-state density and long carrier diffusion in organolead trihalide perovskite single crystals, Science, 347 (2015) 519-522.
[120] X. Wu, M.T. Trinh, D. Niesner, H. Zhu, Z. Norman, J.S. Owen, O. Yaffe, B.J. Kudisch, X.Y. Zhu, Trap states in lead iodide perovskites, Journal of the American Chemical Society, 137 (2015) 2089-2096.
[121] P.E. Shaw, A. Ruseckas, I.D.W. Samuel, Exciton diffusion measurements in poly(3-hexylthiophene), Advanced Materials, 20 (2008) 3516-3520.
[122] H. Zhu, Y. Fu, F. Meng, X. Wu, Z. Gong, Q. Ding, M.V. Gustafsson, M.T. Trinh, S. Jin, X.Y. Zhu, Lead halide perovskite nanowire lasers with low lasing thresholds and high quality factors, Nature Materials, 14 (2015) 636-642.
[123] F. Deschler, M. Price, S. Pathak, L.E. Klintberg, D.-D. Jarausch, R. Higler, S. Hüttner, T. Leijtens, S.D. Stranks, H.J. Snaith, M. Atatüre, R.T. Phillips, R.H. Friend, High photoluminescence efficiency and optically pumped lasing in solution-processed mixed halide perovskite semiconductors, The Journal of Physical Chemistry Letters, 5 (2014) 1421-1426.

[124] J.A. Sichert, Y. Tong, N. Mutz, M. Vollmer, S. Fischer, K.Z. Milowska, R. García Cortadella, B. Nickel, C. Cardenas-Daw, J.K. Stolarczyk, A.S. Urban, J. Feldmann, Quantum size effect in organometal halide perovskite nanoplatelets, Nano Letters, 15 (2015) 6521-6527.
[125] G.T. Einevoll, Confinement of excitons in quantum dots, Physical Review B, 45 (1992) 3410-3417.
[126] A.L. Efros, Excitons in quantum-well structures, Soviet Physics Semiconductors, 1986.
[127] E. Jacky, P. Laurent, K. Claudine, Understanding quantum confinement of charge carriers in layered 2D hybrid perovskites, ChemPhysChem, 15 (2014) 3733-3741.
[128] Q. Chen, N. De Marco, Y. Yang, T.-B. Song, C.-C. Chen, H. Zhao, Z. Hong, H. Zhou, Y. Yang, Under the spotlight: The organic–inorganic hybrid halide perovskite for optoelectronic applications, Nano Today, 10 (2015) 355-396.
[129] J. Liang, C. Wang, Y. Wang, Z. Xu, Z. Lu, Y. Ma, H. Zhu, Y. Hu, C. Xiao, X. Yi, G. Zhu, H. Lv, L. Ma, T. Chen, Z. Tie, Z. Jin, J. Liu, All-inorganic perovskite solar cells, Journal of the American Chemical Society, 138 (2016) 15829-15832.
[130] Y. Tong, E. Bladt, M.F. Aygüler, A. Manzi, K.Z. Milowska, V.A. Hintermayr, P. Docampo, S. Bals, A.S. Urban, L. Polavarapu, J. Feldmann, Highly luminescent cesium lead halide perovskite nanocrystals with tunable composition and thickness by ultrasonication, Angewandte Chemie International Edition, 55 (2016) 13887-13892.
[131] L. Protesescu, S. Yakunin, M.I. Bodnarchuk, F. Krieg, R. Caputo, C.H. Hendon, R.X. Yang, A. Walsh, M.V. Kovalenko, Nanocrystals of cesium lead halide perovskites ($CsPbX_3$, X = Cl, Br, and I): Novel optoelectronic materials showing bright emission with wide color gamut, Nano Letters, 15 (2015) 3692-3696.
[132] T.J. Savenije, C.S. Ponseca, L. Kunneman, M. Abdellah, K. Zheng, Y. Tian, Q. Zhu, S.E. Canton, I.G. Scheblykin, T. Pullerits, A. Yartsev, V. Sundström, Thermally activated exciton dissociation and recombination control the carrier dynamics in organometal halide perovskite, The Journal of Physical Chemistry Letters, 5 (2014) 2189-2194.
[133] M.A. Boles, D. Ling, T. Hyeon, D.V. Talapin, The surface science of nanocrystals, Nature Materials, 15 (2016) 141-153.
[134] K. Tanaka, T. Kondo, Bandgap and exciton binding energies in lead-iodide-based natural quantum-well crystals, Science and Technology of Advanced Materials, 4 (2003) 599-604.
[135] T. Ishihara, J. Takahashi, T. Goto, Optical properties due to electronic transitions in two-dimensional semiconductors $(C_nH_{2n+1}NH_3)_2PbI_4$, Physical Review B, 42 (1990) 11099-11107.
[136] R.R. Guseinov, Coulomb interaction and excitons in a superlattice, Physica Status Solidi (b), 125 (1984) 237-243.
[137] C. Wehrenfennig, G.E. Eperon, M.B. Johnston, H.J. Snaith, L.M. Herz, High charge carrier mobilities and lifetimes in organolead trihalide perovskites, Advanced Materials, 26 (2014) 1584-1589.

[138] S.D. Stranks, V.M. Burlakov, T. Leijtens, J.M. Ball, A. Goriely, H.J. Snaith, Recombination kinetics in organic-inorganic perovskites: Excitons, free charge, and subgap states, Physical Review Applied, 2 (2014) 034007.
[139] H. Huang, L. Polavarapu, J.A. Sichert, A.S. Susha, A.S. Urban, A.L. Rogach, Colloidal lead halide perovskite nanocrystals: synthesis, optical properties and applications, NPG Asia Materials, 8 (2016) e328.
[140] A. Naeem, F. Masia, S. Christodoulou, I. Moreels, P. Borri, W. Langbein, Giant exciton oscillator strength and radiatively limited dephasing in two-dimensional platelets, Physical Review B, 91 (2015) 121302.
[141] G. Nedelcu, L. Protesescu, S. Yakunin, M.I. Bodnarchuk, M.J. Grotevent, M.V. Kovalenko, Fast anion-exchange in highly luminescent nanocrystals of cesium lead halide perovskites ($CsPbX_3$, X = Cl, Br, I), Nano Letters, 15 (2015) 5635-5640.
[142] Q.A. Akkerman, V. D'Innocenzo, S. Accornero, A. Scarpellini, A. Petrozza, M. Prato, L. Manna, Tuning the optical properties of cesium lead halide perovskite nanocrystals by anion exchange reactions, Journal of the American Chemical Society, 137 (2015) 10276-10281.
[143] W. Tress, N. Marinova, T. Moehl, S.M. Zakeeruddin, M.K. Nazeeruddin, M. Grätzel, Understanding the rate-dependent J-V hysteresis, slow time component, and aging in $CH_3NH_3PbI_3$ perovskite solar cells: the role of a compensated electric field, Energy & Environmental Science, 8 (2015) 995-1004.
[144] Y. Tong, B.J. Bohn, E. Bladt, K. Wang, P. Müller-Buschbaum, S. Bals, A.S. Urban, L. Polavarapu, J. Feldmann, From precursor powders to $CsPbX_3$ perovskite nanowires: One-pot synthesis, growth mechanism, and oriented self-assembly, Angewandte Chemie International Edition, 56 (2017) 13887-13892.
[145] A. Swarnkar, R. Chulliyil, V.K. Ravi, M. Irfanullah, A. Chowdhury, A. Nag, Colloidal $CsPbBr_3$ perovskite nanocrystals: Luminescence beyond traditional quantum dots, Angewandte Chemie, 127 (2015) 15644-15648.
[146] M. Giersig, I. Pastoriza-Santos, L.M. Liz-Marzan, Evidence of an aggregative mechanism during the formation of silver nanowires in N,N-dimethylformamide, Journal of Materials Chemistry, 14 (2004) 607-610.
[147] Y.-N. Wang, W.-T. Wei, C.-W. Yang, M.H. Huang, Seed-mediated growth of ultralong gold nanorods and nanowires with a wide range of length tunability, Langmuir, 29 (2013) 10491-10497.
[148] K.-S. Cho, D.V. Talapin, W. Gaschler, C.B. Murray, Designing PbSe nanowires and nanorings through oriented attachment of nanoparticles, Journal of the American Chemical Society, 127 (2005) 7140-7147.
[149] J. Zhang, A.A. Lutich, J. Rodríguez-Fernández, A.S. Susha, A.L. Rogach, F. Jäckel, J. Feldmann, Optical anisotropy of semiconductor nanowires beyond the electrostatic limit, Physical Review B, 82 (2010) 155301.

[150] J.G. Rivas, O.L. Muskens, M.T. Borgström, S.L. Diedenhofen, E.P.A.M. Bakkers, Optical anisotropy of semiconductor nanowires, in: Z.M. Wang (Ed.) One-Dimensional Nanostructures, Springer New York, New York, NY, 2008, pp. 127-145.
[151] J. Wang, M.S. Gudiksen, X. Duan, Y. Cui, C.M. Lieber, Highly polarized photoluminescence and photodetection from single indium phosphide nanowires, Science, 293 (2001) 1455-1457.
[152] N.P. Dasgupta, J. Sun, C. Liu, S. Brittman, S.C. Andrews, J. Lim, H. Gao, R. Yan, P. Yang, 25th Anniversary Article: Semiconductor nanowires-synthesis, characterization, and applications, Advanced Materials, 26 (2014) 2137-2184.
[153] Y. Xia, P. Yang, Y. Sun, Y. Wu, B. Mayers, B. Gates, Y. Yin, F. Kim, H. Yan, One-dimensional nanostructures: Synthesis, characterization, and applications, Advanced Materials, 15 (2003) 353-389.
[154] P.C. Sercel, K.J. Vahala, Analytical technique for determining the polarization dependence of optical matrix elements in quantum wires with band-coupling effects, Applied Physics Letters, 57 (1990) 545-547.
[155] A.V. Maslov, C.Z. Ning, Radius-dependent polarization anisotropy in semiconductor nanowires, Physical Review B, 72 (2005) 161310.
[156] F. Vouilloz, D.Y. Oberli, M.A. Dupertuis, A. Gustafsson, F. Reinhardt, E. Kapon, Effect of lateral confinement on valence-band mixing and polarization anisotropy in quantum wires, i Physical Review B 57 (1998), 12378.
[157] H.P. Zappe, Introduction to semiconductor integrated optics, Artech House Publishers, 1995.
[158] J.D. Cutnell, K.W. Johnson, Physics, 5 ed., John Wiley, 2001.
[159] M. Leroux, N. Grandjean, B. Beaumont, G. Nataf, F. Semond, J. Massies, P. Gibart, Temperature quenching of photoluminescence intensities in undoped and doped GaN, Journal of Applied Physics, 86 (1999) 3721-3728.
[160] Y. Fang, L. Wang, Q. Sun, T. Lu, Z. Deng, Z. Ma, Y. Jiang, H. Jia, W. Wang, J. Zhou, H. Chen, Investigation of temperature-dependent photoluminescence in multi-quantum wells, Scientific Reports, 5 (2015) 12718.
[161] Y. Tong, E.-P. Yao, A. Manzi, E. Bladt, K. Wang, M. Döblinger, S. Bals, P. Müller-Buschbaum, A.S. Urban, L. Polavarapu, J. Feldmann, Spontaneous self-assembly of perovskite nanocrystals into electronically coupled supercrystals: Toward filling the green gap, Advanced Materials, DOI:10.1002/adma.201801117.
[162] C.C. Stoumpos, C.D. Malliakas, J.A. Peters, Z. Liu, M. Sebastian, J. Im, T.C. Chasapis, A.C. Wibowo, D.Y. Chung, A.J. Freeman, B.W. Wessels, M.G. Kanatzidis, Crystal growth of the perovskite semiconductor $CsPbBr_3$: A new material for high-energy radiation detection, Crystal Growth & Design, 13 (2013) 2722-2727.
[163] C.R. Kagan, C.B. Murray, Charge transport in strongly coupled quantum dot solids, Nature Nanotechnology, 10 (2015) 1013-1026.

[164] Z. Nie, A. Petukhova, E. Kumacheva, Properties and emerging applications of self-assembled structures made from inorganic nanoparticles, Nature Nanotechnology, 5 (2009) 15-25.
[165] M.P. Pileni, Nanocrystal self-assemblies: Fabrication and collective properties, The Journal of Physical Chemistry B, 105 (2001) 3358-3371.
[166] Y. Min, M. Akbulut, K. Kristiansen, Y. Golan, J. Israelachvili, The role of interparticle and external forces in nanoparticle assembly, Nature Materials, 7 (2008) 527-538.
[167] M. Grzelczak, J. Vermant, E.M. Furst, L.M. Liz-Marzán, Directed self-assembly of nanoparticles, ACS Nano, 4 (2010) 3591-3605.
[168] S. Sun, C.B. Murray, D. Weller, L. Folks, A. Moser, Monodisperse FePt nanoparticles and ferromagnetic FePt nanocrystal superlattices, Science, 287 (2000) 1989-1992.
[169] A. Dong, J. Chen, P.M. Vora, J.M. Kikkawa, C.B. Murray, Binary nanocrystal superlattice membranes self-assembled at the liquid-air interface, Nature, 466 (2010) 474-477.
[170] H. Tong, N. Umezawa, J. Ye, T. Ohno, Electronic coupling assembly of semiconductor nanocrystals: self-narrowed band gap to promise solar energy utilization, Energy & Environmental Science, 4 (2011) 1684-1689.
[171] A. Dong, Y. Jiao, D.J. Milliron, Electronically coupled nanocrystal superlattice films by in situ ligand exchange at the liquid-air interface, ACS Nano, 7 (2013) 10978-10984.
[172] K. Fujiwara, R. Cingolani, K. Ploog, Spectroscopic investigations of miniband dispersion and excitonic effects in GaAs/AlAs short-period superlattices, Solid State Communications, 72 (1989) 389-392.
[173] P.-f. Yuh, K.L. Wang, Formalism of the Kronig-Penney model for superlattices of variable basis, Physical Review B, 38 (1988) 13307-13315.
[174] T. Forster, 10th Spiers Memorial Lecture. Transfer mechanisms of electronic excitation, Discussions of the Faraday Society, 27 (1959) 7-17.
[175] M.J. Pilling, S.A. Rice, Long range energy transfer by dipole-dipole and exchange interactions in rigid media and in liquids, Journal of the Chemical Society, Faraday Transactions 2: Molecular and Chemical Physics, 72 (1976) 792-801.
[176] C.R. Kagan, C.B. Murray, M. Nirmal, M.G. Bawendi, Electronic energy transfer in CdSe quantum dot solids, Physical Review Letters, 76 (1996) 1517-1520.
[177] T. Franzl, D.S. Koktysh, T.A. Klar, A.L. Rogach, J. Feldmann, N. Gaponik, Fast energy transfer in layer-by-layer assembled CdTe nanocrystal bilayers, Applied Physics Letters, 84 (2004) 2904-2906.
[178] T. Franzl, T.A. Klar, S. Schietinger, A.L. Rogach, J. Feldmann, Exciton recycling in graded gap nanocrystal structures, Nano Letters, 4 (2004) 1599-1603.
[179] S. Mayilo, J. Hilhorst, A.S. Susha, C. Höhl, T. Franzl, T.A. Klar, A.L. Rogach, J. Feldmann, Energy transfer in solution-based clusters of CdTe nanocrystals electrostatically bound by calcium ions, The Journal of Physical Chemistry C, 112 (2008) 14589-14594.
[180] K. Becker, J.M. Lupton, J. Müller, A.L. Rogach, D.V. Talapin, H. Weller, J. Feldmann, Electrical control of Förster energy transfer, Nature Materials, 5 (2006) 777-781.

[181] M.V. Artemyev, A.I. Bibik, L.I. Gurinovich, S.V. Gaponenko, U. Woggon, Evolution from individual to collective electron states in a dense quantum dot ensemble, Physical Review B, 60 (1999) 1504-1506.
[182] M.V. Artemyev, U. Woggon, H. Jaschinski, L.I. Gurinovich, S.V. Gaponenko, Spectroscopic study of electronic states in an ensemble of close-packed CdSe nanocrystals, The Journal of Physical Chemistry B, 104 (2000) 11617-11621.
[183] S. Mourdikoudis, L.M. Liz-Marzán, Oleylamine in nanoparticle synthesis, Chemistry of Materials, 25 (2013) 1465-1476.
[184] Z. Wang, X.-D. Wen, R. Hoffmann, J.S. Son, R. Li, C.-C. Fang, D.-M. Smilgies, T. Hyeon, Reconstructing a solid-solid phase transformation pathway in CdSe nanosheets with associated soft ligands, Proceedings of the National Academy of Sciences, 107 (2010) 17119-17124.
[185] A. Manzi, Y. Tong, J. Feucht, E.-P. Yao, L. Polavarapu, A.S. Urban, J. Feldmann, Resonantly enhanced multiple exciton generation through below-band-gap multi-photon absorption in perovskite nanocrystals, Nature Communications, 9 (2018) 1518.

Acknowledgements

It is a great experience for me to do my Ph.D. dissertation in this international group, I had a good time and also learned a lot. I would like to thank many people for their kind help and support.

First, I would like to thank **Professor Jochen Feldmann** for giving me the opportunity to do my research in his chair and supervising my doctoral thesis. His solid and broad knowledge in physics greatly helped me to understand the physical principles of the semiconductor system which I worked on. With his supervision and many constructive ideas and comments, I learned how to think and make deeper investigation from the physics perspective. I also want to mention that the high research standard, the excellent academic atmosphere and experimental equipment of the chair are extremely helpful for enhancing my knowledge background as well as realizing new ideas. I am very grateful that he gave me the chances to present my results at international conferences and join collaborative research projects, which has improved my experimental and conversational skills.

Many thanks to **Dr. Alexander Urban**, he is always available for productive discussions, he gave me many suggestions to make progress in my research projects. He is always happy to share his broad physics knowledge and scientific experiences with us and I benefit much from this. I am also very thankful to **Dr. Lakshminarayana Polavarapu**, with his broad interests in science, he really showed me that doing scientific research can be a lot of fun. He also motivated me to realize research ideas by well-designed experiment and gave me help in the whole process. Both of them helped me a lot in preparing posters, oral presentations, papers, abstracts and also this thesis.

I am thankful to **Prof. Thomas Bein**, **Prof. Dr. Joachim Rädler**, **Prof. Dr. Sara Bals**, **Prof. Dr. Hermann Gaub**, **Prof. Dr. Peter Müller-Buschbaum** for providing the TEM, HRTEM, AFM and XRD characterization instruments. I want to thank **Dr. Markus Döblinger**, **Dr. Andreas Wisnet**, **Eva Bladt**, **Dr. Willem Vanderlinden**, **Kun Wang**, **Meltem Aygüler** and **Dr. Pablo Docampo** for measurements and helpful discussions.

I want to thank **Prof. Dr. Hilmi Volkan Demir** and **Dr. Samuel Stranks** for their support in collaborative research and helpful discussions. And thanks to **Dr. Robert Hoye**, **MayLing Lai** and **Dr. Fei Yan** for their great efforts in the collaborative projects.

Thanks to **Dr. Ming Fu** for giving me instructions on the spectroscopic equipment and being very helpful in both experiment and theory. I would also like to thank **Dr. Jacek Stolarczyk**, **Dr. Carlos Cardenas-Daw**, **Dr. Karolina Milowska**, **Dr. En-Ping Yao**, **Dr. Verena Hintermayr**, **Alexander Richter**, **Aurora Manzi**, **Bernhard Bohn**, **Florian Ehrat**, **Jasmina Sichert** and **Sebastian Rieger** for their help in my research projects. Particular thanks to **Aurora Manzi**, **Bernhard Bohn** and **Jasmina Sichert** for their helpful suggestions on my thesis.

I want to thank **Gerlinde Adam** for taking care of administration and **Stefan Niedermaier** for the help in technical questions and making specialized devices for experiments. And thanks to **Christoph Maier** and **Patrick Urban** for the help with computer issues.

My special thanks go to all my colleagues at the Chair of Photonics and Optoelectronics, there are too many to list all of them. I appreciate the wonderful time working with you.

I am also very grateful for the support and help from the **China Scholarship Council** and the **LMU international office**.

Last but not least, I would like to thank my family and friends, especially my parents and my girlfriend for their endless support, which gives me enormous encouragement in my life.